Farbod Fonoon

Contact information

Address: Room 1326, Gymnasiumstraße 85 , Döbling

1190 Wien

Phone: +4368181407124

E-mail: Farbod_f16@yahoo.com , Farbodfonoon@gmail.com

Education:

- High school diploma: June, 2005. Beheshti high school.
- Pre-university: June, 2006. Motahari school.
- B.Sc. degree in solid state physics: June, 2012 - International Imam Khomeini University of Qazvin (IKIU).
- Master Program: Institute for Advanced Studies in Basic Sciences (IASBS) for two trimesters. (2012/13)
- Master program: October, 2013 - University of Vienna, Austria (Master of Physics).
- Master student intern: June, 2015 - Institute for quantum optics and quantum information (IQOQI), Vienna, Austria.

Language skills:

- Persian (Native).
- English: Ielts, Overall 6.5 (April 2012).
- German: B2 (2014). [Language center of University of Vienna]
- Arabic: Basic knowledge.

- *Workshops*:

- Intermediate and advanced Astronomy at RIAAM research institute.
- Introduction to Nanophysics applications, IKIU University.
- Galilean nights, IKIU University. (organizer)
- Quantum Information workshop: May, 2015 – Traunkirchen, Austria.

Computer skills including:

- ❖ MATLAB
- ❖ Microsoft Office
- ❖ LaTeX
- ❖ Mathematica
- ❖ LabView

Reseach interests:

- Quantum optics and information
- Free space quantum communication
- Laser physics
- Space quantum experiments

Experiences:

- ➢ Fiber-based and free space quantum optics.
- ➢ Microscope related experience: Transmission electron microscope (TEM), scanning electron microscope (SEM), scanning tunneling microscope, scanning transmission electron microscope, light microscope.
- ➢ Amateur Astronomy.

Grants:

- ✓ Research grant, Austrian Academy of Science (ÖAW).

Interests and hobbies:

- Photography
- Football
- Music
- Hiking

15.06.2016

universität wien

MASTERARBEIT / MASTER'S THESIS

Titel der Masterarbeit / Title of the Master's Thesis

" Uplink quantum communication with the international space station "

verfasst von / submitted by

Farbod Fonoon

angestrebter akademischer Grad / in partial fulfilment of the requirements for the degree of

Master of Science (MSc)

Wien, 2016 / Vienna, 2016

Studienkennzahl lt. Studienblatt / degree programme code as it appears on the student record sheet:	A 066 876
Studienrichtung lt. Studienblatt / degree programme as it appears on the student record sheet:	Masterstudium Physik (UG2002)
Betreut von / Supervisor:	o.Univ.-Prof. Dr. Anton Zeilinger

Acknowledgements

Above all, I would like to thank my parents for all the love the dedications through the years. My sincere thanks to my my family for their continuous support and Compassion.
A special thank to professor Anton Zeilinger, who has done an extraordinary contribution in developments of quantum physics both in theoretically and experimentally which led to many research establishments in Austria.
Many thanks to Dr. Rupert Ursin for supervising the works I've done over the passed year.
Lots of thanks go to my friends and colleagues in the university of Vienna and IQOQI, specially "free spacers", from whom I learned a lot. Studying in the University of Vienna and working in IQOQI was a great privilege.
Finally, I thank Austrian Academy of Science (ÖAW) for the research grant.

UNIVERSITY OF VIENNA

Abstract

UNIWIEN
University of Vienna, Physics department

Master of Science

Uplink Quantum Communication with the International Space Station

Since 20th century, the new discoveries in physics is changing the world as we knew it. One of them is quantum physics. There are strange but simultaneously amazing consequences of physics in quantum realm such as superposition, entanglement, quantum tunneling, etc. There have been various experiments testing quantum phenomena. In the past decade, lots of proposals were given including space quantum experiments. This thesis focuses on ground-space uplink experiments and more specifically with the International Space Station (ISS). We can perform various experiments like Bell-type experiment, quantum key distribution (QKD), gravitational decoherence, etc. We can make use of a motorized tracking mount (NightPod) and a photographic lens (Nikon 400mm f/2.8 AF-I) plus a digital camera (Nikon D3s) which are already on board the ISS. Additional parts are to be sent to the ISS. Before doing the actual experiment, we have to perform a preparatory experiment to acquire more data. For this purpose, we can use the equipment already on board the ISS. By characterizing the Nikon DSLR camera and the Nikon lens, they could be used for preparatory experiments and tracking purposes.

Abstract

(german)

Im 20.Jahrhundert veränderterten die neuen Entdeckungen der Physik die Welt so wie wir sie kannten. Einer von ihnen ist die Quantenphysik. Dadurch ergeben sich im Quantenreich seltsame, aber gleichzeitig erstaunliche Folgen in der Physik wie Superposition, Verschränkung, Quantentunneln usw. Viele verschiedene Experimente untersuchen diese Quantenphänomene. Im Laufe des vergangen Dezennium gabe es viele verschiedene Vorschläge einschließlich Experimente im Weltall. Diese Arbeit konzentriert sich auf Boden-Weltall Uplink Experimente und insbesondere mit der Internationalen Raumstation (ISS). Wir können verschiedene Arten von Experimente wie Bell-Experimente, Quantenschlüsselverteilung (QKD), Gravitations Dekohärenz usw. durchführen. Vor den eigentlichen Experimenten, müssen vorbereitende Experimente durchführt werden, um weitere Daten sammeln zu können. Zu diesem Zweck können wir von der bereits am Bord der ISS befindlichen Ausstattung gebrauch machen wie ein motorisierten Halterung (NightPod), einem Fotoobjektiv (Nikon 400mm f / 2.8 AF -I) sowie eine Digitalkamera (Nikon D3s). Zusatzteile können in weiterer Folge zur ISS geschickt werden. Durch die Charakterisierung der Nikon DSLR-Kamera und das Nikon-Objektiv, könnten diese für vorbereitende Experimente und Tracking-Zwecke verwendet werden.

To my parents.

Contents

Chapter 1

Quantum Physics and Space

1.1 Benefits of quantum experiments in space

FIGURE 1.1: International Space Station over the earth, seen from Space Shuttle Endeavour.

Since men walked into space a whole new opportunity opened to feed the curiosity of mankind for explorations not only about space and beyond, but also the very fundamental aspects of life and science on earth. Before the space era, we were bound to do experiments on earth and were limited to the boundaries imposed by the laws of physics such as gravity, atmosphere pressure, etc. On the other hand, performing experiments in space is favorable and sometimes even cheaper and the boundaries like gravity are no more a problem. Benefits of having a full-time low-gravity laboratory or non vanishing gratis vacuum are tremendous. To be able to exert such experiments, a station large enough to be stable and contain necessary equipment is needed. The International Space Station (ISS), the largest artificial satellite currently orbiting the Earth, is the best candidate we have. There have been lots of experiments going on, on board the ISS[1]. Due to transmission losses in fiber based quantum channels and detector dark counts, terrestrial quantum communication experiments have an upper limit for the distance of the

[1] http://www.nasa.gov/mission_pages/station/research/experiments/experiments_by_name.html

communication in the order of 100 km[24]. To overcome this problem, we can establish our quantum communication network in space.
ISS orbits the earth 15.5 time a day (93 minutes per orbit) and between each orbit earth rotates 22.5 degrees around its own axis so the next orbit would be shifted 22.5° to the west. The following figures show two different positions of ISS, 30 minutes apart.

(A) ISS position 25 April 2016 at 15:00

(B) ISS position 25 April 2016 at 15:30

FIGURE 1.2: ISS in orbit depicted with previous and next orbit and the visible region from earth. [*Mathematica*]

We can excavate the most fundamental aspects of quantum physics such as entanglement and the effect of distance, gravity[2], etc. by carrying out such ground-space linked experiments. It's been years since quantum physics evolved from pure theoretical science to applied science. The urge of having quantum computer, quantum computation, quantum communication and their subsidiaries including quantum key distribution(QKD), quantum teleportation, quantum dense coding makes such experiments useful for both theoretical and applied science.

[2]Experiments like gravitational decoherence experiment to be carried out.

1.2 Introduction to the quantum information science

Since 1820's Charles Babbage steam-driven calculating machine till now, many engineers, scientists, manufacturers tried to build smaller and more powerful computers. Nowadays people have compact computer that can carry around, thanks to advanced technologies. Moore's law state that roughly every two years, number of transistors in an integrated circuit doubles. It means the the size of transistors (distance between source and drain) are getting smaller and smaller which as of 2016 it reached the astonishing size of 10 nm. By 2025 we are expected to be close to 5 nm transistors which is the size of approximately 45 silicon atoms packed together and in these scales we cannot merely rely on classical laws of physics but also quantum physics. It mean that we still get a current when the circuit is switched off (no gate voltage) due to quantum tunneling. We could find a solution to rise the barrier between drain and source so the probability of having quantum tunneling approaches zero. The other solution is to go to another paradigm for computing, the quantum computing. Using quantum computers requires quantum algorithms instead of classical algorithms. But algorithm design for quantum computers is not easy as designers face two difficult problems which does not exist in the construction of algorithms for classical computers. First, our human intuition is based on the classical world. Using that intuition to construct quantum algorithms would subconsciously lead us to classical ideas. We should stop thinking classically for at least part of the design process, using truly quantum effects to achieve the desired algorithmic end. Second, it is not enough to design an algorithm using merely quantum physics. The algorithm must be better than any existing classical algorithm, otherwise it would be reinventing the wheel! This is truly a challenge to design a quantum algorithm which is outstandingly better than existing or even more daring, the prospective classical algorithms.[16]
First basic principle of quantum mechanics states that Every physical system is associated with a Hilbert Space, every unit vector in the space corresponds to a possible pure state of the system, and every possible pure state, to some vector in the space. The state $|\Psi>$ completely describes an isolated system. Quantum information is simply the information stored in the state of the quantum system. In order to handle this information, we adopt quantum computation which can confirm whether we can have quantum computers or not and in addition, provides the algorithm that should be used with quantum computers.

1.2.1 Quantum Communication

People have been communicating with each other in various ways for a long time. Starting from most primitive ways of communication to recent modern methods. As we move forward, our lives are getting more dependent on reliable ways of communication. Classical communication cannot fully protect our privacy between the parties which are communicating, but thanks to quantum communication, it is possible to have secure communication. The fundamental aspects of quantum physics like entanglement or no-cloning theorem would help us in the journey of having a perfectly secured communication.

1.2.2 Quantum Key Distribution

Quantum key distribution, or QKD, is a well known quantum cryptography method which provides a secure random key for the parties of a communication. Having this key, they could communicate with each other using encrypted messages. After receiving the encrypted massage, they use the secret key the produced before sending the secret message. The communicating parties can detect any third party who is trying to eavesdrop.
There various protocols for QKD e.g. BB84, B92, E91, etc., which aim to produce the key. It is necessary to mention that all of these protocols have some technical loopholes and the scientists try to restrict those loopholes as good as possible.

BB84 protocol

In the year 1984, Charles Bennett and Gilles Brassard proposed the first QKD protocol that lets parties (namely Alice and Bob) share a secret key between one another. According to quantum mechanics, there's no way to measure something without perturbing it if the two states are not orthogonal. Relying on no-cloning theorem, Alice and Bob construct a protocol to communicate.
At first, Alice starts with sending 2 stings of bits, namely "a" and "b", which are n bits long each. Each element "i" in string "a" can be in one of two orthogonal states(H/V and +/- for BB84). Elements of second string "b", determine the basis string "a" should be encoded with. In this way, Alice encodes these two strings as a string of n qubits:

$$|\psi\rangle = \bigotimes_{i=1}^{n} |\psi_{a_i b_i}\rangle \tag{1.1}$$

Which for different indices we get the following four qubits:

$$\begin{aligned} |\psi_{00}\rangle &= |0\rangle = |H\rangle \\ |\psi_{10}\rangle &= |1\rangle = |V\rangle \\ |\psi_{01}\rangle &= \frac{1}{\sqrt{2}}|0\rangle + \frac{1}{\sqrt{2}}|1\rangle = |+\rangle \\ |\psi_{11}\rangle &= \frac{1}{\sqrt{2}}|0\rangle - \frac{1}{\sqrt{2}}|1\rangle = |-\rangle \end{aligned} \tag{1.2}$$

Note that, as mentioned above, it's the second bit that decides in which basis the first bit is going to be encoded. As indexed above, if the second bit is 0, the encoding of the first bit would be in H/V basis and if the second bit is 1, encoding would be in +/- basis. These qubits are to be sent to Bob via a quantum channel. The transmission of information is done by sending photons in some polarization states. The direction of the polarization encodes a classical bit. Prior to communication, they agree on which polarization directions should assigned to 1 and which ones to 0 (See figure 1.3)[3]. In order for bob to be able to get the right polarization, considering the quantum indeterminacy, he should choose the right basis. Bod has no idea what's the polarization of the photon Alice sends in the sequence. So he chooses a random basis for measurement (either +/- or H/V). If he, by chance, chooses the right basis then he measures the correct polarization. But if he chooses a wrong (different from Alice's basis) basis, then with a probability of 50% , he get the correct polarization and 50% of the time the wrong one.

[3] http://swissquantum.idquantique.com/?Key-Sifting

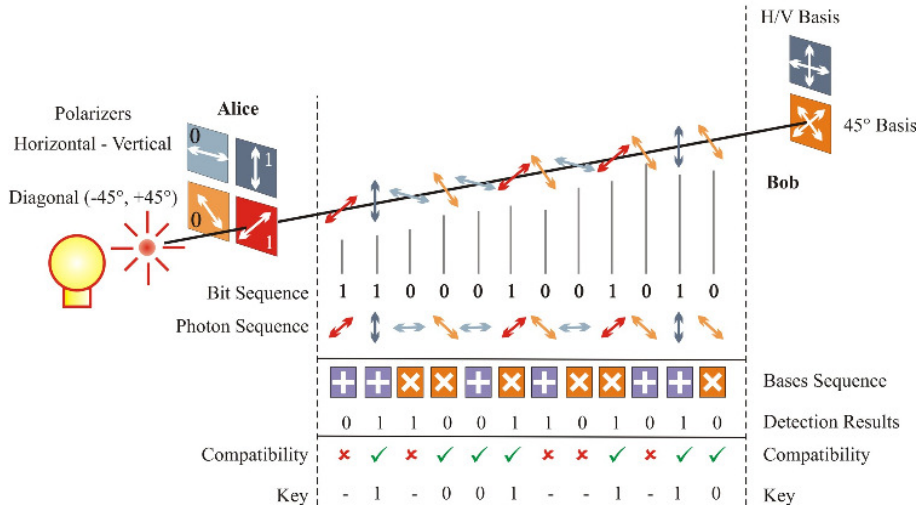

FIGURE 1.3: BB84 protocol

In Figure 1.3, Bob chooses the wrong basis for the third and sixth photon that Alice sent which have the same polarization. Once he get 0 and once 1 for the same polarization. When this phase of communication is over, Bob via a classical channel tells Alice the basis he chose for measuring each photon. Alice tells him with bases he chose wrong. After basis reconciliation, they throw away the bits that were obtained from a wrong basis choice and the rest of the bits would be the secured sifted key that would be used for further communications.
Meanwhile, like classical communication, a third party, namely Eve, can intercept the communication to eavesdrop. According to no-cloning, neither Bob or Eve can copy a qubit and have to do a measurement to get the state of the photon. Eve, same as Bob, has to choose a random basis for measuring each photon. She chooses the right polarization half of the time. After Eve prepares a similar state that she measured and sends it to Bob, Bob will measures with a wrong basis half of the time and gets the right bit. This leads to a quantum bit error rate of 25% (50% $\times$ 50%).
Alice and Bob compare a subset of the sifted key publicly and if the bits are the same 75% of the time or more, they can be sure that the communication over that quantum channel is secure, but if the bits are different more than 25% of the time, then they know that Eve is eavesdropping. Alice and Bob would abandon that quantum channel and proceed the same protocol in another quantum channel.

B92 protocol

B92 is more or less similar to BB84. In 1992, Charles Bennett published another paper proposing another protocol using any two non-orthogonal states for quantum cryptography. In this protocol only two states are needed rather than 4 polarization states in BB84.
First Alice prepares one random classical bit a, and depending on the result, sends

Bob the following qubits[16]:

$$|\psi\rangle = \begin{cases} |0\rangle\,, & \text{if } a = 0 \\ \dfrac{|0\rangle + |1\rangle}{\sqrt{2}}, & \text{if } a = 1 \end{cases} \tag{1.3}$$

Depending on the random bit(a') he generates, Bob measures the incoming qubit using Z basis $|0\rangle$, $|1\rangle$ (for $a' = 0$) basis or +/- (for $a' = 1$) basis. From his measurement, he obtains the result b, which is 0 or 1, corresponding to the -1 and +1 eigenstates of X and Z. Bob send alice the measurements results and they keep the pairs of a and a' for which the result $b = 1$ obtained.
When $a = a'$, b is equal to zero all the time. But for $a' = 1 - a$, Bob will obtain $b = 1$ for 50% of the times. The secure key would be a for Alice, and $1 - a'$ for Bob.

Ekert 91

Ekert 91 protocol is a quantum cryptography based on Bell's theorem [3]. Unlike B84 and B92, Ekert protocol makes use of entangled photons [10]. Alice won't send any photons to Bob, but they both receive pairs of entangle photons from a single source. The spin $1/2$ particles travel through the channel along the z axis toward each party of communication, Namely Alice and Bob [8]. Then they would perform a measurements on spin components of their particle along three directions given by a_i (Alice's analyzer) and b_j (Bob's analyzer) (i,j = 1,2,3). For simplicity, we can assume that both a_i and b_j lie in $x-y$ plane which is perpendicular to the trajectory of the particles and characterized by these azimuthal angle: ϕ_1^a=0° ,ϕ_2^a=45° ,ϕ_3^a=90° , ϕ_1^b=45° ,ϕ_2^b=90° , ϕ_3^b=135° . They choose a basis randomly for each measurement and each measurement can yield either $+\hbar/2$ (spin up) or $-\hbar/2$ (spin down) or simply +1 and -1 which corresponds to one bit of information. The correlation coefficient of Alice's measurement and Bob' measurement is as follows:

$$E(a_i, b_j) = P_{++}(a_i, b_j) + P_{--}(a_i, b_j) - P_{-+}(a_i, b_j) - P_{+-}(a_i, b_j) \tag{1.4}$$

Where $P_{\pm\pm}(a_i, b_j)$ is the probability that result ± 1 has been obtained along a_i and ± 1 along b_j.
As Alice and Bob are measuring entangled photons, we have:

$$E(a_i, b_j) = -a_i \cdot b_j \tag{1.5}$$

Two pairs of analyzers with the same angle have anti-correlation of the results obtained by Alice and Bob:

$$E(a_2, b_1) = E(a_3, b_2) = -1 \tag{1.6}$$

Now we define the S parameter from CHSH inequality as the sum of all correlation coefficients for which Alice and Bob used differently oriented analyzers:

$$S = E(a_1, b_1) - E(a_1, b_3) + E(a_3, b_1) + E(a_3, b_3) \tag{1.7}$$

According to local realism, we have the upper limit for S parameter (Tsirelson's bound) :

$$S \leq 2\sqrt{2} \tag{1.8}$$

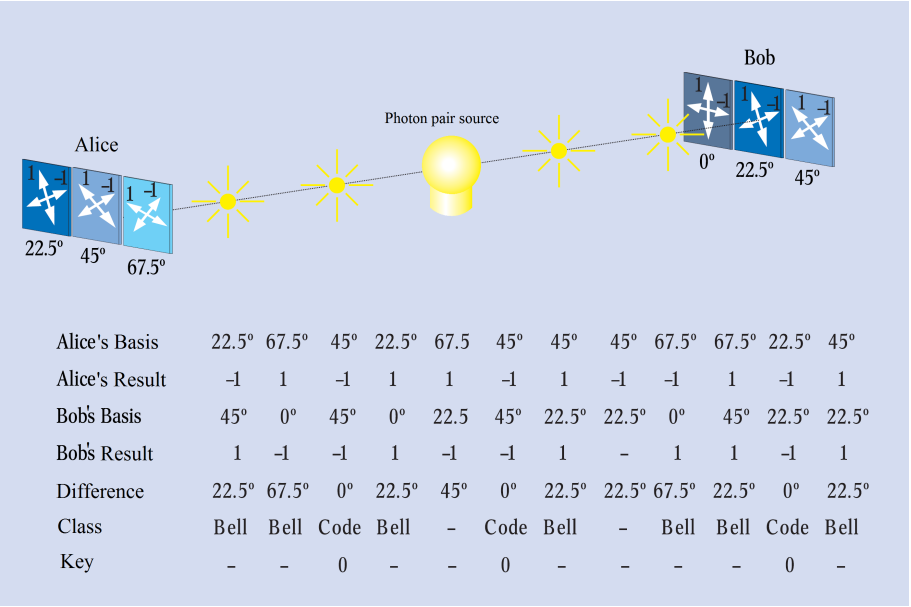

Alice's Basis	22.5°	67.5°	45°	22.5°	67.5	45°	45°	45°	67.5°	67.5°	22.5°	45°
Alice's Result	-1	1	-1	1	1	-1	1	-1	-1	1	-1	1
Bob's Basis	45°	0°	45°	0°	22.5	45°	22.5°	22.5°	0°	45°	22.5°	22.5°
Bob's Result	1	-1	-1	1	-1	-1	1	-	1	1	-1	1
Difference	22.5°	67.5°	0°	22.5°	45°	0°	22.5°	22.5°	67.5°	22.5°	0°	22.5°
Class	Bell	Bell	Code	Bell	-	Code	Bell	-	Bell	Bell	Code	Bell
Key	-	-	0	-	-	0	-	-	-	-	0	-

FIGURE 1.4: Ekert QKD protocol.[22]

They will use the bits which were measured with the same basis by Alice and Bob for the key and the other bits for Bell's measurement. Considering the initial two states were entangled, the Bell's inequality should be violated. If not, they suspect an eavesdropper and may change to another channel to communicate.

Decoy state

As seen in BB84 protocol, Alice uses a single photon source to communicate with Bob. But a real single photon source does not exist, so one should finds a source which behaves almost like a single photon source. We make use of a weak coherent state laser source.
With a weak attenuated laser, eavesdropper could still use a beam splitter and get some information about the communication. In decoy state QKD, a few different photon intensities are used instead of one (different mean photon number). The highest key rates for strong attenuation can be reached with a decoy-state protocol. We can estimate the net key generation rate with a fraction Δ of tagged photons (multiphoton pulses) in the detected photons as[12]:

$$R = \frac{1}{2}\, p_{\text{exp}} \left(\Big(1-\Delta\Big) - \Big(1-\Delta\Big) \cdot H_2\Big(\frac{\delta}{1-\Delta}\Big) - f[\delta] \cdot H_2(\delta) \right) \tag{1.9}$$

Where δ is the error in the measured key. $H_2(\delta)$ given by the binary entropy function and $[\delta]$ is the correction factor for the performance of the error correction protocol. The first term removes the information of an eavesdropper due to the multiphoton pulses. The second term comes because we assume that the error in the sifted key is caused only by non-tagged photons. The third term is the information leaked during the error correction protocol.
A lower bound of Δ could be estimated by the following formula[25]:

$$\Delta = \frac{\mu}{\mu' - \mu} \left(\frac{\mu \cdot e^{\mu}}{\mu' \cdot e^{\mu'}} \frac{Q'}{Q} - 1 \right) + \frac{\mu \cdot e^{\mu}}{\mu'} \frac{Q_0}{Q} \tag{1.10}$$

Δ is dependent only on the count rates, Q_i, of the different mean photon numbers (μ and μ').
The following graph shows the net secret key generation rate R (after error correction and privacy amplification) versus link attenuation η for a decoy state protocol using two different mean intensities plus vacuum pulses.

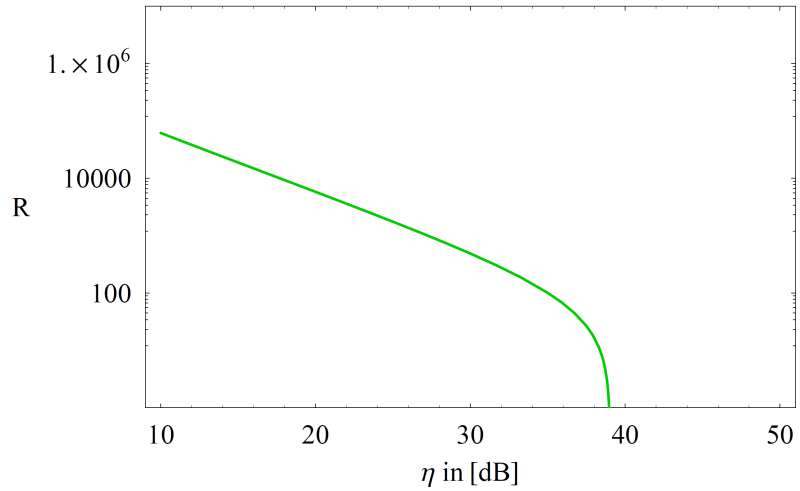

FIGURE 1.5: Net secure key generation rate R (in bits per second) for a decoy-state protocol using the weak coherent source at a repetition rate of 10 MHz versus the link attenuation η. Figure from [17]

QBER

The Quantum Bit Error Rate (QBER) is defined as the ratio of wrong bits to the total number of bits received [11] and contains information on the existence of an eavesdropper and how much he knows:

$$\text{QBER} = \frac{N_{\text{wrong}}}{N_{\text{wrong}} + N_{\text{right}}} = \frac{R_{\text{error}}}{R_{\text{error}} + R_{\text{sift}}} \underbrace{\approx \frac{R_{\text{error}}}{R_{\text{sift}}}}_{if \quad R_{\text{error}} \ll R_{\text{sift}}} \tag{1.11}$$

If the string of the raw key is long enough, then the Sifted Key rate would statistically be half that of the raw key. As the raw key is consisted of pulses of photons with frequency of f and the mean number of photons per pulse of μ, considering the probability of a photon reaching the analyzer is equal to t and the efficiency of photon detection of η, the following formula would give the sifted key rate:

$$R_{\text{sift}} = \frac{1}{2} R_{\text{raw}} = \frac{1}{2}\, f\, \mu\, t\, \eta\, q \tag{1.12}$$

The factor $q(\leqslant 1)$ is added for some phase-coding setups in order to correct for noninterfering path combinations which is usually 1 or $\frac{1}{2}$. The error could be caused from different sources. One could be that the photon going to the wrong detector due to imperfect interference or the contrast of the PBS. To calculate the portion of error caused by the photons that go into the wrong detector, is the product of the R_{sift} and P_{opt}, the probability that a photon goes into a wrong

detector.

$$R_{\text{opt}} = R_{\text{sift}} p_{\text{opt}} = \frac{1}{2}\, f\, \mu\, t\, \eta\, q\, p_{\text{opt}} \tag{1.13}$$

The second source of the error is the detector. We should take into account the dark counts (intrinsic) and the background noise (free-space setup).

$$R_{\text{det}} = \frac{1}{2}\,\frac{1}{2}\, f\, p_{\text{d}}\, n \tag{1.14}$$

The p_{d} is the probability of a dark count per time window and per detector, and n is the number of the detectors used by Alice and Bob. The fist $\frac{1}{2}$ factor is due to the fact that a dark count could happen by a chance of 50% when Alice and Bob choose incompatible bases and so would be thrown away during the reconciliation. The second $\frac{1}{2}$ factor is the 50% chance of a dark count happens in the right detector.
The third source could be the accidental count caused by uncorrelated photons being counted in *entanglement based* setups. There's a given time window that the photons are registered and sometimes photons belonging to different pairs arrive in the same time window which are not necessarily in the same state.The p_{acc} is the probability of finding a second pair within the time window, knowing that a first one was created. The rate of these accidental counts would be given by:

$$R_{\text{acc}} = \frac{1}{2}\,\frac{1}{2}\, f\, p_{\text{acc}}\, n\, t\, \eta \tag{1.15}$$

Now we can rewrite the QBER as:

$$\begin{aligned} \text{QBER} &= \frac{R_{\text{opt}} + R_{\text{det}} + R_{\text{acc}}}{R_{\text{sift}}} \\ &= p_{\text{opt}} + \frac{p_d\, n}{t\, \eta\, 2\, q\, \mu} + \frac{p_{\text{acc}}}{2\, q\, \mu} \\ &= \text{QBER}_{\text{opt}} + \text{QBER}_{\text{det}} + \text{QBER}_{\text{acc}} \end{aligned} \tag{1.16}$$

For the phase coding setups:

$$\text{QBER}_{\text{opt}} = p_{\text{opt}} \simeq \frac{1 - V}{2} \tag{1.17}$$

Where V is the interference visibility.

1.2.3 Quantum teleportation

Beside the exciting aspects of quantum teleportation in science fiction, it is actually a technique to make use of entanglement to send a quantum state from sender to recipient without having a quantum communicational channel linking those two. We should keep in mind that quantum teleportation is different from the common teleportation often mentioned in Sci-Fi literature. Quantum teleportation is not about transfering a particle but about communicating. Moreover, as the information is sent on a classical channel, this communication cannot violate the fact that the uplimit speed of communication is bound to speed of light.
So how can one transport a qubit from a place to another without transfering a physical particle?

The answer lies in the notion of entanglement. The procedure is as follows:
Alice and Bob each take one qubit of a generated EPR pair [7]. Some time later, Alice wants to send an arbitrary qubit, $|\psi\rangle$ to Bob. It's not easy for Alice to do this as she doesn't know the state of the qubit and she's only able to send classical information to Bob.
Since Alice has no other copy of the qubit, if she wants to determine its state, she has to perform a measurement on the qubit which destroys the state. Also due to no cloning theorem, she cannot copy the state. Alice can pull this impossible mission off in an elaborate way.
Alice interacts the qubit $|\psi\rangle$ with her qubit from the EPR pair she has from before. Then she measures the qubit which leads to classical results of 00, 01, 10 and 11. She sends the outcomes of the measurement to Bob over classical channels. After Bob receives the message from Alice, he performs one of four operations on his qubit which he had from EPR pair. Surprisingly, he can recover the state of the initial qubit, $|\psi\rangle$, Alice wanted to send! In figre 1.6, Quantum circuit representation of the quantum teleportation is depicted.

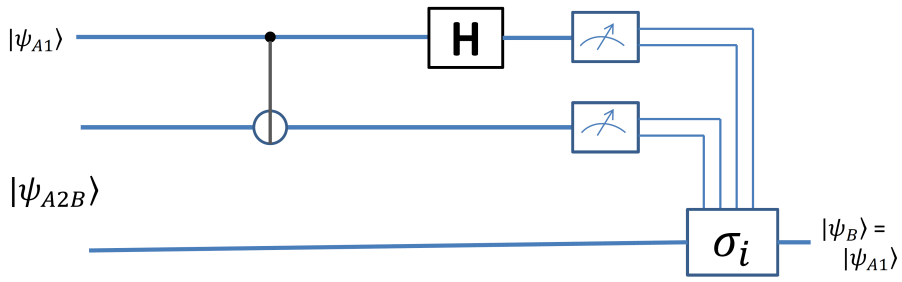

FIGURE 1.6: Quantum teleportation circuit. Classical channels are indicated with double lines.

The state $|\psi_{A1}\rangle$ is the single copy qubit that Alice wants to send:

$$|\psi_{A1}\rangle = \alpha\,|0\rangle + \beta\,|0\rangle \tag{1.18}$$

The state $|\psi_{A2B}\rangle$ is the state of the EPR qubit they initially share:

$$\frac{1}{\sqrt{2}}(|00\rangle + |11\rangle) \tag{1.19}$$

From left site of the circuit we have:

$$\begin{aligned} &|\psi_{A1}\rangle\,|\psi_{A2B}\rangle = (\alpha\,|0\rangle + \beta\,|0\rangle)\frac{1}{\sqrt{2}}(|00\rangle + |11\rangle) = \\ &\frac{\alpha}{\sqrt{2}}\,|0\rangle\,(|00\rangle + |11\rangle) + \frac{\beta}{\sqrt{2}}\,|1\rangle\,(|00\rangle + |11\rangle) \end{aligned} \tag{1.20}$$

After performing a C-Not gate and a Hadamard gate, we get to:

$$\frac{1}{\sqrt{2}}(|00\rangle\,\sigma_0\,|\psi_B\rangle + |01\rangle\,\sigma_x\,|\psi_B\rangle + |10\rangle\,\sigma_y\,|\psi_B\rangle + |11\rangle\,i\sigma_z\,|\psi_B\rangle) \tag{1.21}$$

Where σ_is are Pauli matrices. By performing a measurement on the above state in computational basis, Bob get the original state Alice wanted to send. Of course,

for performing a measurement, Bob needs to know the outcome of Alice's measurement which would be sent over classical channel.

1.2.4 Entanglement and SPDC

Entanglement is the counterpart of correlation in quantum physics. If a pair of particles are entangled, the state of the system of those two particles cannot be described by the product of the state of each particle separately.
A most common way to produce entangled pairs is the spontaneous parametric down conversion (SPDC). A nonlinear crystal is pumped by a laser to produce spontaneous down conversion. SPDC is a random process caused by vacuum fluctuations. Therefore the conversion efficiency is low. The path of down converted photons are constrained to a cone shape path. After the crystal is pumped[14], we have two beam; one is called signal and the other idler (as it is known to be present when the signal is detected). Conservation of energy impose the following rule on the pump, signal and idler (phase matching condition):

$$\begin{aligned} k_3 &= k_1 + k_2 \\ \omega_3 &= \omega_1 + \omega_2 \end{aligned} \tag{1.22}$$

Where k is the wavenumber and ω is the frequency of the photon. Indices of 3, 1 and 2 are respectively correspond to pump, signal and idler photon.
There are two types of SPDC processes, type-I and type-II. In type-I, to cones are coincide with each other and centered to the pump beam. In type-II, the cones are separated with an angle.

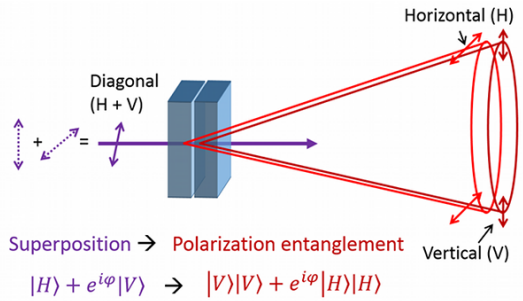

FIGURE 1.7: Type-I SPDC. [4]

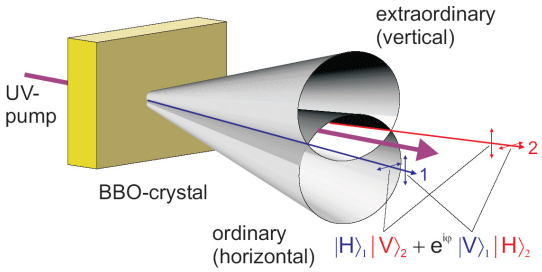

FIGURE 1.8: Type-II SPDC.[5]

[4] http://research.physics.illinois.edu/QI/Photonics/research/
[5] http://spie.org/x23635.xml?pf=true&ArticleID=x23635

1.2.5 Entanglement decoherence in a gravitational well

We can construct an experiment [18] to test gravitaional decoherence and consequently answer the question: "Is time travel allowed by the laws of physics?"
According to Einstein's theory of general relativity, it might be possible for time to form a closed loop (a closed timelike curve). In addition we need to know what happens to quantum systems when they go back in time.
Back in 1991, David Deutsch developed a model [5] which a single qubit goes back in time and interacts with itself. Two strange consequences of Deutsch's model are that, one, it's nonlinear and thus superposition principle doesn't hold anymore and two, it's non-unitary and therefore the information can be lost (like in a black hole). We can actually test the model experimentally. But first we have to overcome such obstacles as: One, it only describes non relativistic particles and two, we don't have a time machine!
The Deutsch's model can be generalized to relativistic field. We can use quantum optics since it describes the light as particles which travel at the speed of light. The generalization can be done by taking the quantum optics field operator (annihilation operator) and add an extra degree of freedom do it.

$$\bar{a}_K(x,t) = \int dk K(k) e^{ik(x-t)} \hat{a}_k \tag{1.23}$$

The event formalism generalized nonlinear operator would be:

$$\bar{a}_K(x,t,\Delta) = \int dk K(k) e^{ik(x-t)} \int d\Omega |K(\Omega)| e^{i\Delta\Omega} \hat{a}_{k,\Omega} \tag{1.24}$$

This nonlinear modification allows the operator to commute with itself after a certain amount of time has passed.

$$[\bar{a}_K(x,t,\Delta), \bar{a}^\dagger_{K'}(x',t,\Delta')] \approx 0 \quad \text{if} \quad \tau \gg \sigma \tag{1.25}$$

Where τ is the time elapsed from t (global time) until t_d (detection time of the propagating mode), as measured incrementally by a set of local observers at rest with respect to the choice of coordinates (x,t) and stationed along the semi-classical trajectory of the wavepacket. Ω is the Fourier complement of τ. Δ is the difference between t_d and $\tau(t,t_d)$.
It turns out that there's no need for time to bend all the way back on itself to see the effects of Deutsch's model.†
It's enough to look at the time dilation caused by the Earth's gravitaional field and we can see some decoherence predicted by Deutsch's model.
We can make use of entangled photons to test this decoherence. One photon of the entangled pair is detected locally and the other is send to space (to the ISS for instance). If the rate of coincidences decreases, it means that the decoherence is occured. The effect of gravity on entanglement would provide a signature of models like Deutsch's model.

1.3 Optics

1.3.1 Gaussian Optics

The Gaussian beam is a transverse electromagnetic mode (TEM). The intensity of the beam with a power P is described by a Gaussian function:

$$I(r,z) = \frac{P}{\pi w(z)^2/2} \exp\left(-\frac{2r^2}{w(z)^2}\right) \tag{1.26}$$

The beam radius, $w(z)$ is considered as the distance from the beam axis where the intensity drops to $1/e^2$ of its maximum value.
For the propagation of the Gaussian beam, we can use the *paraxial approximation* which let up omit the second-order derivative of the Maxwell's equation in the propagation equation and just dealing with a first-order differential equation[6].

$$E(r,z) = E_0 \frac{W_0}{W(z)} \exp\left(-\frac{r^2}{w(z^2)}\right) \exp\left(-i\left[kz - \arctan\left(\frac{z}{z_R}\right) + \frac{kr^2}{2R(z)}\right]\right) \tag{1.27}$$

$$w(z) = w_0 \sqrt{1 + (\frac{z}{z_R})^2} \tag{1.28}$$

$$z_R = \frac{\pi w_0^2}{\lambda} \tag{1.29}$$

$$R(z) = z\left[1 + (\frac{z_R}{z})^2\right] \tag{1.30}$$

Where E_0 is the peak amplitude and w_0 is the beam waist, k is the wavenumber, z_R is the Rayleigh length, R(z) is the radius of curvature of the wavefronts and λ is the wavelength of the monochromatic Gaussian beam.
The beam divergence for far field ($z \gg z_R$) is:

$$\theta = \frac{\lambda}{w_0 \pi} \tag{1.31}$$

In reality, a laser might not be giving a perfect focus point but a little bigger spot size and therefore smaller divergence angle. We can correct the divergence angle by adding a factor known as beam quality factor or beam propagation factor (M^2):

$$\theta = M^2 \frac{\lambda}{w_0 \pi} \tag{1.32}$$

A diffraction-limited laser beam is a laser which can be focused to a small spot as small as possible that only the intrinsic diffraction limit bound the minimum focus spot size. Then the angle would be as close as possible to the angle calculated from equation 1.31 for the given wavelength and therefore $M^2 = 1$ for that laser. Otherwise, if the laser doesn't have ideal quality and $0 < M^2 < 1$. A mixed-mode beam with a waist of M times larger than the embedded Gaussian has a divergence M times greater than the embedded Gaussian.

[6] https://www.rp-photonics.com/gaussian_beams.html

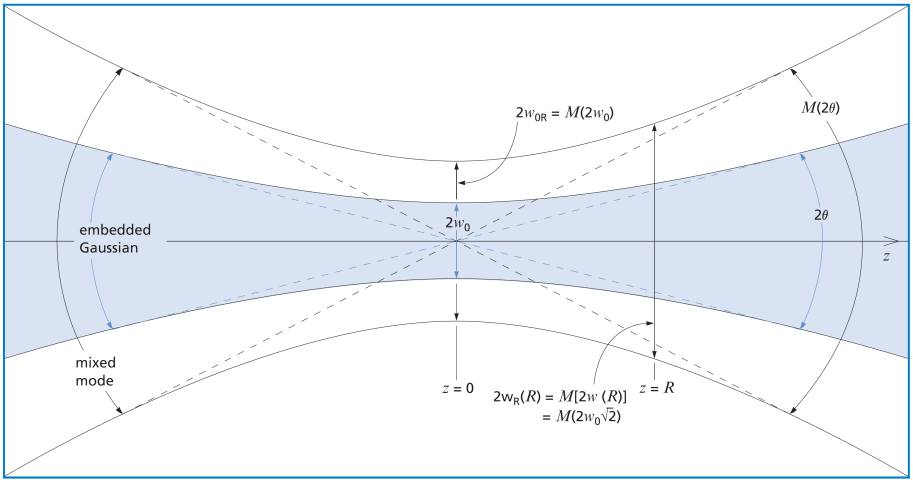

FIGURE 1.9: Propagation of a Gaussian beam. Image from *CVI Laser Optics.*

We can specify the properties of Gaussian beam at a particular point z along the axis of the beam by defining a complex parameter:

$$\frac{1}{q(z)} = \frac{1}{R(z)} - \frac{i\lambda}{\pi n w(z)^2} \tag{1.33}$$

Where n is the index of refraction of the medium beam is going through. We can use ABCD method for a Gaussian beam as the q parameter modifies by an optical element:

$$q' = \frac{Aq + B}{Cq + D} \tag{1.34}$$

1.3.2 Airy disc

As light goes uniformly through a circular aperture, it gets diffracted in a way that there is a Bright spot in the center of the diffraction pattern, called Airy disc.

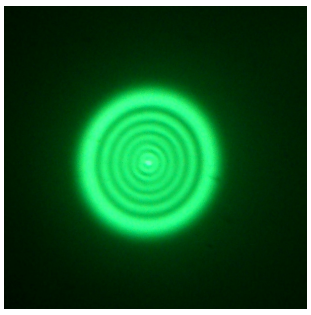

FIGURE 1.10: Airy disc formed from an infrared laser beam passing through a lens (view from infrared viewer).

The focus spot size of a lens is considered the size of the Airy disc. The intensity distribution of the Airy disc is given by:

$$I(\theta) = I_0 \Big(\frac{2J_1(ka \sin\theta)}{ka \sin\theta} \Big)^2 \tag{1.35}$$

As we have:

$$ka \sin\theta = \frac{2\pi ar}{\lambda R} = \frac{\pi}{\lambda N} \tag{1.36}$$

Then we can rewrite the distribution:

$$I(r, \varphi) = I_0 \Big(\frac{2J_1(\frac{\pi r}{\lambda N})}{\frac{\pi r}{\lambda N}} \Big)^2 \tag{1.37}$$

Where J_1 is the order-one Bessel function of the first kind. θ is the angle of observation, I_0 is the maximum intensity of the pattern (at the center of the Airy disc) and k is the wavenumber. a is the radius of the aperture, R is the observation distance, r is the radial distance from the optics axis in the observation (or focal) plane and N is the numerical aperture (see section 1.3.3).

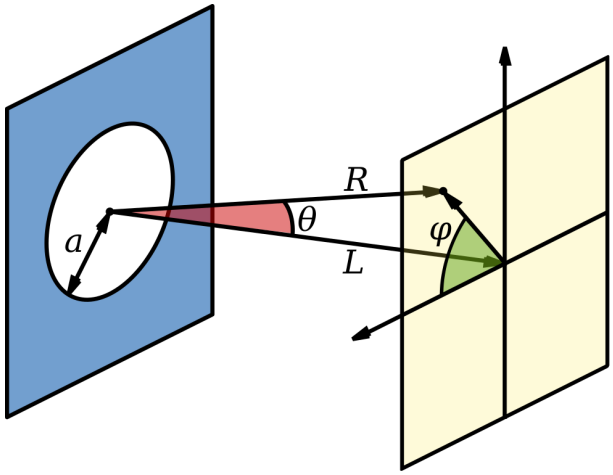

FIGURE 1.11: Far field (Fraunhofer) Diffraction from a circular aperture.

1.3.3 Diffraction Limit

In 1837, Ernst Abbe introduced a formula for the focus spot size of a beam (d) of light which travels through a medium with refractive index of n:

$$d = \frac{\lambda}{2n \sin\theta} \tag{1.38}$$

Where λ is the wavelength of the beam and θ is the converging angle.
$n \sin\theta$ is often called the numerical aperture (NA) of the optical element. Formula 1.38 is the famous Abbe diffraction limit which states that even with perfect optical elements, one cannot obtains a smaller angle of convergence and therefore the resolution is limited by this intrinsic property.
For a telescope, the diffraction limit is given by:

$$\theta = \frac{1.22 \times \lambda}{D} \quad (rad) \tag{1.39}$$

Where D is the diameter of the telescope and the factor 1.22 come from the position of the first dark circular ring surrounding the central Airy disc of the diffraction pattern (first zero of Bessel function $J_1(x)$ divided by π).

In digital photography, the diffraction limit can be calculated by:

$$d = 2 \times 1.22\,\lambda\,N \tag{1.40}$$

Where is is the focus spot size and N is the $f-$number of the imaging optics. The $f-$number is simply the ratio of the focal length and the diameter of the entrance pupil. On the various lenses such as Nikkor lenses, there are options for the $f-$number that basically by opening and closing a diaphragm, one can change the effective aperture and therefore the $f-$number.

1.3.4 Polarization

One of the fundamental properties of light is the polarization. Light is an electromagnetic Field which is consisted of an electrical field and a magnetic field. These two fields are perpendicular to each other and oscillate as they propagate. The Direction of electric field indicates the polarization. Light is a traverse wave, i.e. the oscillation is perpendicular to the propagation. Two components of the electric field are depicted in the following graph[7]:

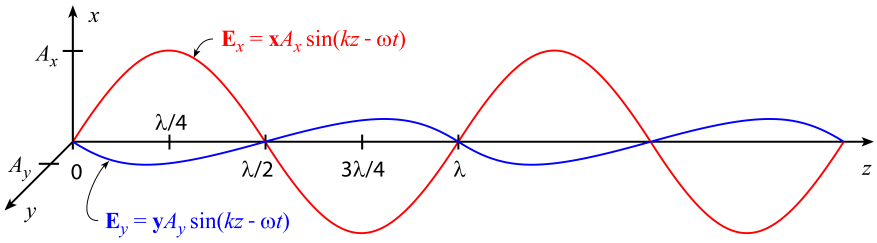

FIGURE 1.12: E_x and E_y component of the electric field.

The components shown in the figure 1.12 are the real part of the solution of the Maxwell's equation for the electric field. In general we can write the complex solutions as the following:

$$\begin{aligned} E_x &= \hat{x}\,A_x\,e^{i(kz-\omega t+\varphi_x)} \\ E_y &= \hat{y}\,A_y\,e^{i(kz-\omega t+\varphi_y)} \end{aligned} \tag{1.41}$$

Then the electric field vector would be:

$$\begin{aligned} \vec{E} &= \vec{E_0'}e^{i(kz-\omega t)} \\ \text{where} \quad \vec{E_0'} &= (\hat{x}\,A_{0x}\,e^{i\varphi_x} + \hat{y}\,A_{0y}\,e^{i\varphi_y}) \end{aligned} \tag{1.42}$$

Note that we separated the oscillating part and E_0' does not oscillate anymore and indicates the phase and the amplitude in x and y direction which fully determines the state of polarization. The vector E_0' is called the *Jones* vector. The state of the polarization can be represented by the Bloch sphere:

[7] Semrock Optics - Understanding Polarization

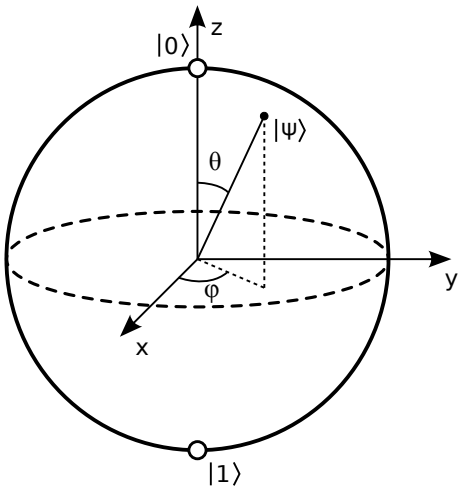

FIGURE 1.13: Bloch sphere.

The general state of the polarization cab be written as:

$$\begin{aligned} |\psi\rangle &= \cos\frac{\theta}{2}\,|0\rangle + e^{i\varphi}\cos\frac{\theta}{2}\,|1\rangle \\ |0\rangle &\equiv |H\rangle \quad ; \quad |1\rangle \equiv |V\rangle \end{aligned} \tag{1.43}$$

Figure 1.12 demonstrate a Linear polarization and A_x should not necessarily be equal to A_y but their relative phase should be zero.
In case of an elliptical polarization, there's a relative phase between E_x and E_y and $A_x \neq A_y$. Thus we would have the following for the electric field components:

$$\begin{aligned} E_x &= \hat{x}\, A_x\, \sin(kz - \omega t + \delta) \\ E_y &= \hat{y}\, A_y\, \sin(kz - \omega t) \end{aligned} \tag{1.44}$$

In a special case which $\delta = 0$, we obtain a linear polarization and in the other special case where $\delta = \pm\frac{\pi}{2}$ and $A_x = A_y$, we would have a circular polarization.
Here are 6 most common polarization states and their corresponding normalized Jones vectors:

$$\begin{aligned} \text{Linear; Horizontal: } |H\rangle \equiv |0\rangle &\mathrel{\widehat{=}} \begin{pmatrix} 1 \\ 0 \end{pmatrix} \\ \text{Linear; Vertical: } |V\rangle \equiv |1\rangle &\mathrel{\widehat{=}} \begin{pmatrix} 0 \\ 1 \end{pmatrix} \\ \text{Linear; Diagonal}(+45^\circ)\text{: } |D\rangle = \frac{1}{\sqrt{2}}(|H\rangle + |V\rangle) &\mathrel{\widehat{=}} \frac{1}{\sqrt{2}} \begin{pmatrix} 1 \\ 1 \end{pmatrix} \\ \text{Linear; Anti-diagonal}(-45^\circ)\text{: } |A\rangle = \frac{1}{\sqrt{2}}(|H\rangle - |V\rangle) &\mathrel{\widehat{=}} \frac{1}{\sqrt{2}} \begin{pmatrix} 1 \\ -1 \end{pmatrix} \\ \text{Right Hand Circular Polarized: } |R\rangle = \frac{1}{\sqrt{2}}(|H\rangle + i\,|V\rangle) &\mathrel{\widehat{=}} \frac{1}{\sqrt{2}} \begin{pmatrix} 1 \\ +i \end{pmatrix} \\ \text{Left Hand Circular Polarized: } |L\rangle = \frac{1}{\sqrt{2}}(|H\rangle - i\,|V\rangle) &\mathrel{\widehat{=}} \frac{1}{\sqrt{2}} \begin{pmatrix} 1 \\ -i \end{pmatrix} \end{aligned} \tag{1.45}$$

1.3.5 Qubit

Classical information and classical computation is built upon a fundamental concept called bit. Its counterpart in quantum information and quantum computation is known as quantum bit or simply, qubit. In classical case we have 0 and 1 as a bit, but in quantum case, in addition we can also have a superposition of 0 and 1. This ability makes the quantum computers distinct and more powerful than ordinary computers. Qubits use the dirac notation known as Kets and Bras.
A single qubit can be written as:

$$|\psi\rangle = \alpha\,|0\rangle + \beta\,|1\rangle \tag{1.46}$$

Where α and β are complex numbers which satisfy: $|\alpha|^2 + |\beta|^2 = 1$. We can again use the bloch sphere to represent the state of the qubit (eq.1.43) as depicted in Figure 1.13. Information is embedded in a qubit via using polarization for instance.
As qubit is a unit of quantum information in a 2-level quantum system, qutrit is a unit of quantum information in a 3-level quantum system and a general term for a unit of quantum information in a d-level quantum system is qudit. According to 4^{th} postulate of quantum mechanics, the state of a n qubit system could be described as the tensor product of the state of each qubit. For instance, the general state of a two qubit system would be:

$$|\psi\rangle = \alpha_{00}\,|00\rangle + \alpha_{01}\,|01\rangle + \alpha_{10}\,|10\rangle + \alpha_{11}\,|11\rangle \tag{1.47}$$

Most common and simple bipartite entangled states are the following Bell states:

$$\begin{aligned}
\left|\Phi^+\right\rangle &= \frac{1}{\sqrt{2}}(|00\rangle + |11\rangle) \\
\left|\Phi^-\right\rangle &= \frac{1}{\sqrt{2}}(|00\rangle - |11\rangle) \\
\left|\Psi^+\right\rangle &= \frac{1}{\sqrt{2}}(|01\rangle + |10\rangle) \\
\left|\Psi^-\right\rangle &= \frac{1}{\sqrt{2}}(|01\rangle - |10\rangle)
\end{aligned} \tag{1.48}$$

These states are frequently used in quantum information science.

Chapter 2

Missions Possible

2.1 Proposals on space experiments

There are different space proposals for quantum related experiments such as Quantum cryptography (e.g. QKD), Bell test experiments and closing loopholes, Wave function collapse, gravitational decoherence in a gravitational well, etc.

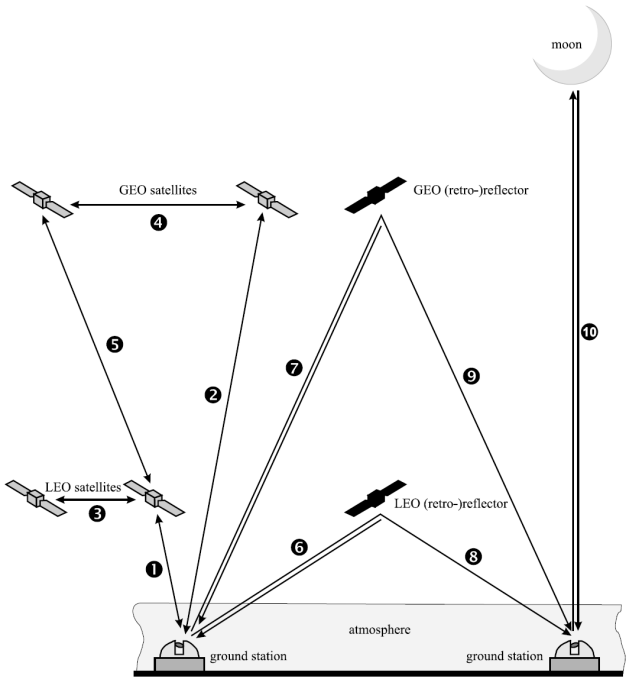

FIGURE 2.1: Different types of free space communication. Figure from [2]

1. ground $\leftrightarrow$ LEO link, (link distance: $\sim$ 500 km)
2. ground $\leftrightarrow$ GEO link, (link distance: $\sim$ 36000 km)
3. LEO $\leftrightarrow$ LEO link, (link distance: $\sim$ 2000 km)
4. GEO $\leftrightarrow$ GEO link, (link distance: $\sim$ 40000 km)
5. LEO $\leftrightarrow$ GEO link, (link distance: $\sim$ 35500 km)
6. ground $\rightarrow$ LEO retro-reflector $\rightarrow$ ground link,
7. ground $\rightarrow$ GEO retro-reflector $\rightarrow$ ground link,
8. ground $\rightarrow$ LEO reflector $\rightarrow$ ground link,
9. ground $\rightarrow$ GEO reflector $\rightarrow$ ground link,
10. ground $\rightarrow$ moon-based retro-reflector $\rightarrow$ ground link.

2.2 Attenuation of the link

In free-space communications the attenuation of the link is more significant than fiber based communications. Reliable quantum communication protocols require single photon detection which is synchronized with the transmitter (e.g. in single qubit QKD like BB84) or with a distant detector (e.g. in entanglement based QKD like Ekert protocol or a violation of Bell's inequality). This synchronization leads to intrinsic error rate in detection process and since high error count rate makes the QKD vulnerable to eavesdropper more fundamentally prevents the violation of Bell's inequality by reducing the two-photon interference visibility below the classical field theory limit. These reasons limit the maximum affordable loss of signal.
Maximum acceptable attenuation for entanglement based communications is determined by the timing resolution and the dark counts rates f the detectors and also the count rate of the source. In a spontaneous parametric down conversion, the entangled photons would have a wavelength of 800 nm if pumped with a 400 nm laser. For 800 nm, Alice and Bob use silicon avalanche photodiodes which typically has a timing jitter of 500 ps and dark count rates of 50 Hz. The accidental coincident rate is given by[2]:

$$C_{acc} = S_1 S_2 \Delta\tau \tag{2.1}$$

Where the S_1 and S_2 are the dark count rates of the Alice's and BOB's detector and $\Delta\tau$ is the timing jitter of the detectors. A minimum of 71% (corresponding to a SNR of 6:1 [1]) for the two fold coincidental visibility is needed to violate the Bell's inequality. This means that minimum coincidences should be 6 times greater than the background coincidences.
Coincidence detection efficiency of the whole link η is the product of the efficiencies of each qubit link ($\eta_1$andη_2):

$$\eta = \eta_1 \times \eta_2 \tag{2.2}$$

And the detected coincidences would be:

$$C = P \times \eta \times \eta_{det1} \times \eta_{det2} \tag{2.3}$$

Where P is the pair production rate of the source and η_{det1} and η_{det2} are the efficiencies for each detector.
As mentioned earlier, we should have:

$$C_{min} \geqslant SNR \cdot C_{acc} \tag{2.4}$$

Which leads to:

$$\eta \geqslant SNR \times \frac{S_1 S_2 \Delta\tau}{P \eta_{det1} \eta_{det2}} \tag{2.5}$$

The attenuation factor of a link is given by:

$$A = P_T/P_R = \frac{L^2 \lambda^2}{D_T^2 D_R^2 T_T (1 - L_P) T_R} \tag{2.6}$$

[1] Visibility= $\frac{SNR}{SNR+2}$

Where P_T is the optical power of the transmitter and P_R is the power received by the receiver, L is the link distance, λ is the wavelength of the link and D_T and D_R are respectively the diameters of transmitting and receiving telescope. T_T and T_R are the transmission factor of the transmitting and receiving telescope and L_P is the pointing loss due to misalignment of transmitter and receiver. The following assumption were made for derivation of the latter formula[2]:

1. L $\geqslant D_T^2$,
2. Transmitting telescope is diffraction limited,
3. Atmosphere do not affect by any means.

2.2.1 Ground to space link

In the case of ground to space links, we would have additional attenuation due to the atmosphere's variations in temperature (and thus density). The diffraction limit of the telescope would be increased and an *effective aperture* could be assigned depending on the *Fried parameter*, r_0.
Fried parameter is actually defined as the diameter of a circular area over which the RMS wavefront aberration due to passage through the atmosphere is equal to 1 radian. The modified attenuation factor would be[2]:

$$A = \frac{L^2(\theta_T^2 + \theta_{atm}^2)}{D_R^2 T_T (1 - L_P) T_R} 10^{A_{atm}/10} \tag{2.7}$$

Where A_{atm} is the attenuation factor due to atmosphere in decibel. θ_T [13] and θ_{atm} are respectively the divergence angle of transmitting telescope and the divergence angle caused by atmospheric turbulence.

$$\theta_T = 1.27 \cdot \frac{\lambda}{D_T} \qquad \text{(GAUSSIAN BEAM)} \tag{2.8}$$

$$\theta_{atm} = \frac{\lambda}{r_0} \tag{2.9}$$

Fried parameter could be calculated with the following formula:

$$r_0 = [0.423 k^2 (\sec z) \int C_N^2(h) dh]^{-3/5} \tag{2.10}$$

Where k is the wavenumber ($k = \frac{2\pi}{\lambda}$), and $C_N(h)$ is the atmospheric turbulence strength as a function of height (h). Parameter z is the zenith angle.
From equation 2.7, the we see that: $r_0 \propto \lambda^{6/5}$.

Links using retroreflector

If we use a retroreflector with diameter of D_{retro} located in distance L from the transmitter and receiver, the attenuation factor could be modified as [2]:

$$A = \frac{L^2(\theta_T^2 + \theta_{atm}^2)}{D_{retro}^2 T_T (1 - L_P) T_R R_{retro} D_{retro}^2 D_R^2} 10^{A_{atm}/5} \tag{2.11}$$

Where R_{retro} is the effective reflectivity of the retro reflector.

2.3 NightPod and the ISS Infrastructure

2.3.1 NightPod

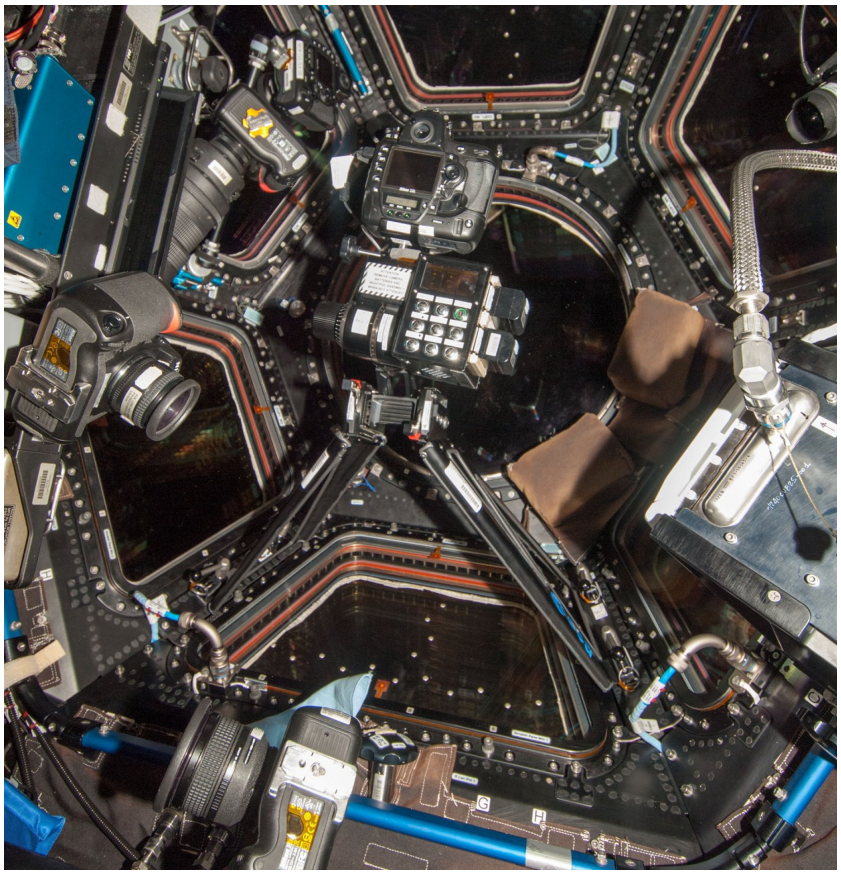

FIGURE 2.2: NightPod installed in Cupola during expedition 30 -31 with a Nikon D3s camera. Figure from [6]

In order to take sharp pictures, one should have steady hands or a nice Mount. It becomes even more crucial when shooting in the dark!
Thanks to Cupola module (see section 2.3.3), now it's a lot easier for astronauts to acquire images from Earth. But they still face the challenge of shooting in the dark. Even using high ISO setting is not quite enough. One should use rather long exposures. Regarding the movement of ISS, the relative movement of earth underneath the ISS is about 28000 km/h and makes it hard to use longer exposures. The image would be blurred. Cosine research B.V. designed and manufactured a mount which is motorized and compensates for the relative rotation of the Earth and lets astronauts to take sharp images with longer exposure time.
The NightPod is already on board the ISS. It's designed to be installed in Cupola with three adjustable axes (figure 2.4), a single motorized rotary stage with a micro-stepper motor, controlled by an onboard computer.
The schematic of the NightPod is illustrated in figure 2.3.

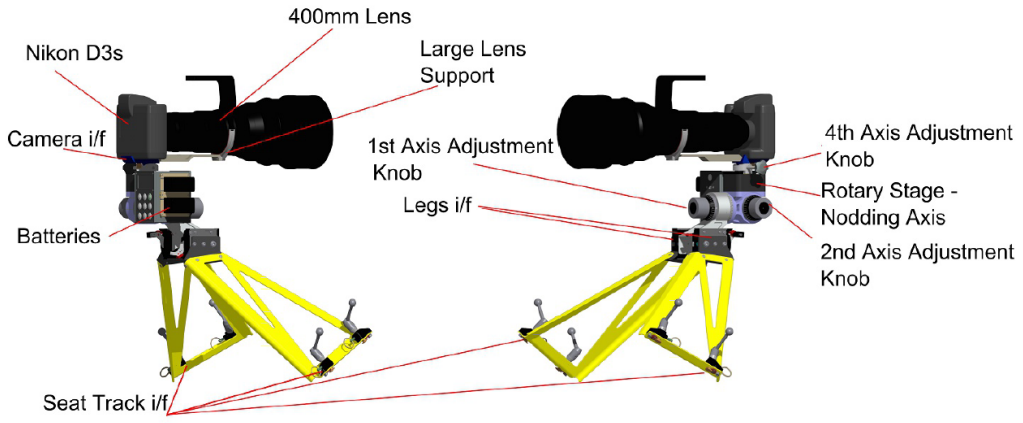

FIGURE 2.3: NightPod schematic with Nikon 400mm lens and a Nikon D3s DSLR installed. Figure from [9]

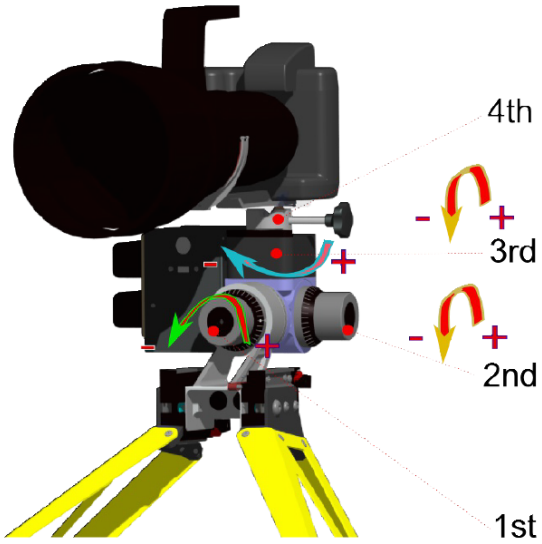

FIGURE 2.4: NightPod axes. Figure from [9]

Astronauts can operate NightPod via its user interface (Figure 2.5). Following installation in Cupola, the astronauts align the NightPod axes based on the current ISS altitude and latitude information. The ISS altitude and pitch/roll/yaw angles are inserted into the NightPod computer, which is able to calculate the rotation angle of each axis in order to have the NightPod fully aligned with the station velocity vector.

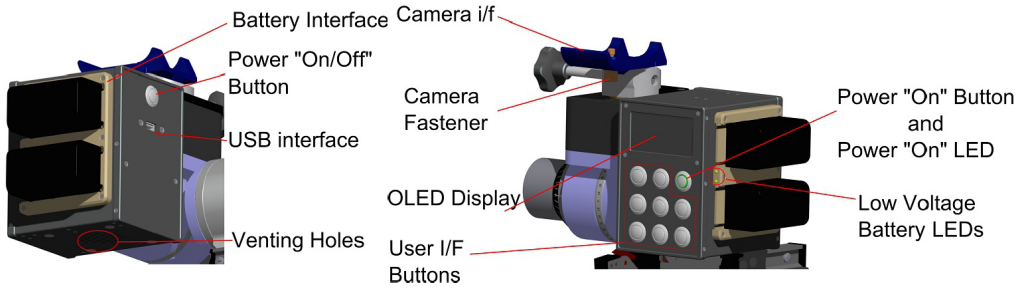

FIGURE 2.5: NightPod's user interface. Figure from [9]

The NightPod is equipped with four axes as show in Figure 2.4: the motorized axis (nodding axis) is aligned perpendicular to the flight direction.
These four axes are as follows:

- Axis 1: Yaw - ρ (Manually controlled)
- Axis 2: Roll - κ (Manually controlled)
- Axis 3: The nodding axis (pitch - δ)
- Axis 4 (non-Eclidean): Manual roll - κ_m

Astronauts can use the values computed by the NightPod's computer and align the mount. The knob drives the axis via a harmonic drive that has a fixed gear ratio of 1:100, i.e. one full revolution of an axis knob will change the axis angle by $3.6°$. The angle of each of the two Eulerian axes is indicated by two separate scales, a major and a minor scale. The minor scale consists of 36 minor ticks, so that changing the axis from one minor tick to the next will change the axis angle by $0.1°$. Locating the mid-point between two minor ticks can obtain a pointing precision of $\sim 0.05°$. The major scale shows the angle in steps of $1°$ and it is used as a reference[6].
For tracking a point on Earth from ISS, an angular rate of about $1° \ s^{-1}$ to $1.4° \ s^{-1}$ is required. The tracking stability of the Nightpod motorized axis has been measured during the NightPod development by the developing company[6] using a lens with focal length of 400 mm and a detector with pixel pitch of 8.45 μm. The results are gathered in table 2.1.

test #	angular rate [°/s]		deviation [%]	RMS stability [arcsec]
	(setting)	(measured)		
1	0.1	0.1	-2.5	7.8
2	0.5	0.49	-2.6	4.8
3	1	0.97	-3.1	5.2
4	1.5	1.46	-2.9	7

TABLE 2.1: Results of stability measurements of the rotational stage. Table from [6].

The Earth Spins around itself every 24 for hour and ISS Orbit the Earth every one and a half hours. If we neglect the Earth's rotation, then the tracking axis (pitch axis in the ISS-centered reference frame) is perpendicular to the V_{ISS} vector. The tangential velocity of earth at the equator is:

$$V_{E_{eq}} = R_{E_{eq}} \times \omega_E = 464.58 \quad m/s \tag{2.12}$$

Where $R_{E_{eq}}$ is Earth's radius at equator and ω_E is the angular velocity of earth. The Tangential velocity For the Teide observatory at Tenerife (latitude = $28.3°$) is:

$$V_{Teide} = R_E \times \cos(latitude) \times \omega_E = 409.05 \quad m/s \tag{2.13}$$

Regarding $51.6°$ inclination of ISS, the tangential velocity of Teide from ISS reference frame would be:

$$(V_{Teide})_{\text{ISS}} = V_{Teide} \times \cos(51.6°) = 254.08 \quad m/s \tag{2.14}$$

If we assume ISS is orbiting in 400 km, the angular separation per second would be: $0.03638 \ °/s$ or $130.97 \ arcsec/s$. We cannot compensate for Earth's rotation using only one axis of NightPod.
The NightPod available imagery is limited to a few images and they're not well documented. To examine the quality of NightPod's performance, three set of five images were overlaid. Unfortunately the exposure time setting of acquisition of these images are unknown.
Nonetheless, the effect of the ISS motion and the Earth rotation is illustrated in figure 2.7. The overlaid images are shifted with respect to each other along the ISS direction and they appear to be rotated by the Earth rotation, as expected.

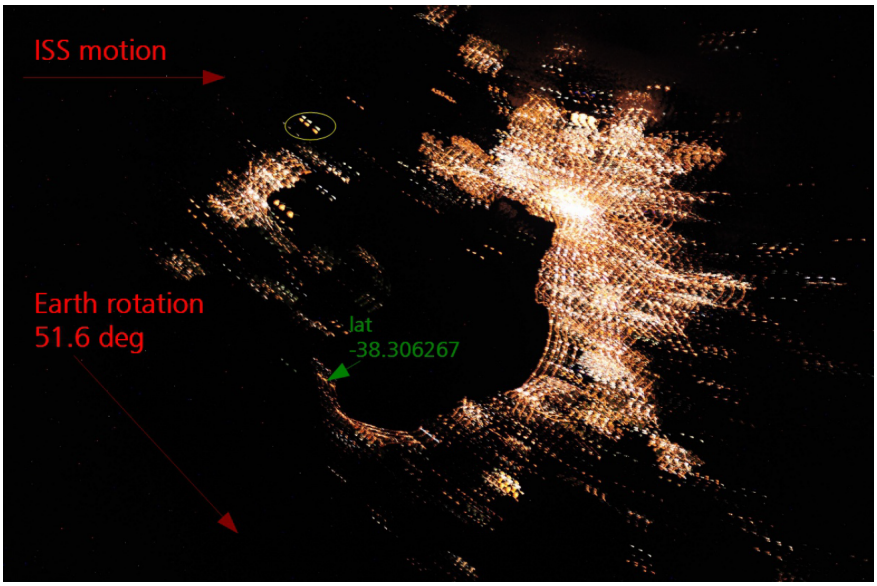

FIGURE 2.6: Overlay of 3 sets of 5 images at different integration time over Melbourne, Australia. Figure from [9]

As a qualitative analysis, we assume that the images were taken in three different sweeps by the NightPod in automatic mode. Automatic mode allows images to be taken in a sequence with a user defined amount of overlap. Each sweep lasts about 14 seconds and the time between each sweep is unknown.

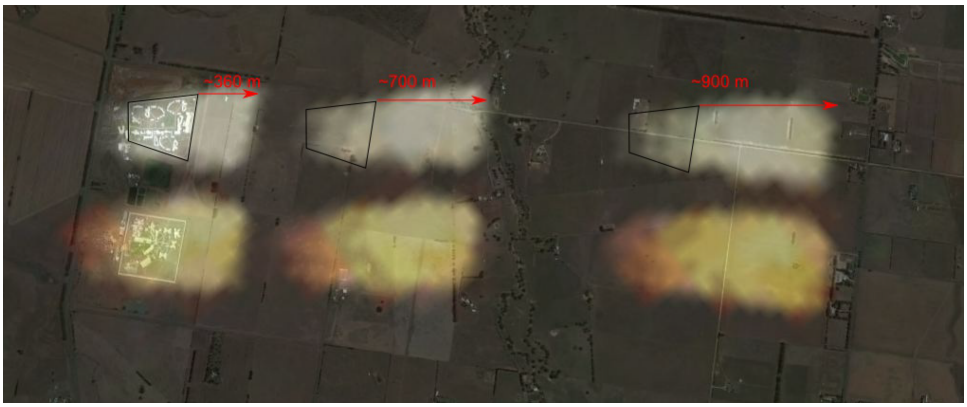

FIGURE 2.7: Detail of the overlaid image sets. Figure from [9]

Here are the measurement results of the shifts during the 3 sweeps:

Sweep sets	Shift between the first and fifth images of each set		
	Total shift	Total angular displacement	Angular displacement per sec
1	∼360 m	∼180 arcsec	∼13 arcsec/sec
2	∼700 m	∼340 arcsec	∼24 arcsec/sec
3	∼900 m	∼440 arcsec	∼31 arcsec/sec

TABLE 2.2: Earth rotation shift in 3 subsequent NightPod sweeps. Table from [9].

Since these results are better than the theoretical error for the case that the Earth's rotation is not compensated by proper setting of the Yaw axis, there's a high chance that the astronauts has corrected the Earth's rotation effect.

2.3.2 International Space Station

International space station is the most expensive international cooperation and the biggest object currently in orbit. On the 20th of November 1998, the first element of the ISS, the Russian Control Module "Zarya", was launched. Since then, various elements where launched and attached to the ISS. On Monday, May 16, 2016 at 06:10' GMT, the ISS began it's 100000th orbit as it crossed the equator.
There are 15 main pressurized modules attached to the ISS[2]. The atmosphere on board the ISS is similar to the Earth's. Double sided solar panels provide the electricity for the ISS. There are rechargeable nickel-hydrogen batteries to compensate for the lack of solar energy as the Earth blocks the sun for almost a third of an orbit ($\sim$ 30 minutes). Radio communications provide links between the station and Mission Control Centers for communications such as sending scientific data or audio-video communication between crew members, flight controllers and family members of astronauts. International space station is consisted of different parts which most of them are added during the years after the launch. Figure 2.8 shows different parts of the ISS.

[2]By the end of May, 2016.

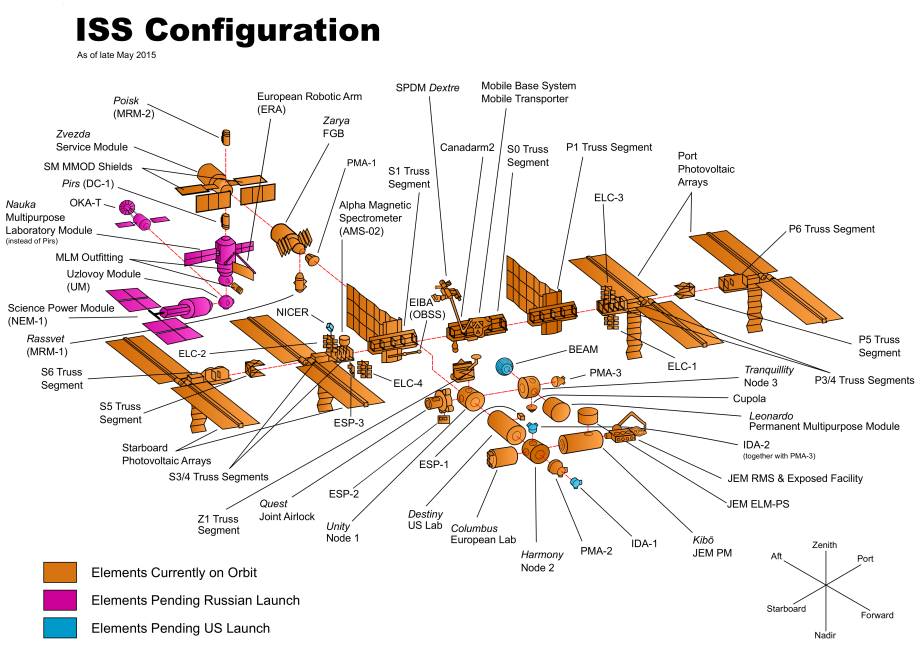

FIGURE 2.8: International space station elements.[3]

ISS orbits in an inclination of $51.6°$ and altitude between 330 km and 430 km. The main benefit of raising the station's altitude will be to cut the amount of fuel needed to keep it there by more than half. When solar activity rises, the atmospheric density increases and dragging the ISS more and costing more fuel for ISS to keep the pace. Smaller variations in ISS height is due to continual collisions of the ISS with gas particles in thermosphere and then a reboost via thruster burn brings it back to the orbit. Here's a graph showing the height of ISS over one year:

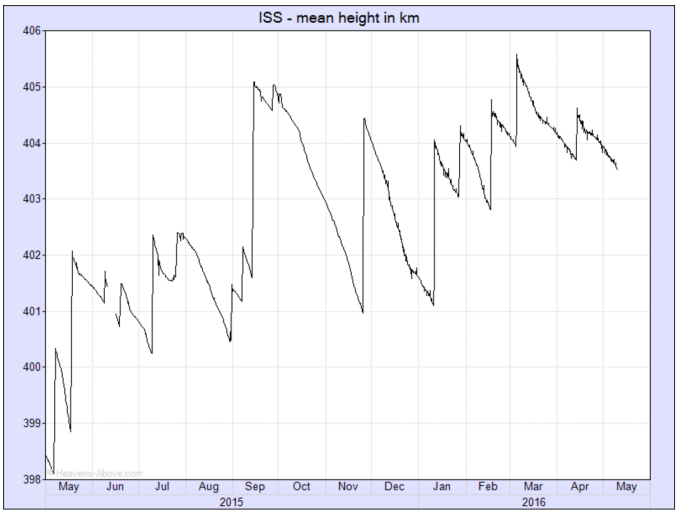

FIGURE 2.9: International space station height variation over one year. [4]

[3] https://en.wikipedia.org/wiki/Assembly_of_the_International_Space_Station

[4] http://www.heavens-above.com/IssHeight.aspx

The height is averaged over one orbit, that's why it's seen as jumps. But actually the increment happens gradually in one orbit. The gradual decrease is caused by atmospheric drag (thermosphere). Also the rate of descent is not constant due to changes in the density of the tenuous outer atmosphere caused mainly by solar activity.
The maximum specified variations of ISS attitude are gathered in the following table:

Parameters	***Characteristics***
Nominal Attitude	XVV (station x-axis toward the velocity vector).
Range of Operational Attitude	Roll, Yaw : +15 deg to -15 deg. Pitch : +10 deg to -20 deg.
Attitude Control Accuracy	$\pm$ 5 deg per axis (compared with the commanded values). $\pm$ 3.5 deg per axis (controlling to TEA).
Attitude Change Rate	Within $\pm$ 0.02 deg/s per axis (except during microgravity operations). Within $\pm$ 0.002 deg/s per axis (during microgravity operations).
Attitude Estimation Accuracy	0.5 deg per axis (3 σ) 0.01 deg/s per axis (3 σ)

TABLE 2.3: ISS altitude variation.[1]

Where:

- XVV attitude mode : X-axis in the Velocity Vector
- TEA attitude mode : Torque Equilibrium Attitude

Tranquility

Tranquility (aka Node 3) is a module of ISS which was built in a cooperation between ESA and Italian Space Agency by a Franco-Italian aerospace manufacturer, Thales Alenia Space. On November 20, 2009, the ownership was transferred to NASA. On February 8, 2010, NASA launched the Tranquility module on the Space Shuttle's STS-130 mission and docked on 12th of February, 2010. The pressurized section provides additional room for crew members and many of the space station's life support and environmental control systems on board. These systems include air revitalization, oxygen generation and water recycling. A waste and hygiene compartment and a treadmill also are located there [5].

2.3.3 Cupola

The Cupola is an observatory module connected to the Tranquility. Cupola was built by ESA and sent to ISS along side with the tranquility module. It was later transferred to the nadir-facing port of Tranquility by a robot arm[6] (Canadarm2), once Tranquility had been berthed to the Unity Module of the ISS (See figure 2.9).

[5] https://www.nasa.gov/mission_pages/station/structure/elements/tranquility.html

[6] http://www.nasa.gov/mission_pages/station/structure/elements/mss.html

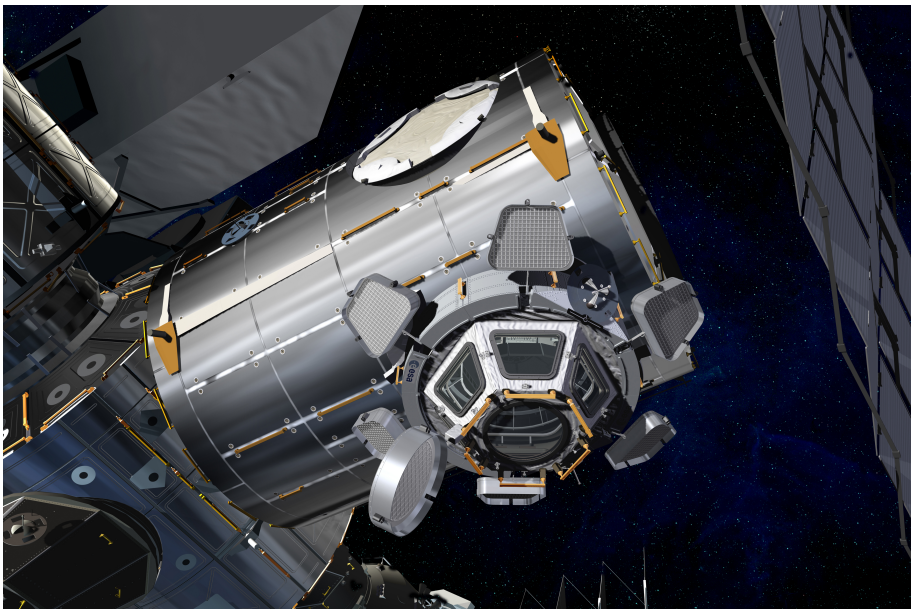

FIGURE 2.10: Cupola module attached to Tranquility.[7]

Huge windows of Cupola, especially the 70.6 cm front window, allows astronauts to take astonishing pictures from Earth. It also provides good opportunities for scientists to perform experiments such as quantum communication.

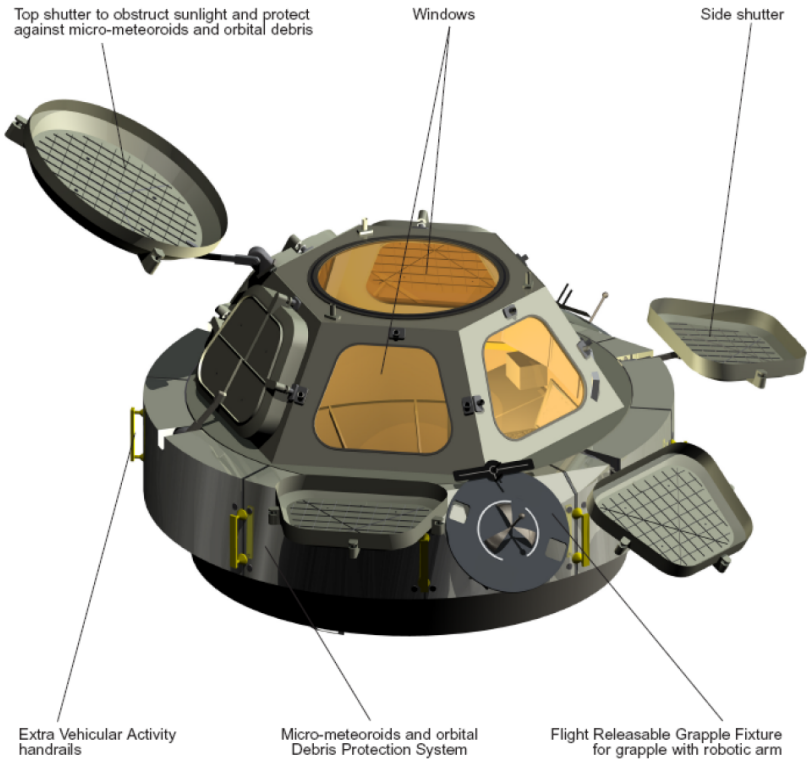

FIGURE 2.11: Cupola module windows. Picture from [1]

[7] ESA - D. Ducros, 2010

Cupola Window Physical Characteristics[1]:

□ Circular Top window (1x):

- Diameter (transparent area): 27.8 in. (70.6 cm)
- Overall thickness 8.18 in. (20.8 cm)

□ Trapezoidal Side windows (6x):

- Height (transparent area): 15.94 in. (40.5 cm)
- Short side length (transparent area): 15.75 in. (40.0 cm)
- Long side length (transparent area): 24.96 in. (64.4 cm)
- Overall thickness 7.28 in. (18.50 cm)
- Corner radius: 1.28 in. (3.24 cm)

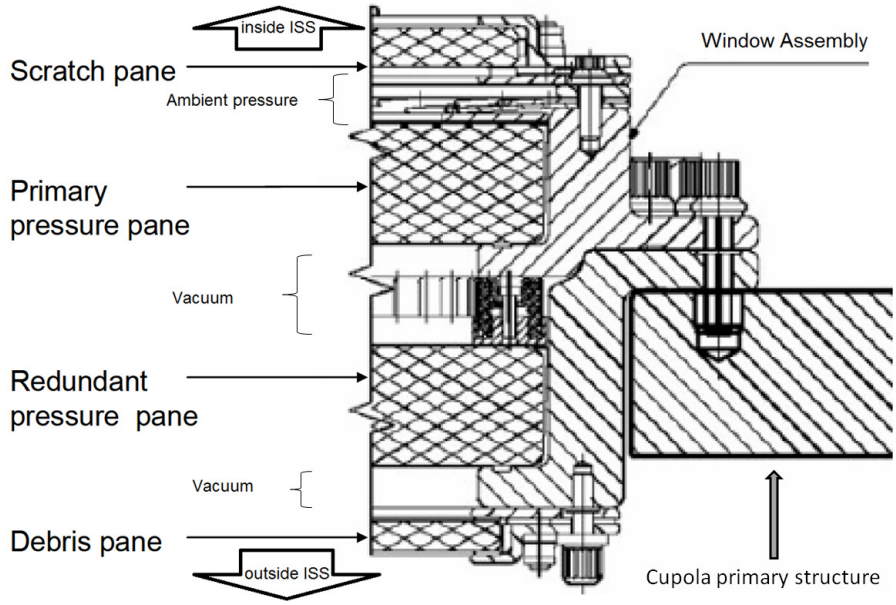

FIGURE 2.12: Cupola window cross section. Figure from [1] (modified)

The following requirements were considered for the production of the Cupola window:

□ **Surface Reflections**:

- Anti–Reflection Coatings SHALL not cause *resolution degradation* exceeding 0.007 mrad (1.5 arcsec).
- Window panes SHALL be designed such that *specular reflectance* from each anti–reflection coated surface, disregarding red–reflector coated surfaces, for 450 to 700 nanometers normally incident light SHALL not exceed 2.0 percent absolute.

□ **Optical Characteristics**:

- *Deviation* at any point on the non–tempered window panes SHALL not exceed 1.45 mrad (5 arcmin). Deviation at any point on the window panes SHALL not exceed 2.9 mrad (10 arcmin) for tempered panes.
- *Distortion* of all type window materials SHALL not exceed a plane slope of 1:24.
- *Haze* of uncoated window panes for all thicknesses SHALL not be greater than 2 percent.
- All glass window panes SHALL not exhibit *warp* and *bow* greater than 0.030 inch per [linear] foot of glass.
- *Parallelness* – The innermost surface of the inner pane and the outermost surface of the outer pane of the window system SHALL not be more than 3.0 degrees from parallel. Adjacent panes of a multipane window SHALL be between 0.1 to 0.3 degrees from parallel.

□ **Optical Transmittance**:

- *Infrared*→ The transmittance SHALL be less than 10.0 percent for wavelengths between 1000 and 850 nanometers.
- *Visible* → The transmittance SHALL be not less than 60.0 percent for wave lengths between 800 and 450 nanometers. The transmissivity SHALL not vary more than 25 percent for incident angles ranging from 30 to 45 degrees as measured from a normal to the surface.
- *Ultraviolet* → The transmittance SHALL be less than 0.1 percent for wavelengths between 320 and 280 nanometers. The transmittance SHALL be less than 0.01 percent for wavelengths between 280 and 220 nanometers.

In the following, the transmission of each pane of Cupola window is depicted[1]:

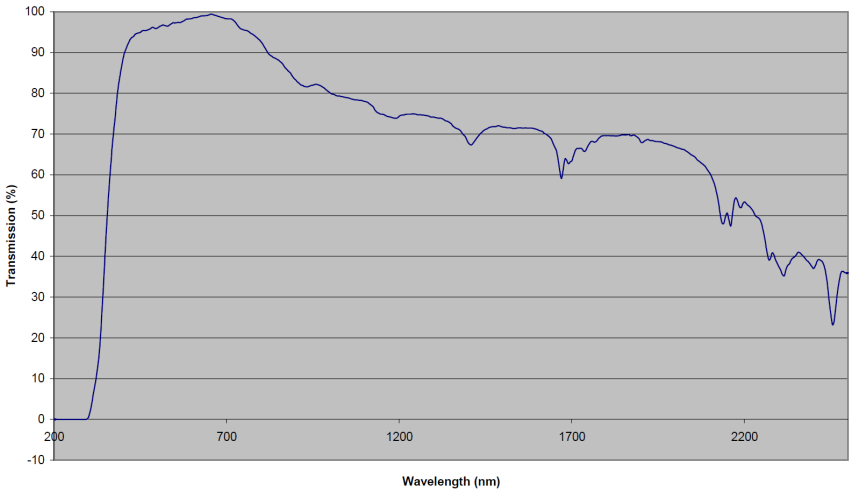

FIGURE 2.13: Cupola Scratch Pane Transmission.

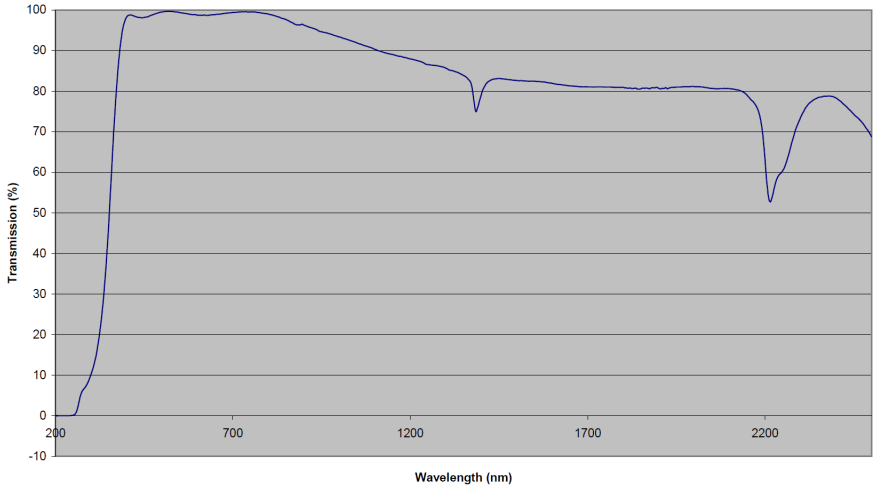

FIGURE 2.14: Cupola Debris Pane Transmission.

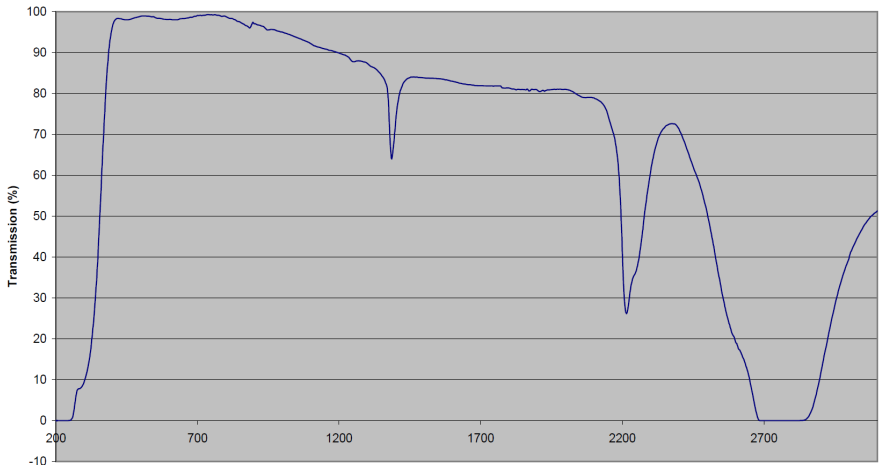

FIGURE 2.15: Cupola Pressure Pane Transmission.

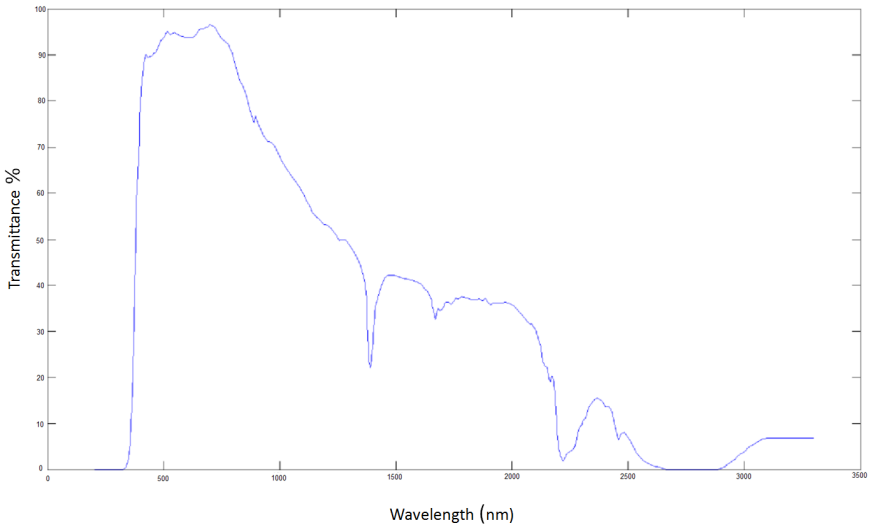

FIGURE 2.16: The total transmittance of the 4 layers of central window of Cupola[9].

The actual transmittance might be less than the measured transmittance due to lots of scratches on the window glasses of Cupola (after taking the atmosphere loss into account). Because of high velocity (up to 7800 m/s) and therefore high momentum of the debris, any object larger than 1cm could penetrate the shields of the Station's crew modules, and anything larger than 10 cm could potentially shatter a satellite or spacecraft into pieces and at this scale conjunction assessments and collision avoidance maneuvers are performed. DoD's (Department of Defense) Space Surveillance Network tracks discrete objects as small 5 centimeters in diameter in low Earth orbit and about 1 meter in geosynchronous orbit[8]. The following picture shows the result of debris impact with a size of no bigger than a few thousandths of a millimeter in diameter[9]. The dent is 7 mm in diameter.

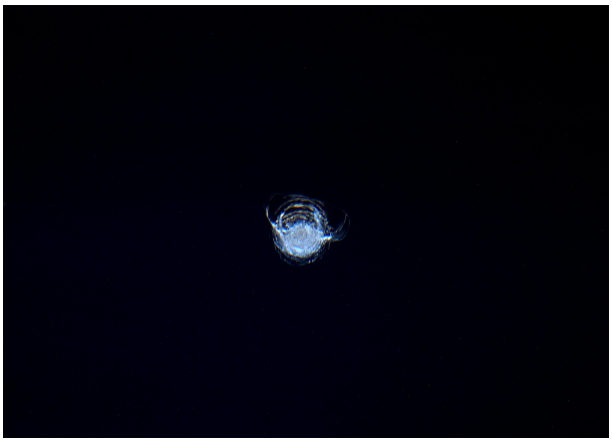

FIGURE 2.17: Impact chip and the caused dent into Cupola's window. Dark space in the background. Credit: ESA astronaut Tim Peake (Released 12/05/2016).

This is why the space debris/trash is a great concern. The impact of respectively large object can have devastating aftermath. Also the small debris are dangerous due to their momentum and they cannot be tracked by control stations. Hopefully by the time of the experiment, the windows of cupola be intact and in shape!

2.3.4 WORF

In addition to Cupola, there's a 51 cm (in diameter) window installed in Destiny module of the ISS that faces the Earth. Like Cupola's window, this window also has four layers consisting a debris pane, two pressure panes and a scratch pane. In front of this window a unique Rack is permanently installed, called *The Window Observational Research Facility* or (WORF). Experimental instruments can be installed in front of the lab window in the WORF rack which protects the window. WORF not only provides the necessary access to the window itself but also the power, data, cooling and mounting connections required for science instruments to operate[10]. The payload volume can be sealed by the installation of a hatch.This hatch prevents the on board light to reach the payload volume.

[8] http://www.nasa.gov/mission_pages/station/news/orbital_debris.html
[9] http://www.esa.int/spaceinimages/Images/2016/05/Impact_chip
[10] https://worf.msfc.nasa.gov/

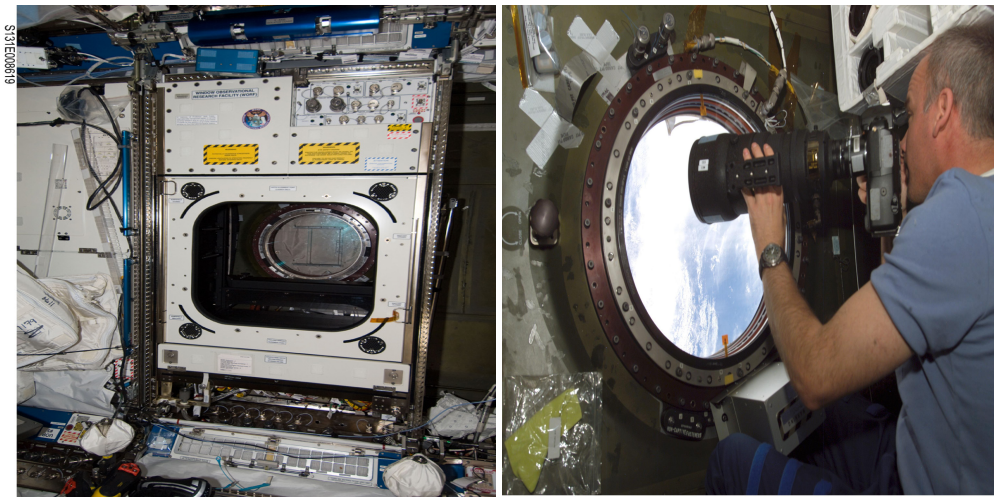

FIGURE 2.18: Left: WORF rack installed in front of Destiny's 51 cm window. Right: Jeff Williams in front of the U.S. Laboratory Science Window before WORF installation. Credit: NASA.

One of the projects that is using WORF facility is the SERVIR (ISS SERVIR Environmental Research and Visualization System). Using a compact telescope and a COTS (commercially off the shelf) digital camera, 3 images per second that cover approximately a 19 km x 11 km area each are automatically captured. The objective is to improve automatic image capturing and data transfer and also using the captured images for environmental science purposes[11].

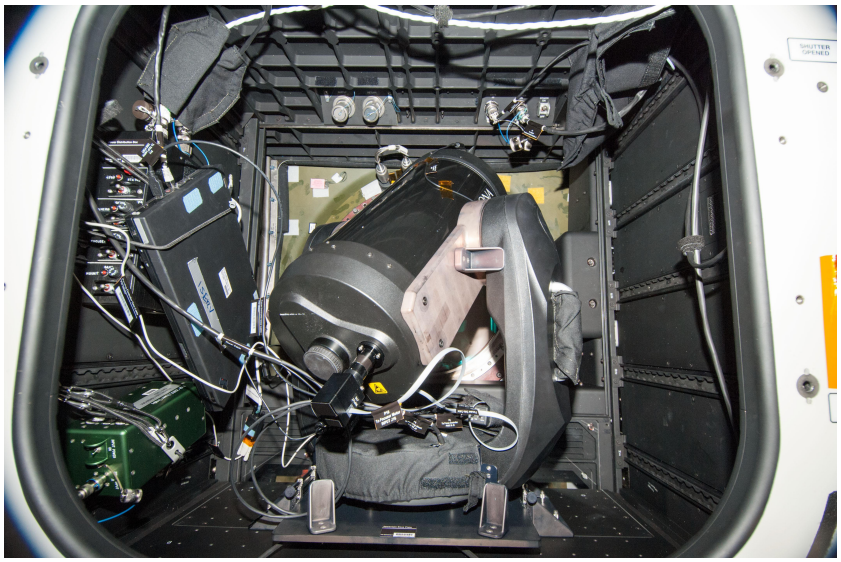

FIGURE 2.19: SERVIR hardware including a 23.5 cm Celestron telescope installed in the WORF. Credit: NASA.

As it can track a point on Earth, we can consider using it for quantum communication purposes. The telescope's range of motion is restricted to $\pm$ 30 degrees from nominal in the altitude and azimuth axes.

[11] http://www.nasa.gov/mission_pages/station/research/experiments/867.html

Chapter 3

Quantum communication with the ISS

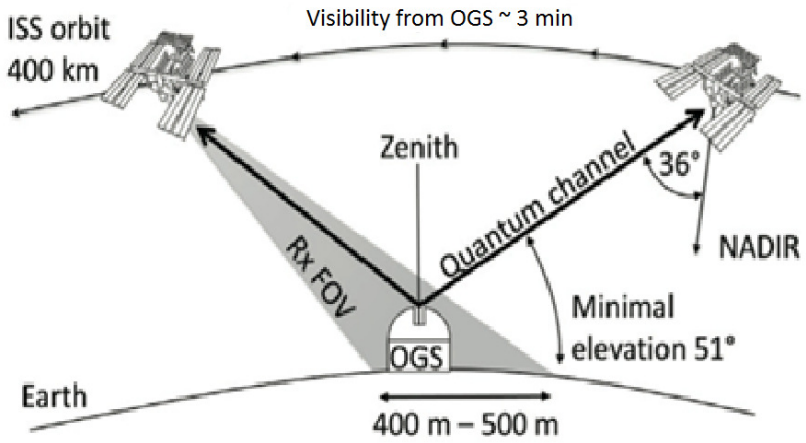

FIGURE 3.1: The orbital pass of the ISS over an optical ground station [19]. The OGS should not be more than 36° off the NADIR direction [1](maximum 3 minutes visibility if the ISS orbit crosses OGS' zenith).

Over the past decade, several free space experiments have been performed through the atmosphere such as a distribution of polarization entangled photon pairs [23] and faint laser pulse decoy states through the atmosphere for an experimental implementation of BB84 QKD protocol [20], where both used a 144 km free space horizontal link between the Canary Islands of La Palma and Tenerife. A free space teleportation has also been demonstrated over a 143 km link [15]. Beside the free space experiments, also fiber based experiments have been done such as a High rate, long-distance quantum key distribution over 250 km of ultra low loss fibers inside a laboratory [21]. By testing the effect of gravitation, atmosphere, motion of the satellite on polarization qubits [4], etc. on quantum theory phenomena like entanglement in ground-space links, we can eventually establish a worldwide quantum communication network in space.
As an attempt for quantum communication[19], we can setup a link between an arbitrary optical ground station (OGS) and ISS using a fairly strong beacon (safety

[1]integration time $\leq 70s$

of the aviation and astronauts is considered) such as a powerful street light. The ISS rounds the earth with an orbit of ca. 93 minutes and in a certain latitude can limited by the diameter of the Cupola's center glass window, we would maximally have 7 minutes (when ISS orbit crosses zenith) until the ISS is out of field of view of the OGS (less than $10°$ above the horizon). But with the proper minimum elevation of $51°$, we would have half of the maximum visible access. The mean measurement time would be 70 seconds in e.g. two transits.
Naturally the OGS would be in an isolated place from light pollution as possible. Then the SNR should be at least 20 which is acceptable for our link. A laser line filter with a narrow band width of 10 nm accompanying a polarizer film cab be inserted into Nikkor lens to get a polarization contrast of 1:200 for e.g. H polarized photons.

Duration	6':25"		
Fri, May 06, 2016 6:35:56 AM WEST	Begin	Max	End
Time	6:35:56 AM	6:38:42 AM	6:41:56 AM
Direction	SW	WSW	NE
Altitude	10°	89°	10°

TABLE 3.1: ISS visibility from Tenerife. One visible pass in one day.

Duration	3':25"		
Sun, May 08, 2016 4:55:34 AM WEST	Begin	Max	End
Time	4:55:34 AM	4:55:34 AM	4:55:48 AM
Direction	SE	SE	E
Altitude	10°	16°	10°
Duration	5':35"		
Sun, May 08, 2016 6:28:12 AM WEST	Begin	Max	End
Time	6:27:21 AM	6:30:06 AM	6:32:56 AM
Direction	W	NW	NNE
Altitude	10°	28°	10°

TABLE 3.2: ISS visibility from Tenerife. Two visible passes in one day.[2]

As seen in table 3.1 and 3.2, some days we might have 2 pass by, some days one and even some days we might have no visible passes.
In table 3.1 one sees that the ISS passes over the zenith and for 6':25" is $10°$ above horizon and almost 3':10" would be in $51°$ above horizon. On the other hand, none of the 2 passes of ISS could be use in table 3.2, because the elevation is not high enough throughout the transition.
Therefore for long duration of visibility, only one pass is possible. But in case of two passes in one day, the altitude would be less than $51°$. So it's the best if we have a near zenith pass.

[2] http://iss.astroviewer.net/observation.php

A proposal

For uplink experiments [19], there should be two segment: A ground segment and a space segment (see figure 3.2). One pair of entangled photons are produced in the optical ground station. One of the photons of the entangled pair is sent to the ISS and the other is measured locally. Because of different source of loss such as losses on optical element surfaces, fiber coupling and detection efficiency, from e.g. 20 Mcps down converted pairs, ca. 5 Mcps could be detected at the source. A faint laser pulse source decoy state typically works at a ferequency of 100 MHz and emits a mean number of photons per pulse up to 1 ($\mu = 1$). practically 40 Mcps are expected, considering an efficiency of 50 % for the detectors.
The coupled out photons of either source are sent to a motorized transmitting telescope using a tip tilt mirror. The time tagging moduls will store the timing information of the local events. The local events in case of EPS are the detection times of the photons measured locally and in case of FPS, are the laser trigger signals.

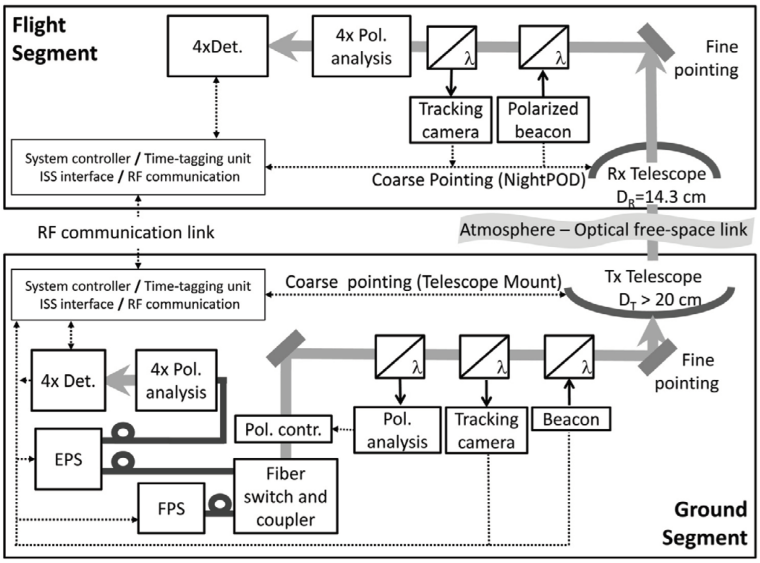

FIGURE 3.2: Diagram of the space segment, the ground segment and the free space in between. Figure from [19].

A 40 dB attenuation in the free space link is expected for the ISS being in a n altitude of 400 km and at zenith. Figure 3.3 presents the attenuation factor as a function of transmitter aperture (ground telescope).
The photons which are reached to the ISS will go through the Cupola window and focused via a photographic lens (Nikon 400mm f/2.8 AF-I). The motorized NightPod mount with track the beam and prevent it to go out of field of view of the lens. A radio frequency communication link can be used to transmit the time tagging unit and detector-channel information which should already be stored in a local storage device.

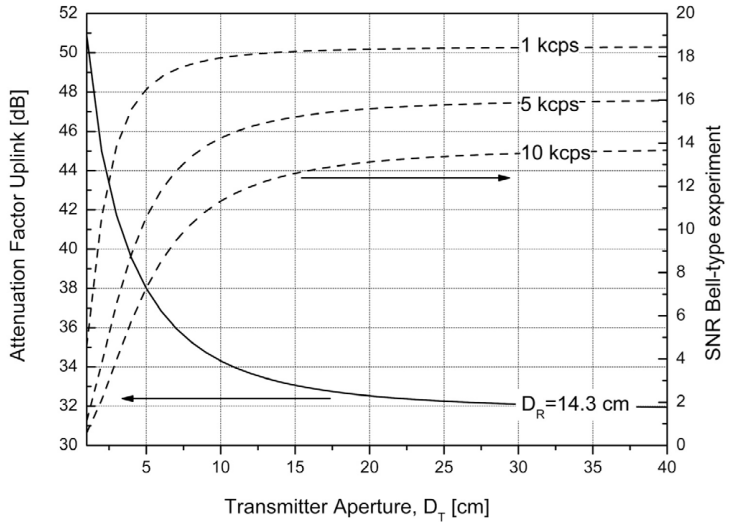

FIGURE 3.3: Solid line: Attenuation of the uplink vs the transmitter aperture for a receiving aperture of 14.3 cm. Dashed lines: expected SNR in a Bell-type experiment is shown for three different background levels. Figure from [19].

Considering 40 dB loss, 500 cps of detected entangled photon pairs for Bell experiment are expected. For QKD using FPS decoy state source, 4 kcps are expected to be detected at the ISS. A minimum SNR of $2/(\sqrt{2}-1) \approx 4.83$ for Bell experiment and a QBER below 11% ($\widehat{=} SNR > 9$) for QKD experiment is required. The following graph shows the SNR of the Bell test and the QKD experiment as a function of attenuation factor of the free space link for different background counts in the detectors located in the ISS.

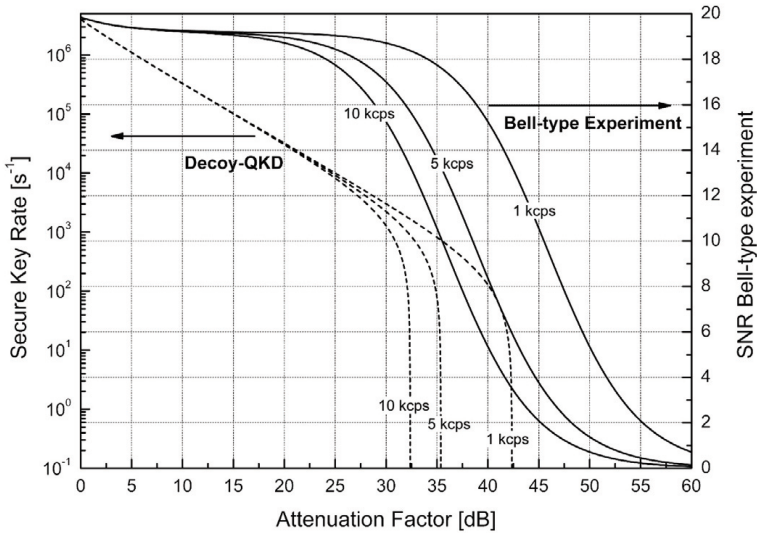

FIGURE 3.4: Solid lines: Obtainable SNR in a Bell experiment as a function of the attenuation factor for different background levels. Dashed lines: Expected secure key rate in an faint laser palse source decoy-state protocol. Figure from [19].

The first step is to perform the experiment using only the center window of the ISS. The next step could be using the side windows of the Cupola and extending the link distance from 400 km to 1800 km.
The camera can be implemented to the setup using an adaptive ring:

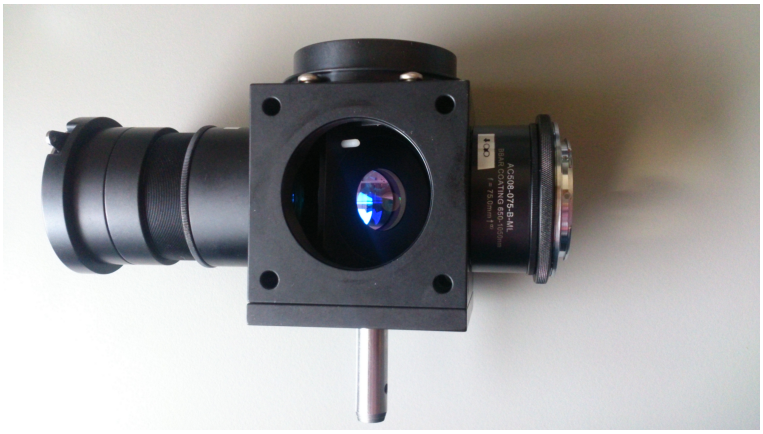

FIGURE 3.5: Connecting the camera to the Nikon lens ($f = 400mm$) and receiving module with a dichroic mirror inside.

In order to perform an uplink experiment with the ISS, we need more precise an reliable data regarding the ISS stability and the precision of NightPod's tracking system (some of previous data are presented in section 2.3.1) or the maximum duration dynamic tracking by the NightPod.
We would have the following objectives:

1. The accuracy of the beam tracking by the NightPod.
2. Influence of the windows on the image quality by using different optics.
3. Influence of the scratch pane and decide whether it shall be removed during the actual experiment or not.
4. Transmission decrement in Cupola window due to scratches.
5. Evaluation of background counts (noise) expected after narrow-band spectral filtering.
6. Influence of Cupola window on the polarization of the photons (considering the existence of pressure only on one side).

For first four objectives and checking for the noise due to the ambient light pollution around the OGS, the instruments already on board the ISS such as the NightPod, Nikon D3s camera and Nikon 400 mm AF-I are enough.
For the last two objectives, we need to prepare and send more parts to the ISS.

Chapter 4

Receiver Lens

4.1 Nikon 400mm f/2.8 AF-I

For narrow angle of view photography of objects far away, one should use large focal length lenses as Nikkor 400mm. The following equation shows how focal length and angle of view are connected:

$$AOV^{\circ} = 2 \cdot arctan(\frac{h}{2f}) \tag{4.1}$$

Where f is the focal length of the lens and h is the horizontal dimension of the sensor which is 36 mm in case of D3s camera, so one would get 5.15° for angle of view. For diagonal and vertical angle of view, h should be respectively replaced by diagonal and vertical dimensions of the sensor.
Therefore having a lens with greater focal length would result to narrower field of view and having picture of remote objects with high resolution. The same kind of lenses are being used by astronauts in the ISS to capture images from earth with fairly high resolution.

FIGURE 4.1: Japanese Aerospace Exploration Agency (JAXA) astronaut Koichi Wakata in front of a window in JEM (aka Kibo) using Nikon D2xs and Nikkor 400mm f/2.8 AF-I. Credit:ISS020-E-021689

Nikon 400mm (f/2.8 AF-I) lens has an aperture with a diameter of 14.7 cm with stops ($f-$ number) down to f/22 with maximum aperture of and has 10 optical elements in 7 groups[1]. Its minimum focus distance is 3 meters and It weights 6.3 Kilograms.
Here's a picture of New York taken from ISS with the same lens currently on board the ISS:

FIGURE 4.2: New York City from the ISS (Nikon D3S @ 400mm, 1/30 s, f/2.8, ISO 51200). Credit: ISS035-E-8051

4.2 Visibility Measurement

To measure the visibility, two polarizers with an extinction ratio better that 10000:1 were used. By setting the first polarizer on H, V, A and D basis and rotationg the second polarizer and subsequently measuring the intensity of the beam coming out of the Nikon lens and using 4.2 formula, the results for the visibility achieved which are shown in figure 4.3. The following formula was used to calculate the visibility:

$$V = \frac{I_{max} - I_{min}}{I_{max} + I_{min}} \tag{4.2}$$

Where V is visibility and I is the intensity of the beam after the second polarizer. According to latter formula, if the minimum intensity after the second polarizer is zero (in case of ideal polarizer and no dark count of the power meter), the visibility would Be 100 % which means that when to bases of to polarizers are perpendicular to each other, there would be no photons reaching the power meter which in turn means the the lens does not add any rotation to the polarization of the photons going through it.

[1] http://www.kenrockwell.com/nikon/40028afi.htm

The visibility measurement of the lens was performed with a 810 nm laser and 730 μW power for Horizontal, vertical, Diagonal and anti-diagonal polarization. The achieved result for the visibility was greater than 99.5%. The setup is depicted in figure 4.5. By knowing the visibility of the lens we can measure the polarization dependent attenuation of the window of the ISS and also the effect on the QBER as it depends on the visibility (see section 1.2.2).

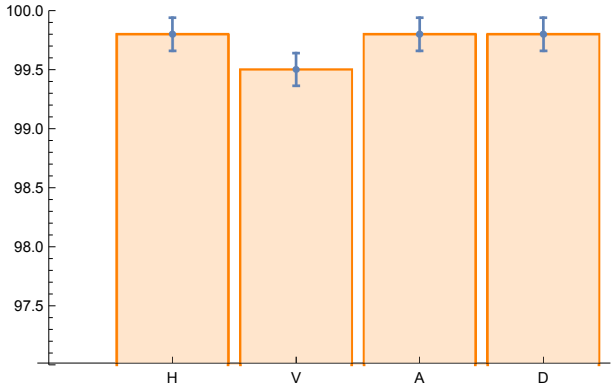

FIGURE 4.3: Visibility diagram of the lens (%).

The error bars correspond to uncertainty in power meter value and variation in laser power and also the extinction ratio of the polarizers (10000:1).

4.3 Transmission measurement

The transmission of the commercial lenses are maximized for the visible spectrum. The manufacture minimize the spherical and chromatic aberrations and correct the astigmatism by using several optical elements in different groups and positions. The laser beam was collimated with a 14 cm lens and sent into the lens. By slightly changing the collimator lens, the beam was focused and the power was measured.
Then again by moving the lens back to the position where the beam gets collimated, the Nikon lens focused the beam on a power meter. A polarizer was used to set the polarization on H, V, A and D. By subtracting the power before and after the lens, the transmission for 810 nm and for each polarization was achieved which is shown in figure 4.4.
To check the collimation, we can manually put the focus on infinity which means the lens focuses an incident beam that is coming from infinity and is collimated on the focal plane of the camera. This distance is $\sim$ 5 cm after the Nikon lens. It is a standard length for all the Nikon f-mounts so one can use different cameras with different lenses.
Throughout the experiment, the f-number was set on f/2.8 which is the wide open aperture[2]. The angle of incident was 0° (perpendicular).

[2]The f number (indicated by N), is the ratio of the focal length of the lens to the diameter of the entrance pupil (effective aperture). $N = \frac{f}{D}$

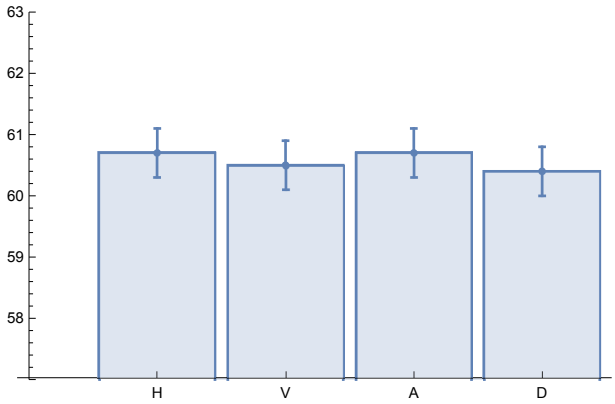

FIGURE 4.4: Transmission of the lens (%).

The error bars correspond to uncertainty in power meter value and variation in laser power and also the extinction ratio of the polarizers (10000:1). Having the transmission results for different polarizations, we can investigate the transmission of the link. The transmission was measure for an incoming collimated beam that covered the whole aperture of the lens (14.5 cm). Considering the dust and the absorption of photons by optical elements and reflection of the photons from the lens" surface and even clipping a small portion of the Gaussian beam's tail, 60 % transmission was achieved.

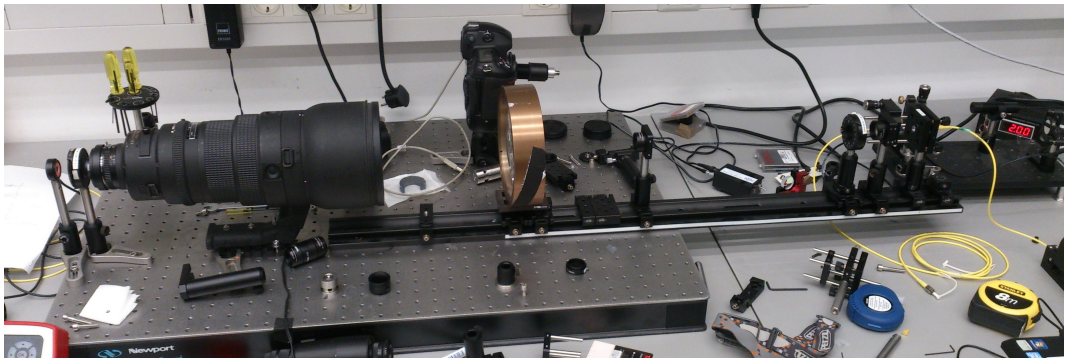

FIGURE 4.5: Visibility and Transmission measurement setup.

Naturally less transmission is expected compared to a collimated laser beam with a diameter of a few millimeters. For a laser beam with a diameter of $\sim 2\,\text{mm}$, the transmission was 75% (± 3). This 15 % difference was a bit more than expected change in the transmission. It is noteworthy to mention that the 52 mm neutral color filter of the Nikon lens has a transmission of 96% for 810 nm light, so without this filter we can increase the transmission by 4% (± 1). We can remove this Neutral color filter and either leave the filter holder empty or replace it with another desired filter.

Instead of this NC filter, we can use a bandpass filter for the certain wavelength we want to send through. Therefore we can cut out the noise and increase the signal to noise ratio.

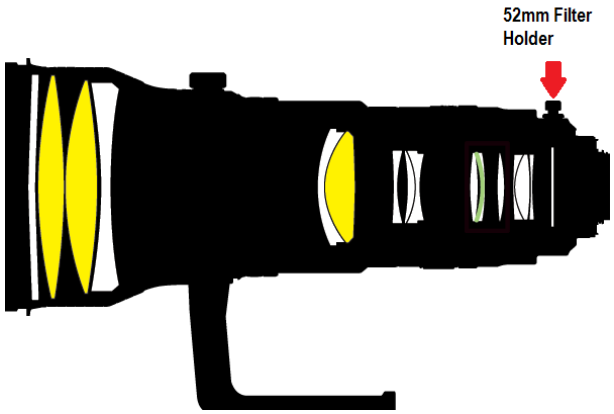

FIGURE 4.6: Diagram of Nikon lens and the potition of filter holder.

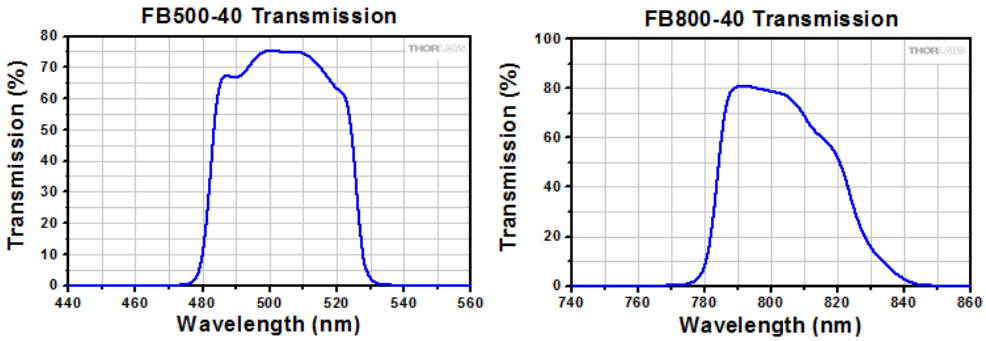

FIGURE 4.7: Bandpass filters samples from Thorlabs for 500 nm (left) and 800 nm (right).

In figure 4.7, the transmission of two 1" band pass filters from Thorlabs are showed. We can use a similar filter but 52 mm in diameter for the Nikon lens.

Chapter 5

Nikon D3s

To get the approval to send an object to the ISS, a rather long procedure is needed which consumes valuable time and also requires expenses. We can use the privilege of having the Nikon D3s on board the ISS to perform preparatory experiments and also use it potentially for tracking purposes. There are different cameras used in the ISS for photography and most of them are Nikon cameras such as: D1, D2Xs, D200, D3, D3s, D3X, D4 and D800E (seems like astronauts are Nikon photographers!). In order to use the existing D3s cameras on board the ISS, we have to characterize the camera. We can use the privilege of having these cameras on board and use them for scientific projects such as quantum communication. These cameras could be used in a setup as a detector, tracker, power meter, etc. First the Nikon D3s with the IR filter was used for characterization and the the IR filter in front of the CMOS was removed so the sensor could detect also in IR region.
A 532 nm laser was used to create specific number of photon. The laser was coupled into a single mode fiber and was focused by a focus tunable lens and sent to the camera. As the surrounding light was suppressed, by taking a dark image (with cap and pathfinder closed) one could subtract the noise from the incoming laser (signal).

5.1 How DSLR cameras acquire images

Digital SLR cameras use a CCD (Charged Coupling Devices) or CMOS (Complimentary Metal Oxide Semiconductor) sensor instead of photography films in traditional SLRs. First digital cameras used CDD as a sensor but because of the special production process and the cost of the production, CMOS became the favorite sensor and is mostly used used in recent cameras whereas CCDs are used in a few recent DSLRs. Unlike CCD, CMOS reads out each pixel individually. Some of Advantages of CCDs are low noise, high full-well capacity, high uniformity and some of disadvantages are slow readout, pixel blooming, special fabrication. As for the CMOS, there are some advantages like high speed readout, random access, low power consumption, lower price compared to CCDs and some disadvantages like high readout noise, reduce dynamic range and reduced uniformity.
In case of Nikon D3s, there's a Bayer color filter array on the top of pixels and consists of two green filters, a red and a blue one. On the top of each filter, there's a micro lens which focuses the light into the pixel pitch. A larger pixel pitch means that more photons would be collected for one pixel which leads to a sharper image. commercial cameras usually mention only the resolution which is the number of pixels. But the pixel size is as important as that.
The photons are showered into each pixel and produce electron-hole pairs in the semiconductor. The produced photoelectrons are gathered by the circuits and go

to Analogue to digital converter (ADC) which will turn into digital numbers as binaries. Figure 5.1 shows how photons turn into pixel values in digital cameras.

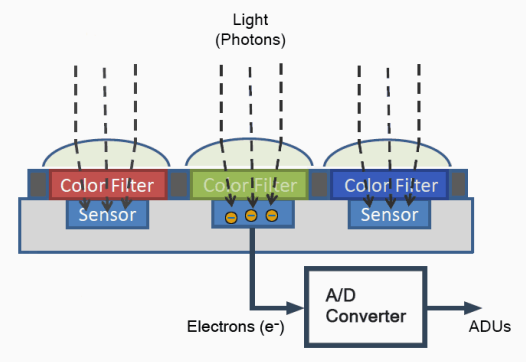

FIGURE 5.1: Simple sketch showing how DSLR camera sensor converts the light into pixels values.[1]

The photo-electrons get amplified for the read out and go for further processing such as compression, noise reduction, etc. which in case of raw image is not the case and the read out after the amplification is the value for each pixel. ISO (aka "film speed") in DSLR cameras is the gain amplification done on the pixel read outs. More gain means more sensitivity and more noise of course. At an unofficially defined "ISO at unity gain", The ADC assigns 1 electron to 1 digital unit. The raw Image produced by the sensor is just a grayscale image which gives the intensity of the incoming photons in each pixel. By knowing the position of each color of the color filter array, the camera can assign a color to each pixel. Because each pixel has a specific color filter, it cannot have any information about the other two color. Also the color assign to a pixel, might not be a correct one. For instance, photons from a 10 millimeter red disc can penetrate through not only the red pixels, but also the green and blue pixels. The intensity of a red pixel exposed to a red photon is much more that the green and blue pixels. Now we would have an image with different color mosaics. To get a smooth image, digital cameras use various demosaicing algorithms to interpolate values of red, green and blue for each pixel. These algorithms use the pixel value of each pixel and its the neighboring pixels to calculate the corresponding color for each pixel. These algorithms can produce various formats like TIFF, PNG, etc. or some more compressed formats like JPG.
For the experimental purposes, we don't need any demosaicing or compressing, so we use raw image to extract the data. It can be a bit challenging as the size of the file is respectively large (24 MB for a 14-bit raw image). If we want to transfer the files from the camera to a device, we need a faster terminal. For the measurements, the raw files with Nikon Electronic Format (NEF) were used. It contains all the data data available from the camera. Since the sensor is a linear device (in opposite to traditional photography films), the NEF file is a linear image. Linear in a sense that when the green pixel get exposed with photons with n-times as intensity as photons hitting the red pixel and the blue pixel get exposed with photons with n-times as intensity as photons hitting the green pixel, the ratio of the pixel value of $blue/green$ is equal to the ratio of the pixel value of $green/red$. The raw image is not usually readable by computer software.

[1] http://www.odelama.com/photo/A-Simple-DSLR-Camera-Sensor-Noise-Model/

A program called *dcraw* was run by *Mathematica* as an external command-line program to convert the raw file to a linear unprocessed TIFF file so the program software could read it for analysing purposes[2].
To analyse the data, a portion of the whole image were cut out about where the laser point hits. Then e.g. for green laser, the green pixels give much larger pixel values and therefore we can find out which pixels have green filter on them. The color filter array on the D3s is a Bayer filter array which is a RGBG pattern as below:

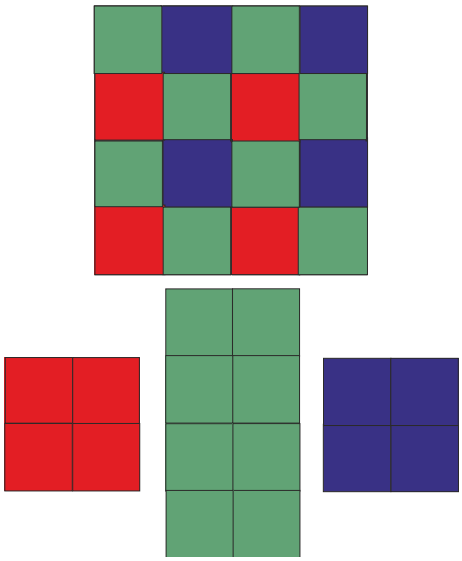

FIGURE 5.2: Bayer color filter pattern. Top: The whole color filter array. Bottom : Red, Green and Blue filters separated.

Each pixel with a certain color filter was selected and the pixel value of it was extracted to check for a certain number of photons, how pixel value would be assigned by the ADC of the camera.
The laser was coupled into a single mode fiber and focused into the sensor as the TEM_{00} mode. The laser point on the sensor was uniformly spread so the statistical distribution of photons on the pixels was the same for each of RGB color filters. As a Gaussian beam has the most intensity around the propagation axis, we can interpret that we have more photon in that area and the number of the photons decay according to the Gaussian distribution of intensity as the radius increases (eq. 1.26).
The Bayer filter is the most common color filter used by DSLR cameras, but there are various other alternative color filter arrays which have different ordering of the colors of even different color filters such as kodak's RGWB color filter array of Fujifilm's EXR color filter array.

[2]Software packages are getting compatible with raw files. For instance *Mathematica* version 10.1 and above, has the ability to read and analyse raw files.

Here's a graphic of the Gaussian profile of the green laser which is spread over about 40×40 RGB pixels for ISO 6400 and 1/400 s exposure time with the IR filter on (a Gaussian function is fitted to the discrete distribution of pixel values at different positions on the sensor):

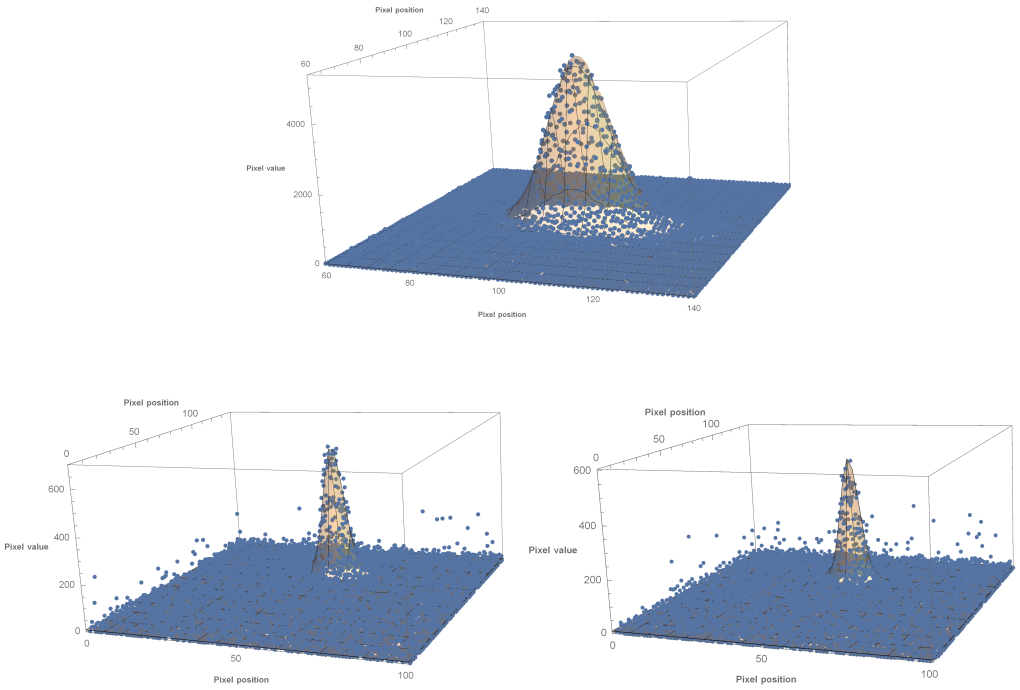

FIGURE 5.3: The Gaussian fitted profile of the green laser. Top: Green, bottom from left: red and blue color filtered pixels.

In last two plots of figure 5.3, the noise starts to become significant as the signal (and consequently pixel values) is reduced. As a green light is sent into the camera, the transmission of green photons in blue and red filters are much lower compared to green filter. The standard error for the fit in X and Y direction was better that 0.1 %.
About 3000 images were acquired and analyzed to get the precise and reliable results. Each acquisition with different setting was checked for the saturation and homogeneity of the beam. If the beam saturates the pixel, it means that the pixel value per photon would be less than the actual value.
There's a feature on most of DSLR cameras called noise reduction. It automatically takes one dark image in addition after the image is taken by the photographer and electronically subtract the noise (which is measured from the dark image) from the original image. The noise reduction was OFF through out the whole characterization to avoid any unknown and unnecessary electronic and digital processes on the image. Instead a similar process was done manually by taking a dark image with the same setting and subtracting the pixel value of two images.

5.2 Measurements with the IR filter on

5.2.1 Dark Counts

Dark count are usually the main source of noise. In the absence of photon source, i.e. when the camera is light-isolated, the should be not pixel value registered by the camera. In reality even single photon counting modules have intrinsic dark count. By knowing the intrinsic dark count of the camera, we can measure the noise due to the light polution around the ground station. As the sensor temperature is far from absolute zero, we have thermal excitation of the electrons. When the camera is exposed to high intensity light, dark counts effect is not considerable. But in low light shooting, and also in high ISO setting (usually extended ISO), the become more noticeable.
Here are some selected graphs of dark counts (whole sensor) vs exposure time in different sets of ISO. It is indicative that there's only small deviation in dark counts distribution.

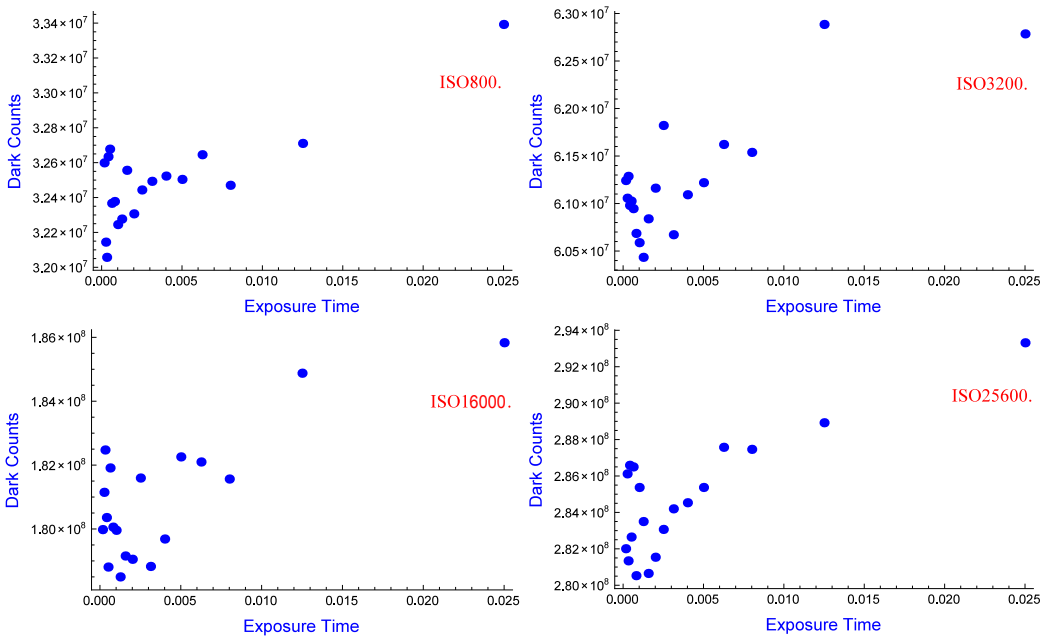

FIGURE 5.4: Dark Counts vs Exposure Time (s) for different ISO settings

The mentioned *dark counts* are actually the pixel values registered by the sensor that we cannot change. The error bars corresponding to the Poissonian error are within the size of the points. The complete set of measurements can be found in appendix A.
It is evident that the number of dark counts are fluctuating for short exposure times. But by increasing the exposure time, the dark counts increase. For instance with ISO 25600, we would get 24 dark counts per pixel in 1/40 seconds. The fluctuation of dark count in short exposure times are more due to the electronics that the ambient photons reaching into the sensor. Then from a hundredth of a second, the fast fluctuations decay.

The figure 5.5 shows dark counts plotted versus the ISO in selected different exposure times. Regardless of some small jumps, they all have a linear trend. The linearity of the CMOS sensor is evident.

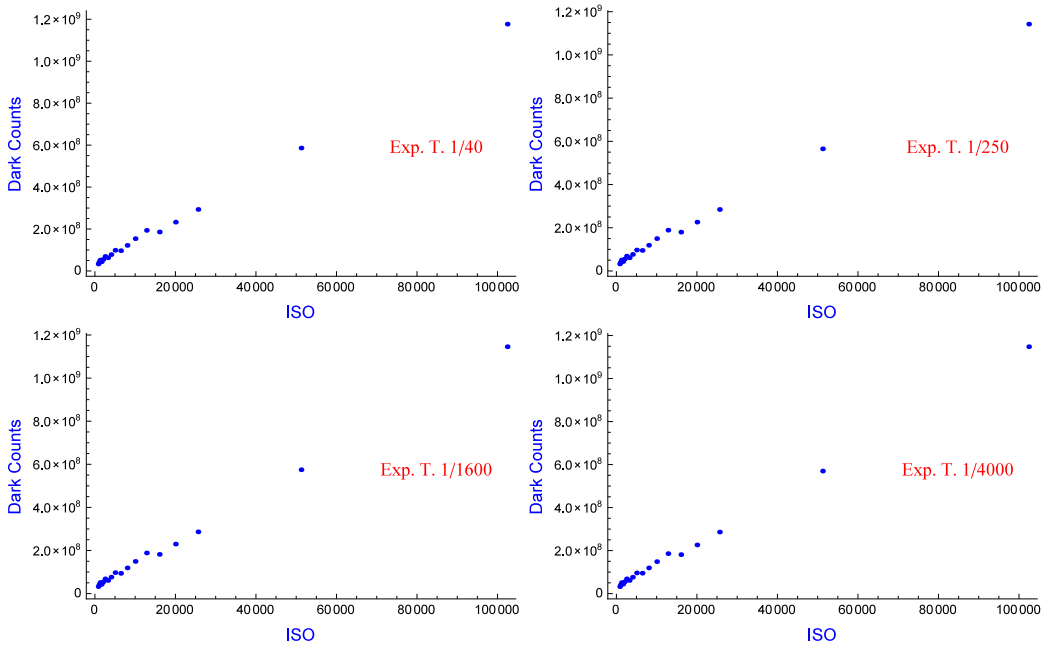

FIGURE 5.5: Dark Counts vs ISO for different Exposure Times (s)

The error bars corresponding to the Poissonian error are within the size of the points. All the graphs for exposure times from 1/40 s to 1/4000 s look the same (see Appendix A for complete set of graphs), but there a slight change in the dark counts. In fact the standard deviation to Mean value ratio for the dark counts of the same ISO setting and different mentioned exposure times varies form 0.007 to 0.011. The jump from ISO 12800 to 16000 appears because the "native" ISO of D3s is between 200-12800 and digital in "boost" mode up to 102400.
The sensor of digital cameras has an unboosted ISO range in which the camera changes the ISO only the gain to amplify the input signal (output=input×gain). One ISO in this range is the base ISO, e.g. 200. In this ISO the gain would be 1, so there's no amplification is performed on the signal. This is because the number of photoelectrons which the sensor produces are equal to the number of electrons needed for the intensity we should get for that certain ISO. The base ISO is an intrinsic property of the material, usually silicon, which the sensor is made of (Quantum efficiency). The amplification of the output is done not only for the incident photons but also for the dark counts as the sensor cannot differentiate the actual signal from the noise. Therefore we see an increase in the noise as the ISO is increase.
In addition to gain amplification, digital cameras offer an extended range of ISO (boosted) settings which are done by post processing in the camera. The sensor would use the highest ISO (as in the highest ISO in Native ISO) and digitally post-process the image to get to the given ISO setting.

5.2.2 Measurements for green laser

The D3s camera could be potentially used for tracking purposes or a single photon counter. For this matter we should characterize the camera for a green beam as the tracking beacon would be green which is most transparent for the Nikon lens and the camera sensor has the highest response to this wavelength. The astronaut can take a picture and feed it to the tracking system. As the CMOS sensor gives use access to each pixel value, we can use green channel of the sensor for tracking. The threshold of having saturated pixels in different exposure time and ISO is depicted in figure 5.6. Any settings below the line, leads to saturation of the pixels in the peak of the Gaussian profile with 0.07 nW power and 532 nm wavelength (the beam is focused on the sensor with a diameter of 40 pixels). Maximum value for the pixels of D3s before saturation is ca. 16000.

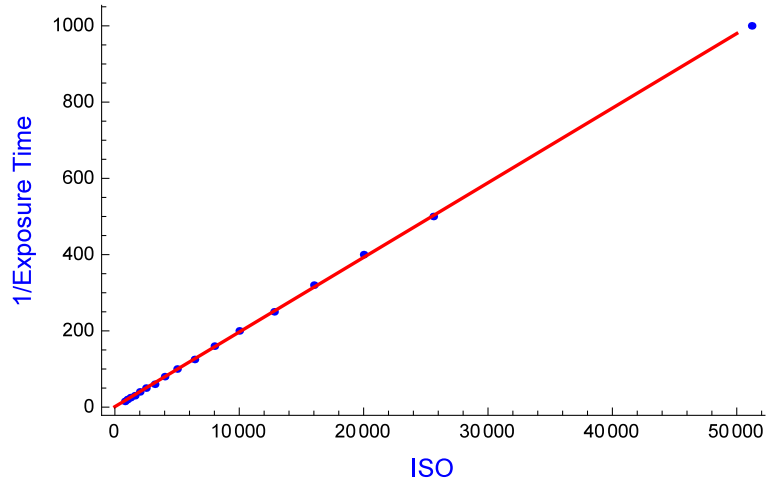

FIGURE 5.6: Saturation threshold for same power (0.07 nW) in form of 1/Exposure time (1/s) vs ISO (linear fit with slope of 0.0196 and y-intercept of 2.5826)

Each point indicates one exposure time and ISO setting from discrete range of setting options. The pixel value per photon for each of red, blue and green color filtered pixel was measured, then we would know by sending a finite number of photons into the sensor, how much pixel value we would get. In other words, if we have a pixel value per photon (PVPP) of 4 for a certain ISO and exposure time, by sending 100 photons in a pixel, we should get a pixel value of 400 for that pixel. The quantum efficiency of Nikon D3s is about 57 % [3]. In turn, the quantum efficiency (QE) is related to photon detection efficiency (PDE) as following:

$$PDE = QE(\lambda, V) \cdot \varepsilon(V) \cdot GE \tag{5.1}$$

Where ε is the Geiger efficiency, GE is the geometric efficiency, λ and V are respectively the wavelength of the incident light and the bias voltage. Geometric efficiency is related to the engineer construction of the sensor. How big the pixel pitch is or the space the electronics around pixels occupy or even the light is reflected to deflected by micro lenses on top of the sensor, can play a role in geometric efficiency.

[3] http://www.sensorgen.info/

Here is the pixel value per photon of green pixels for different ISO settings is depicted:

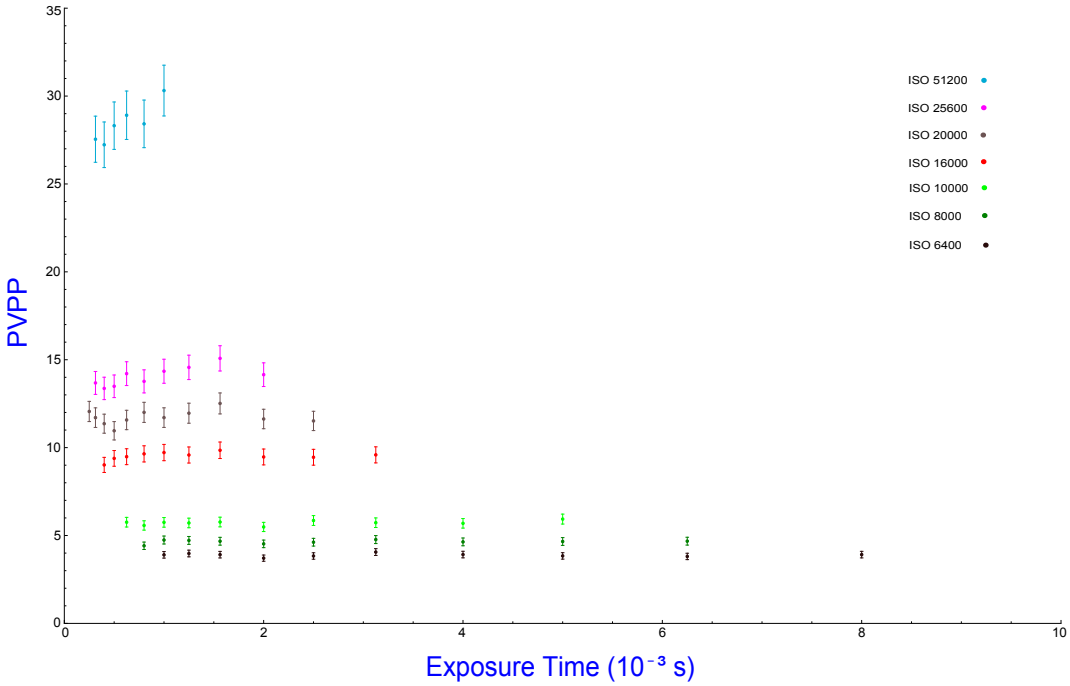

FIGURE 5.7: Pixel value per photon for green pixels with laser beam power of 0.07 nW and wavelength of 532 nm

The error bars correspond to fluctuations in laser's power.

5.3 Measurements after removing the IR filter

As SPDC is commonly used to produce entangled pairs and the wavelength of the down converted photons are 808 nm according to phase matching rule, if a 404 nm pump laser is used. If we want to count the infrared photons with the camera we have to modify the camera for infrared wavelength.
On the top of the sensor, there's a filter which cuts out the wavelengths which are not visible to reduced the noise for visible light photography. As one can see in figure 5.8, To use the camera for infrared purposes, one should remove the IR filter as the transmission for IR is near zero.
After removing the IR filter, the transmission of the filter was measured using LAMBDA 950 UV/Vis/NIR Spectrophotometer and the result is graphed in figure 5.8. As it is evident from the graph, the non-visible spectrum cannot reach the sensor. Without the filter, a broad range of spectrum can reach the CMOS and as the semiconductor used for the sensor is sensitive to this range of wavelength, there would be photoelectrons produced and go to the read out. These photoelectrons would be responsible for a higher noise. As long as we don't need to capture light in non-visible range of spectrum, the best is to use a so-called infrared (IR) filter to get to minimum noise. The transmission for 810 nm is 0.098 % and for 530 nm is 81.38 %.

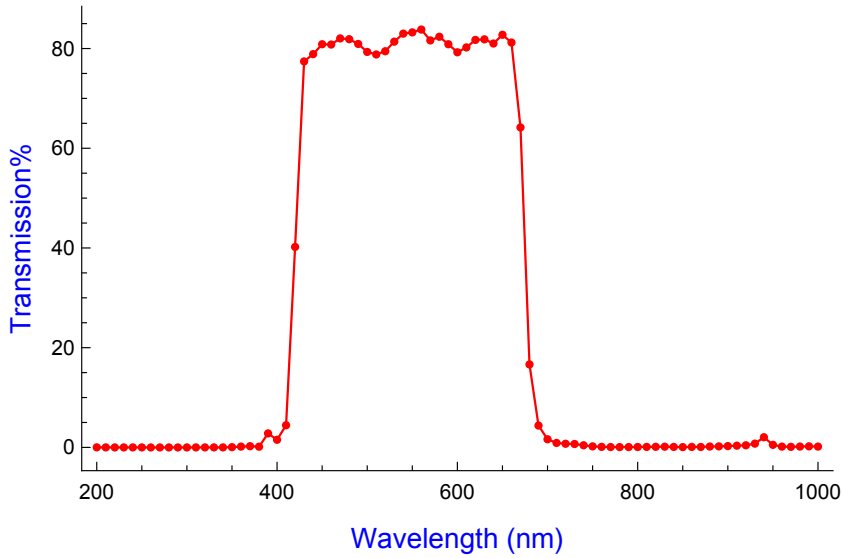

FIGURE 5.8: Transmission of the Nikon D3s infrared filter.

From D3 series, Nikon company used a new sensor (figure 5.10) for the shutter (self-diagnostic shutter monitor circuitry) which allows photographers to capture precise exposure time photos by monitoring how long the shutter stays open. This sensor includes an LED which indicates how long the shutter should stay open. This IR emission from the LED is not emitting through out the exposure as the difference in exposure time does not affect the pixel values. In fact for instance in ISO 10000, the sum of pixel values for the whole sensor is 3×10^9 for exposures of 1/100 s , 10 s, and 30 seconds and stays the same ($\pm$ 1.5%), Sometimes even less for longer exposures. In the absence of IR filter, the emission of the LED leaks into the CMOS and appears like a fog.
The problem is, the CMOS is actually sensitive to this IR wavelength which subsequently prevents IR photographers to use high ISO setting. Some Nikon cameras like D7000 allegedly[4] use a different wavelength for the LED which cannot be detected by the CMOS, so the shutter's function does not interfere with CMOS function.
The fog in dark images (cap and view finder closed and lights off) is distinct in acquisitions with ISO over 2000. As there is no solution to cover the CMOS from exposing to the IR emission of the shutter as the shutter is located on the top of sensor or sealing the IR LED of the shutter, most of the photographers use low ISO settings like 800 and longer exposure times to acquire images form still objects or sceneries. In the following one can see an example of the IR light leaking in the sensor. In the compressed nonlinear form as JPG format, the fog is more distinct as our eyes do not respond to light linearly and digital processes on the raw image, makes it more familiar with our eyes. The fog is brighter but also is more plane compare to dark region on the left side of the image and makes it easier to subtract the noise. In figure 5.9 on the left, the laser point is recognizable as a bright dot.

[4]https://www.lifepixel.com/tutorials/infrared-photography-issues-solutions

Here are two images indicating the IR fog:

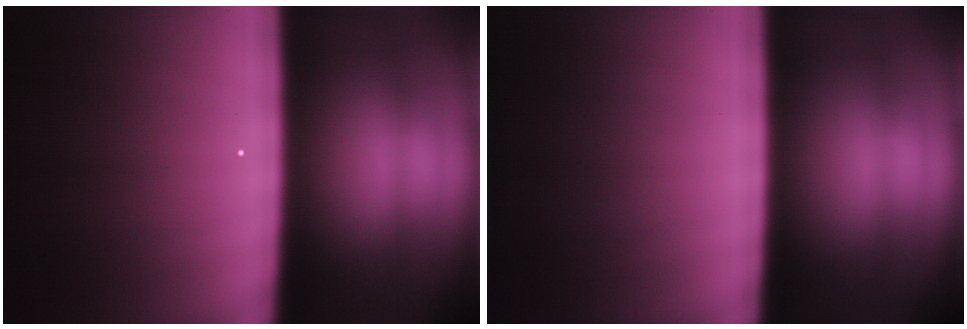

FIGURE 5.9: The fog due to IR emitting LED of the shutter's sensor. Left: laser ON, right: laser OFF (dark image). Images with jpg extension. ISO setting: 16000.

The following figure is the actual shutter of Nikon D3s[5]:

FIGURE 5.10: Nikon D3s shutter unit.

On the right side of the shutter, the LED is located which emits IR light. By using a feedback loop, the camera synchronizes the selected exposure time with the actual time that the shutter is open. The LED emits light only at opening and closure of the shutter. As the leakage occurs from the gap between two sides of the shutter, there's no way to prevent it. However we can use low ISO setting and longer exposures regarding the error budget of the NightPod.
It seems that the only possible way is to have the integration time smaller than the exposure time, i.e. the shutter opens, then after a pause, the sensor starts to collect photons. Then the sensor stops the collection and after that the shutter gets closed. But as simultaneous readout is not possible for CMOS sensors, this idea would not be practical. At least not without modifying the firmware of the camera which is also not risk free.

[5] http://imaging.nikon.com/lineup/microsite/d3s_d3x/en/reliability/

In the following graph, the pixel value per pixel is depicted and it's explicit that the IR fog which is caused by the IR LED of the shutter sensor, leaks into red pixels. The slope of red dots (pixel values corresponding to laser exposure) are 10% steeper than blue dots (pixel values corresponding to no laser exposure).

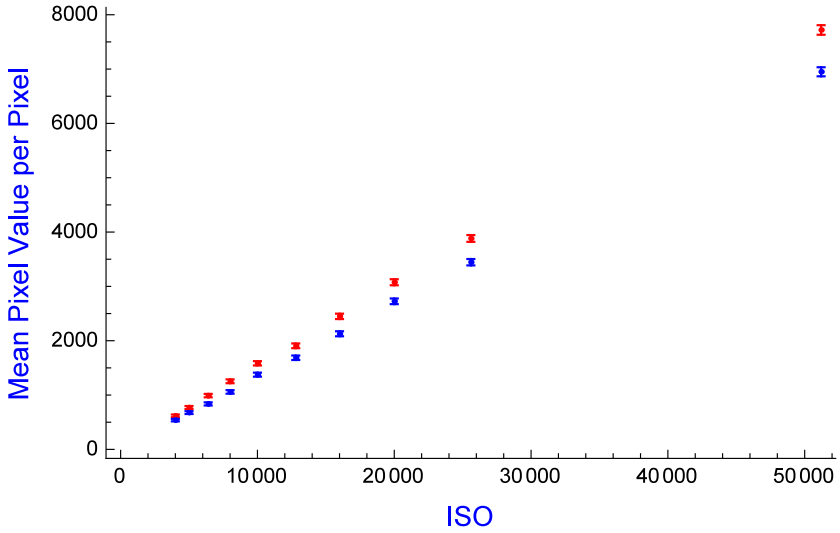

FIGURE 5.11: Pixel value per pixel vs ISO for laser-on (red) and laser-off (blue), exposure time 1/50 s

The error bars are the Poissonian error. As represented above, the signal to noise is lowered dramatically due to the fog caused by the IR leakage from the shutter's sensor. We have an SNR of 1.145 ($\pm$2%) . But the signal from noise is separable by 1 σ separation. Obviously higher ISO setting leads to higher noise but the difference between noise and the signal becomes larger as it is evident in figure 5.11. In the following graph We have the comparison of the IR fog as dark pixel values of two different ISO settings for different exposure times. The error bars corresponding to Poissonian error are within the size of the points.

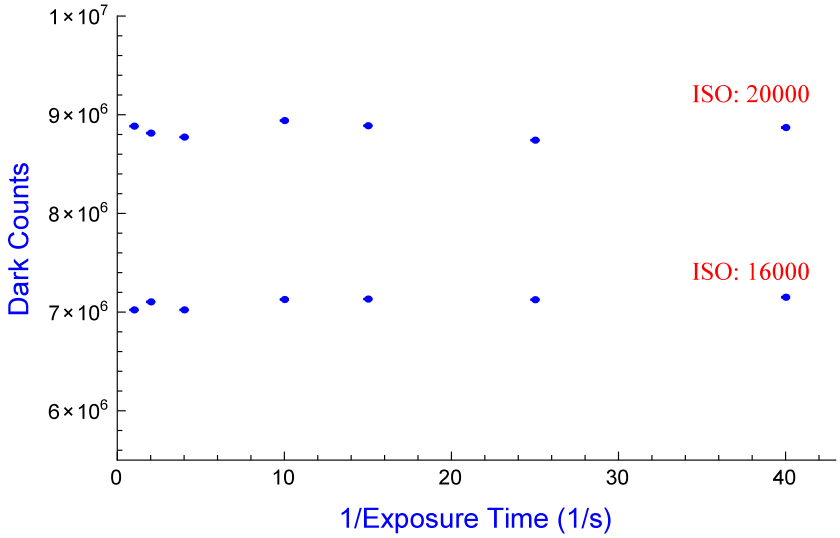

FIGURE 5.12: Cavity extended laser.

A cavity extended laser (see figure 5.13) was used to select the 808 nm wavelength to be coupled to a single mode fiber.

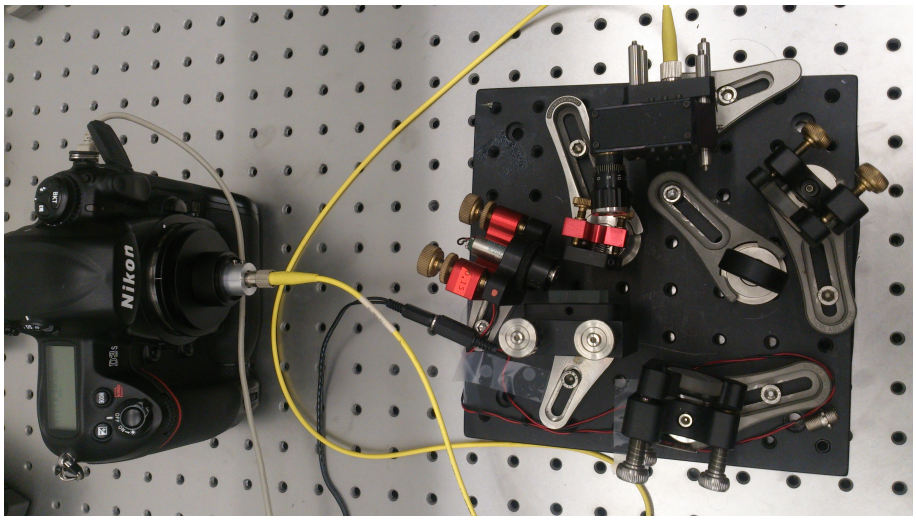

FIGURE 5.13: Cavity extended laser.

The laser setup was placed under a box to be less affected by the temperature change of the immediate area. The wavelength of the laser which was coupled into a single mode fiber was checked using a spectrometer (figure 5.14).

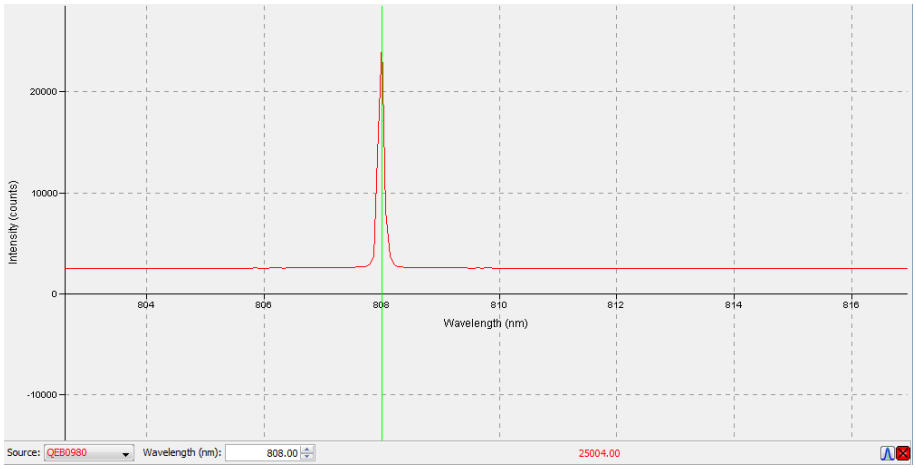

FIGURE 5.14: Spectroscope view of the selected wavelength.

The absorptive filters which were used to reduce the power were characterized. The number of photons sending in was measured using a free space Excelitas as a single photon counter (count rate: 2.8 MHz). Because of the IR leakage, at least 100k∼120k photons are needed to be distinct enough for the camera. That can easily be compensated using exposures in an order of 1 second.

Here are the pixel value per photon for the red pixels and 808 nm laser beam for selected ISO settings:

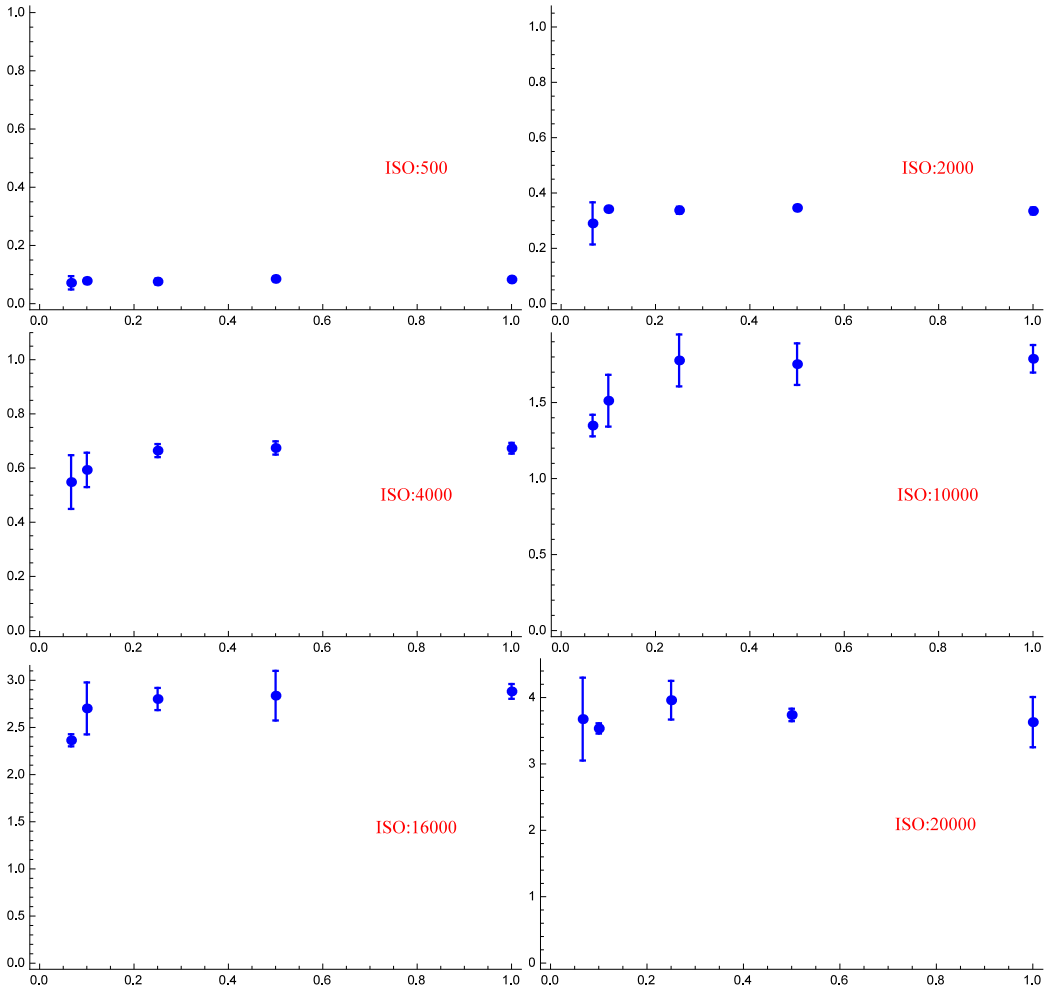

FIGURE 5.15: Pixel value per photon vs exposure time (s).

The error bars correspond to fluctuations in laser's power and statistical error as different pictures was acquired with the same settings. The fluctuation in laser's power plays the dominant role in the errors. The complete set of graphs for different measurement settings are available in Appendix A.
As the exposure time gets smaller and smaller, the fluctuations of the laser's power become evident. It usually appears as a decrease in pixel value per photon indicating that the power of the laser was below the average point when the image was acquired.
Since there's no so called reciprocity failure in DSLR cameras and they are linear (doubling the number of incident photons leads to doubling the output signal), for a given ISO (gain) we should have the same pixel value per photon assuming a constant mean number of incident photons.

One other alternative is to use Live view of the camera. The format of the video is motion JPEG with variable bit rate with one option for the frame rate, set at 24 fps with maximum resolution of 720p.
Here we can see the time averaged pixel value per photon for green pixels and red pixels exposed respectively by a green (532 nm) and infrared (808 nm) laser for each ISO setting.

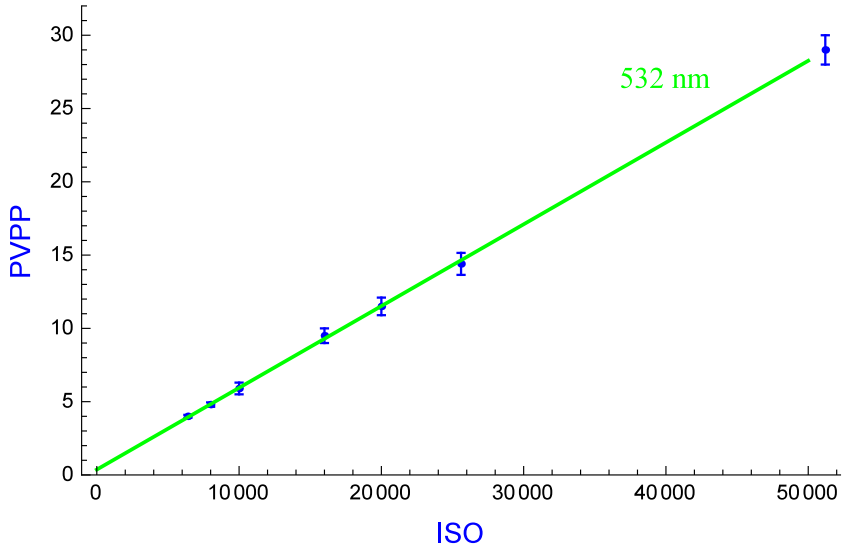

(A) Green pixel exposed by green laser.

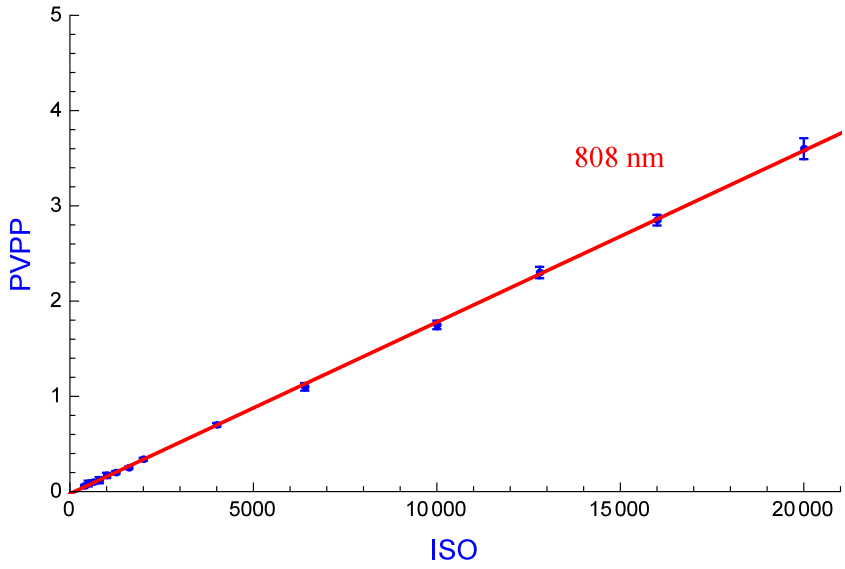

(B) Red pixel exposed by IR laser.

FIGURE 5.16: Averaged PVPP over exposure times vs ISO. A: IR filter on, B: IR filter removed.

The pixel value per photon (PVPP) for 532 nm and green pixels is almost 3.5 times greater than PVPP of 808 nm and red pixels. This could be due to higher quantum efficiency of the CMOS for 532 nm than 808 nm and also higher transmission of green color filters (of CFA) for 532 nm laser compared to transmission of red color filters for 808 nm laser. The error bars indicate the averaged error due to the variation of the laser's power and thus the number of photons for different

images with the same exposure time and ISO setting.
The following graph represents the quantum efficiency of a typical CMOS camera for different wavelengths:

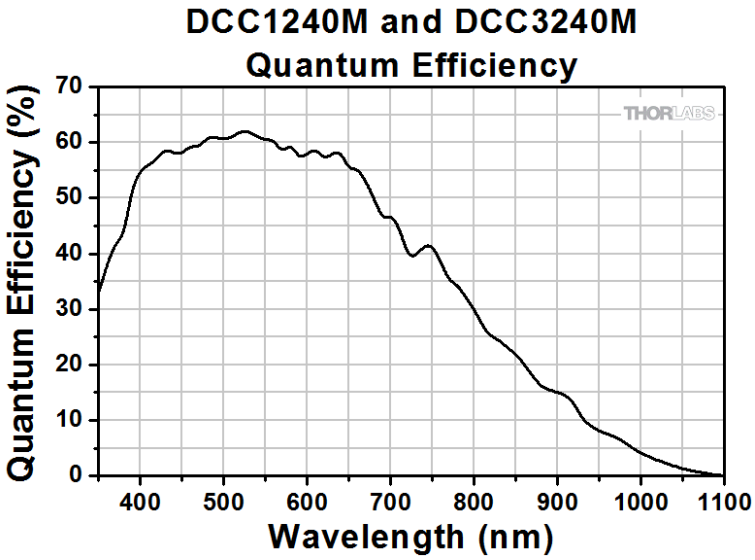

FIGURE 5.17: QE of a USB 3.0 CMOS Camera from Thorlabs.

It's evident that for ca. 530 nm, the QE is the highest and for 808 nm is almost half of QE for 530 nm.
Moreover, the color filters on each pixel have the maximum transmission for visible spectrum, so for red filter, we would have a decrease in transmission after 700 nm. Thus for 808 nm, we would have less transmission in red filter compared to 532 nm and green filter.
As the sensor is sensitive to more wavelengths than only the visible spectrum, all of DSLR cameras originally have a filter (usually known as IR filter) to block the wave length below 400 nm and about 700 nm (see figure 5.8). Having the filter ON, leads to less noise as IR and UV photons cannot reach the sensor.

Chapter 6

Conclusion

Going from terrestrial experiments to extraterrestrial experiments is a big step forward and became a hot topic in the past few years. To make a device space approved, a rather long and expensive procedure is needed. In the meanwhile we can make the best use of the ISS infrastructure and the devices on board the ISS. We can conclude from the outcomes of the measurements that for the tracking purposes, the best is to use the camera with the IR filter on and a green transmitting beacon due to maximum efficiency of the camera's sensor to green light. Also due to the infrared leakage from the implemented IR LED in the shutter, we have lots of background noise. As the shape of the fog is more or less the same for a given ISO value, we can subtract point to point to get the signal. By knowing how pixel values we get for a given amount of incident photons, we can also use the camera as a power meter that is already on board the ISS. For the uplink experiment, we need to use proper avalanche photo diodes to be able to count the single photons reaching the space station. A few thousand down converted infrared photons per second is too faint to be capture by the camera, specially with the mentioned source of noise.
Howerver conducting preparatory experiments to gather more data about the amount of background noise or the probable change in the transmission of the multiple layered window of Cupola due to one pressurized side and scratches and characterizing the accuracy of tracking ability of the NightPod. We can push the limits of the NightPod and check if we can use the side windows of the cupola beside the centered window. We might get less background noise as the side windows situated in a way that they are not faced to the Earth's surface and less light pollution and consequently a higher SNR would be achieved. Moreover there could be more experiments conducted than the ones mentioned before, like constructing a laser communication terminal for classical optical links.

Appendix A

Complete data of measurements

A.1 Dark counts

Here are the Dark counts against exposure time depicted:

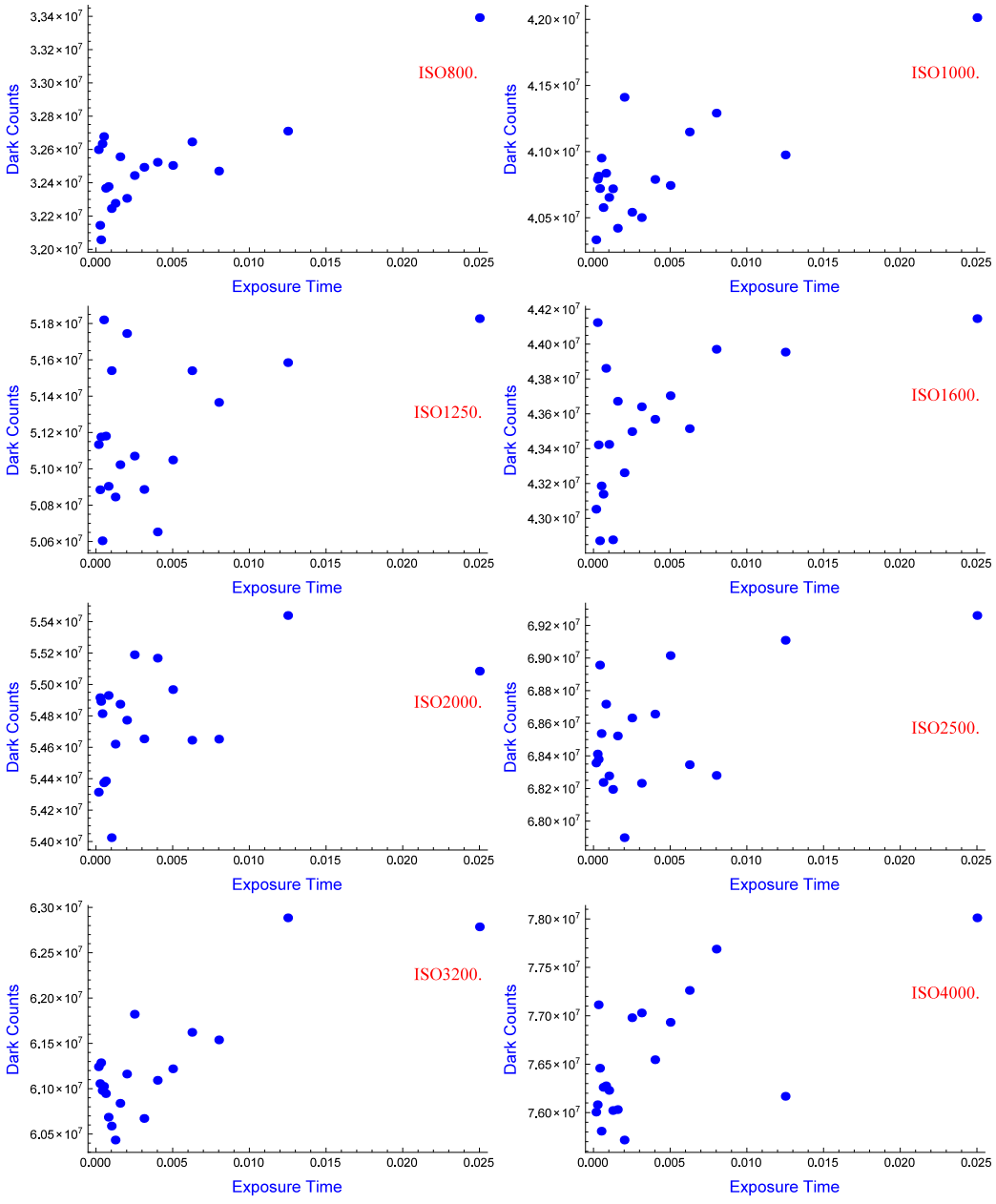

FIGURE A.1: Dark Counts vs Exp. T. (s) for different ISO:Part 1

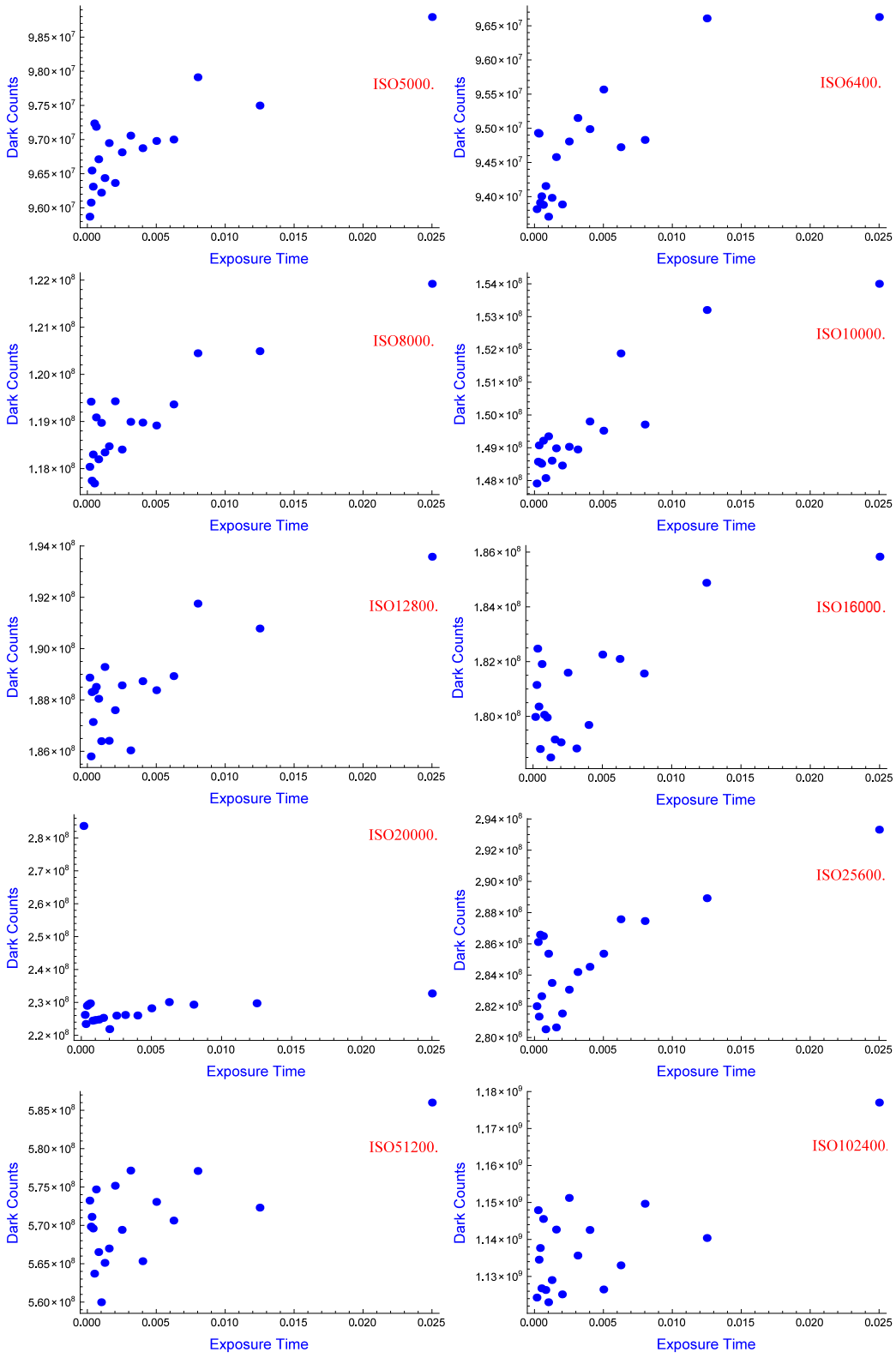

FIGURE A.2: Dark Counts vs Exposure Time (s) for different ISOs:Part 2

Here are the dark counts against different ISO settings depicted:

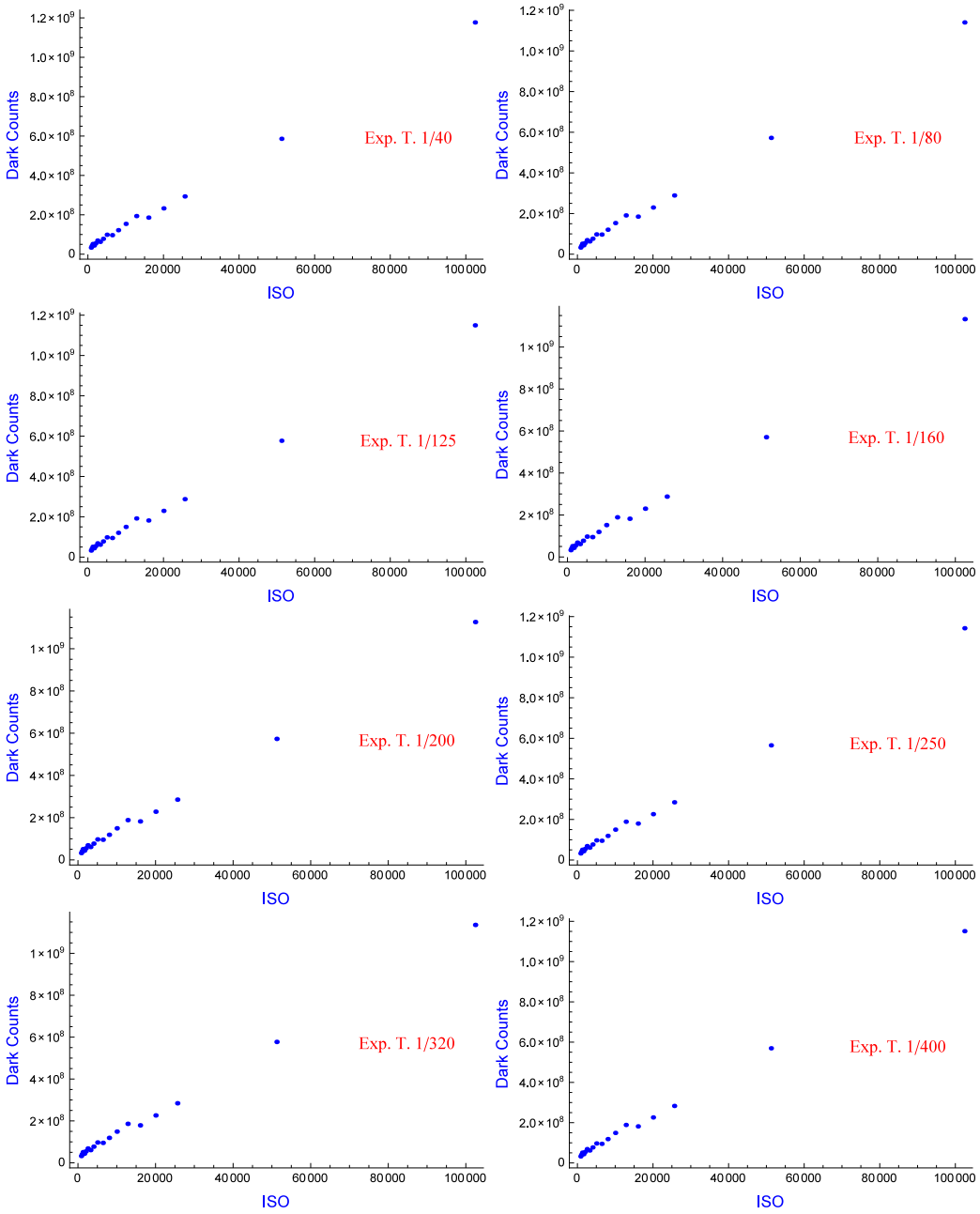

FIGURE A.3: Dark Counts vs ISO for different Exposure Times (s) :Part 1

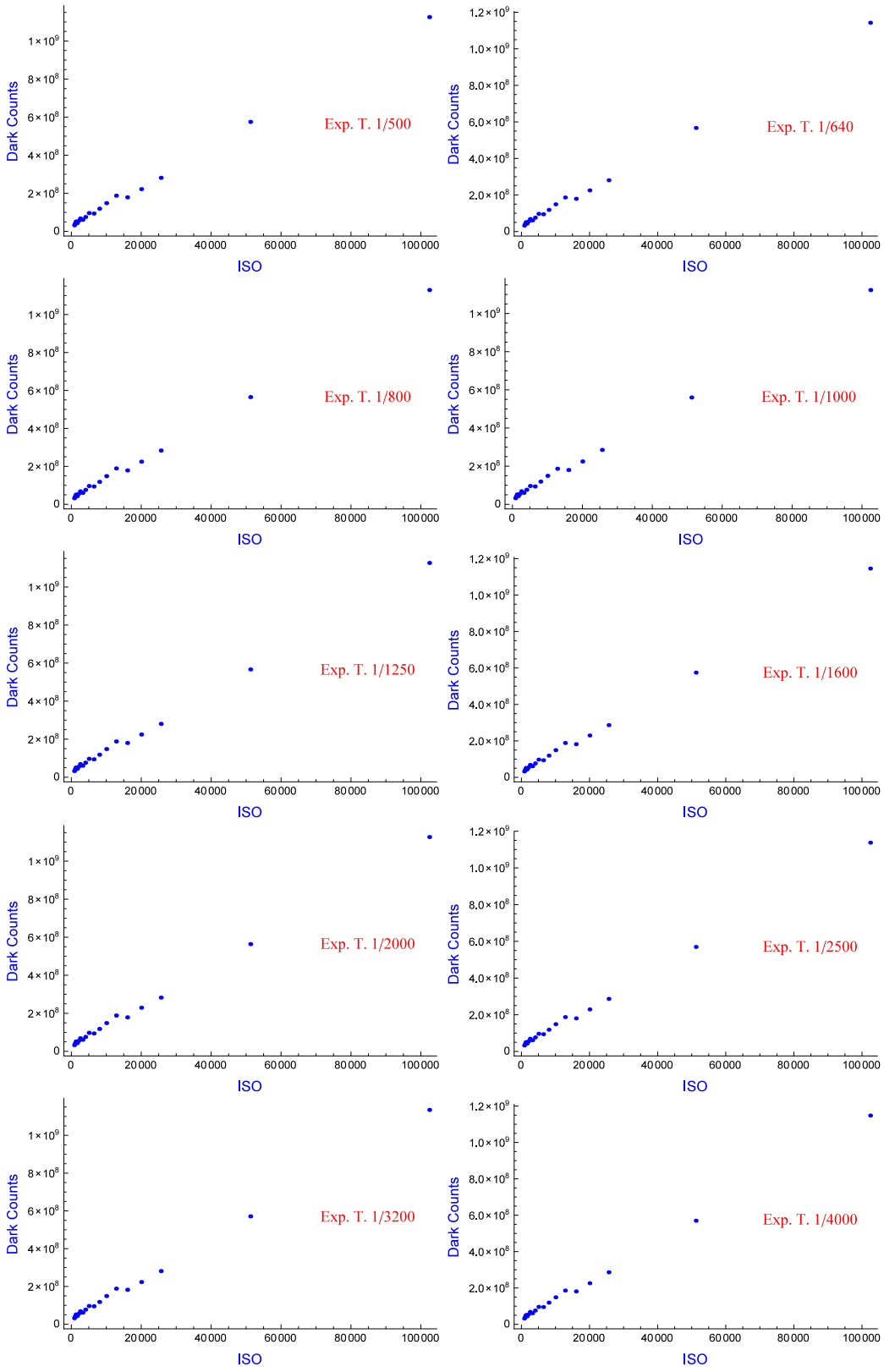

FIGURE A.4: Dark Counts vs ISO for different Exposure Times (s) :Part 2

A.2 Measurements with green laser and IR filter on

A.2.1 Green pixels

Here are the complete set of graphs corresponding to different ISO settings for green pixels:

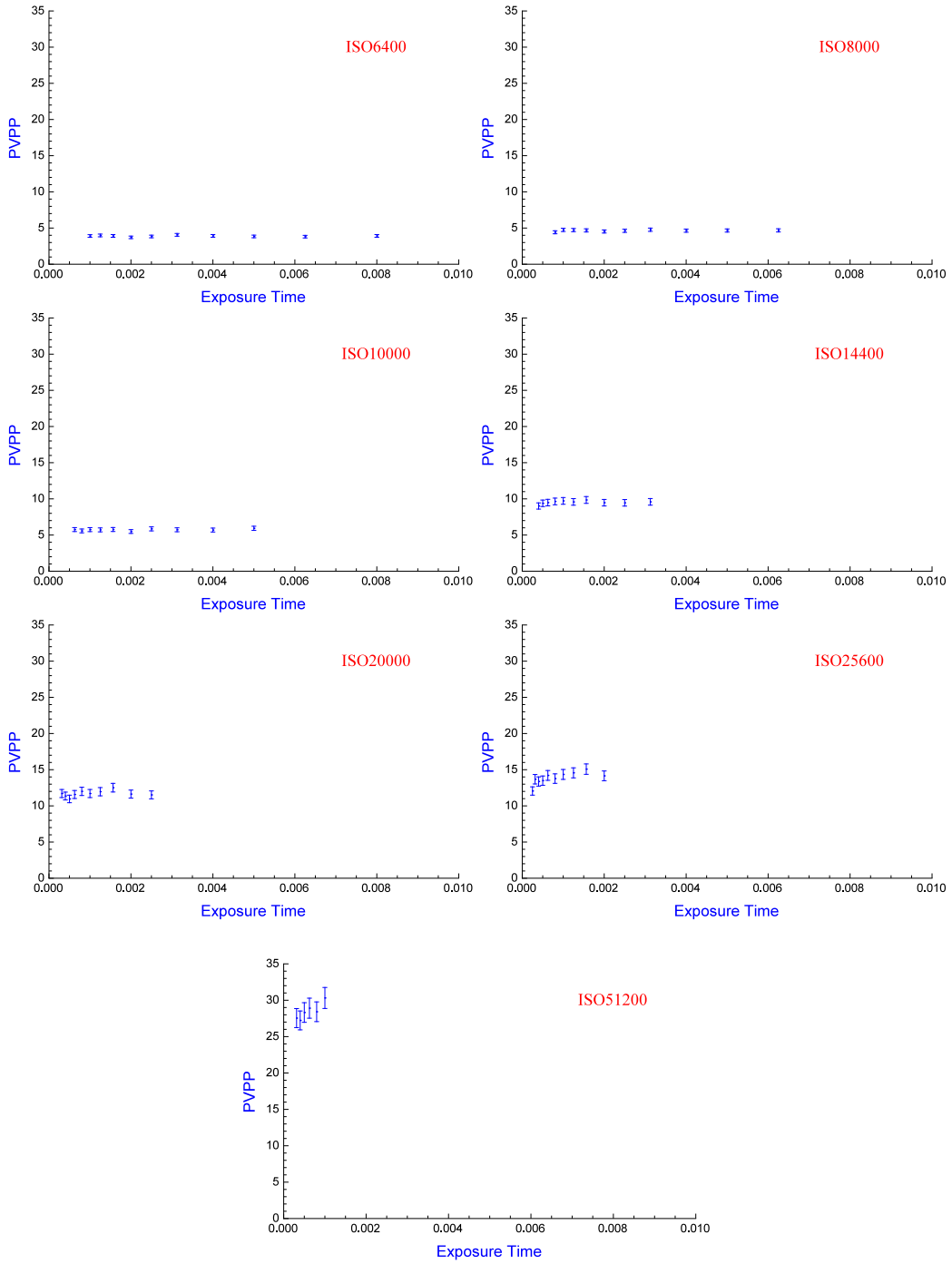

FIGURE A.5: Pixel value per photon for green pixels with laser beam power of 0.07 nW and wavelength of 532 nm.

A.2.2 Blue pixels

Here are the complete set of graphs corresponding to different ISO settings for blue pixels and green laser:

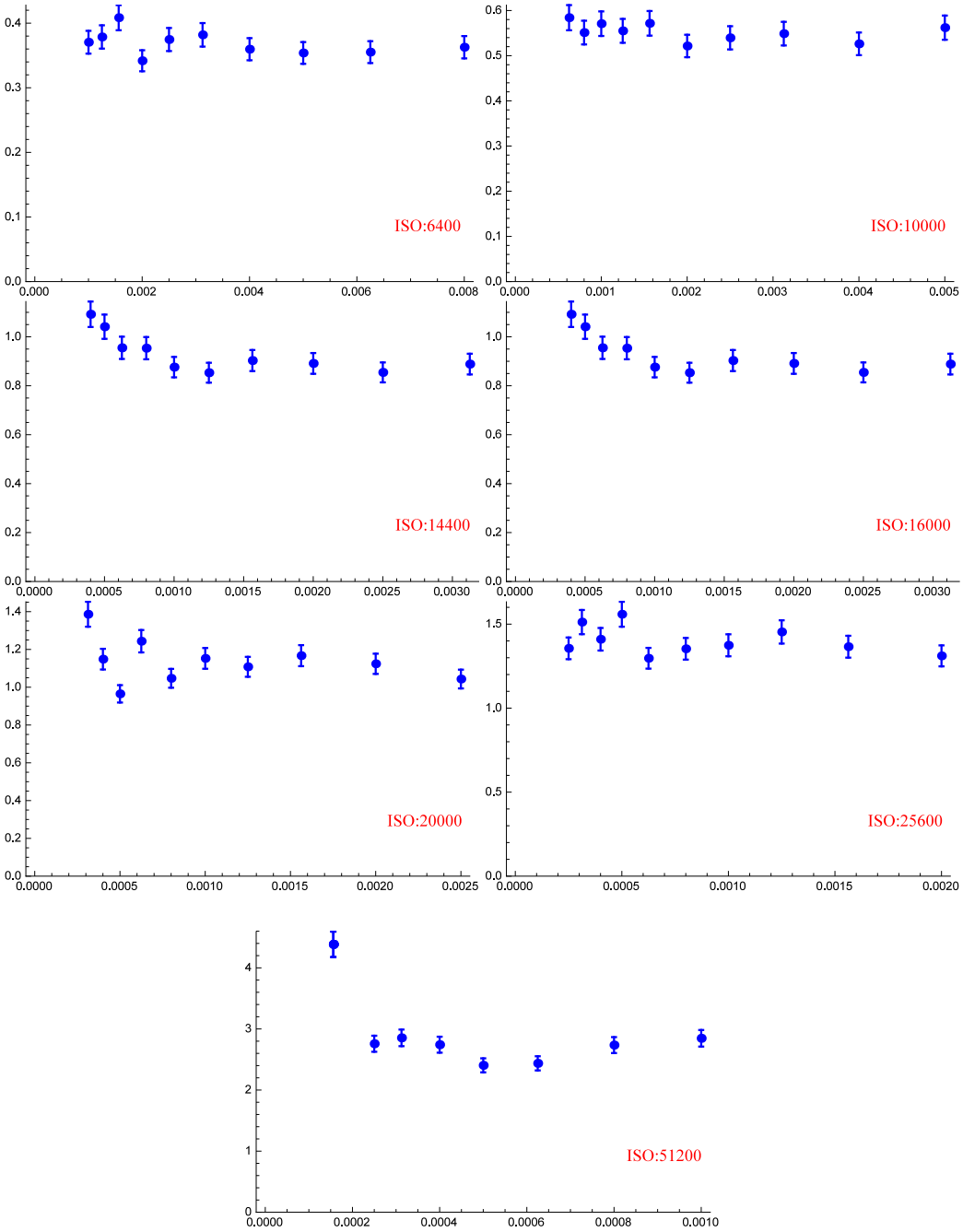

FIGURE A.6: Pixel value per photon versus Exposure time with different ISO settings for blue pixels with laser beam power of 0.07 nW and wavelength of 532 nm

A.2.3 Red pixels

Here are the complete set of graphs corresponding to different ISO settings for red pixels and green laser:

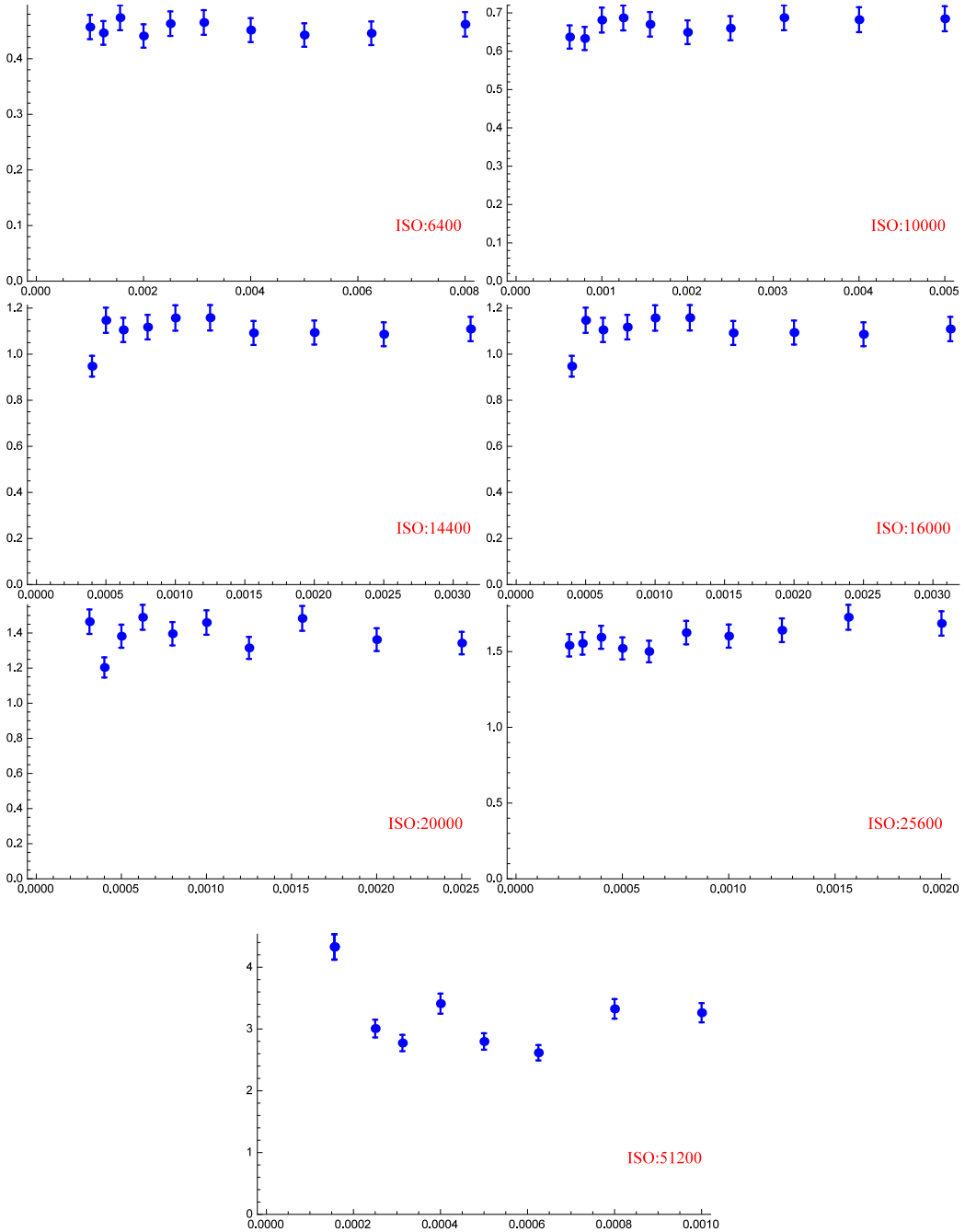

FIGURE A.7: Pixel value per photon versus Exposure time with different ISO settings for red pixels with laser beam power of 0.07 nW and wavelength of 532 nm

A.3 Measurements with IR laser after removing the IR filter

A.3.1 Red pixels

Here are the complete set of graphs corresponding to different ISO settings for red pixels with IR laser:

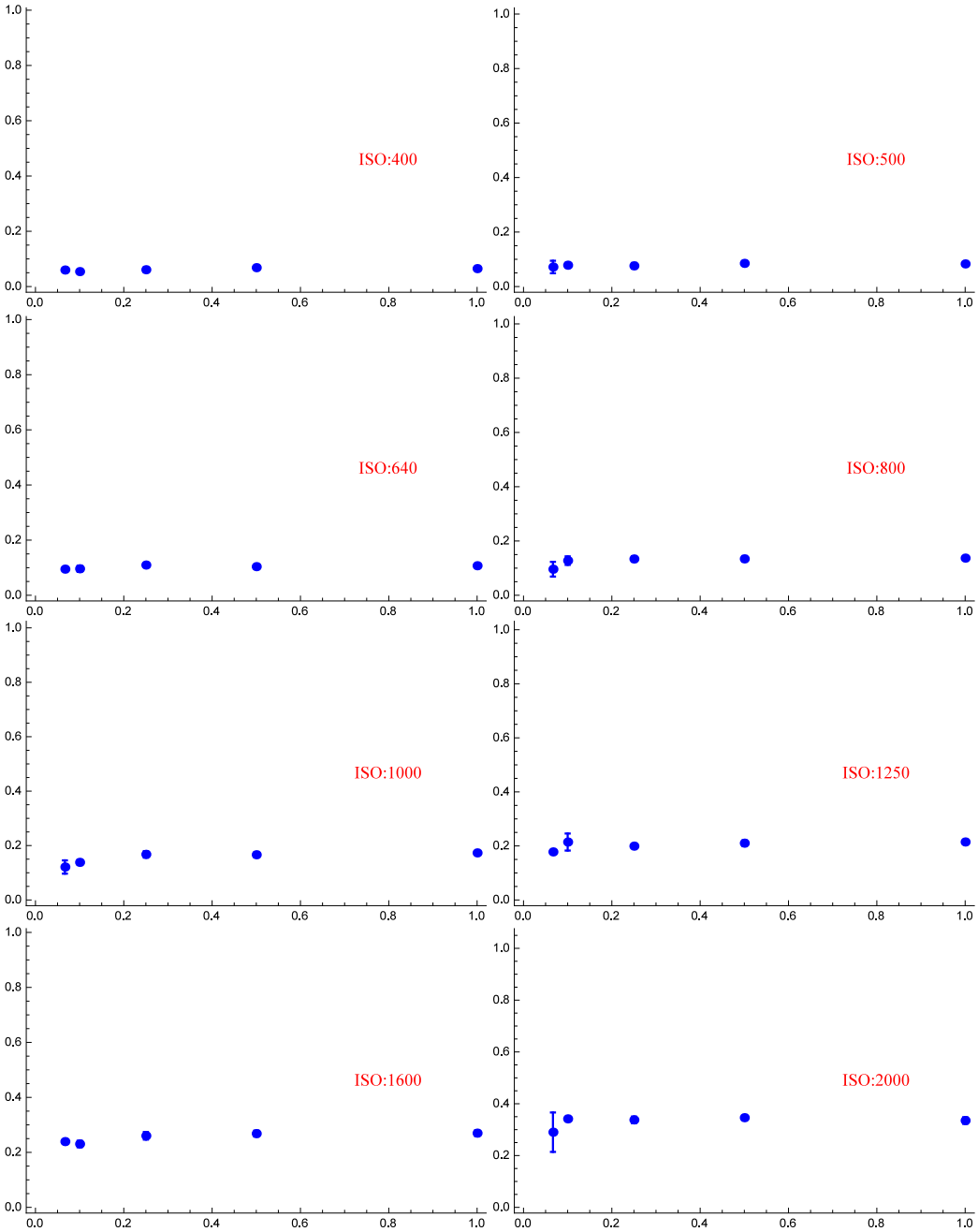

FIGURE A.8: Pixel value per photon vs exposure time (s) for red pixels exposed with IR laser: Part1

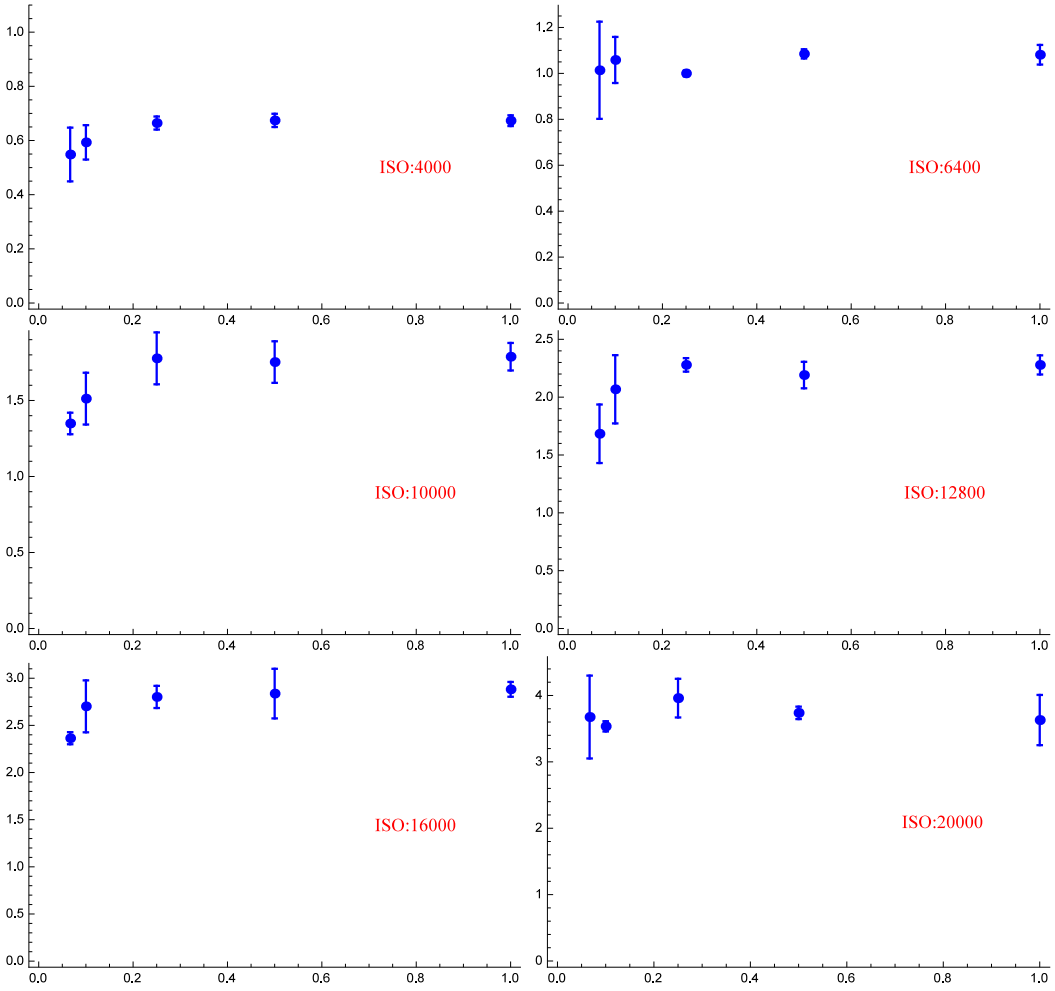

FIGURE A.9: Pixel value per photon vs exposure time (s) for red pixels exposed with IR laser : Part2

A.3.2 Blue Pixels

Here are the complete set of graphs corresponding to different ISO settings for blue pixels with IR laser:

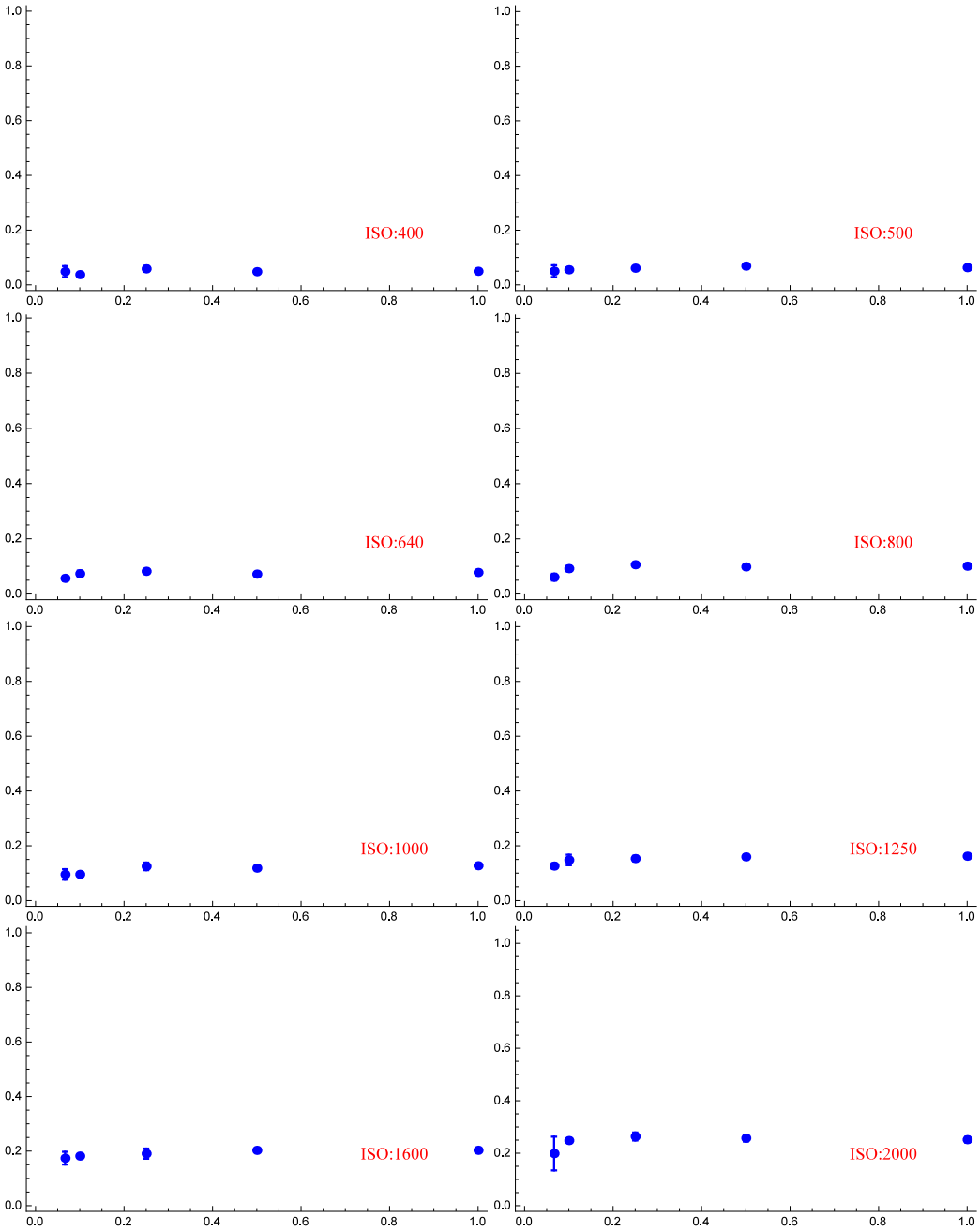

FIGURE A.10: Pixel value per photon vs exposure time (s) for blue pixels exposed with IR laser : Part1

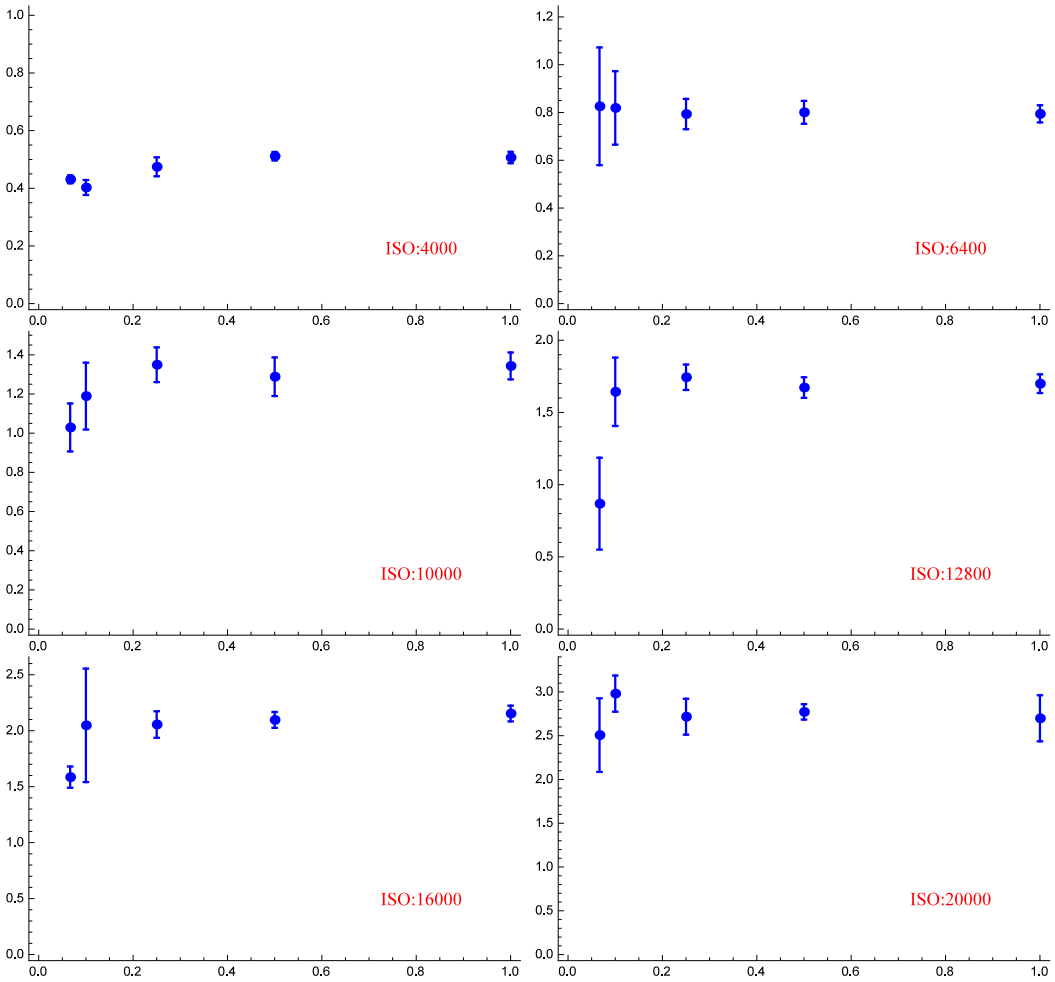

FIGURE A.11: Pixel value per photon vs exposure time (s) for blue pixels exposed with IR laser : Part2

A.3.3 Green pixels

Here are the complete set of graphs corresponding to different ISO settings for green pixels with IR laser:

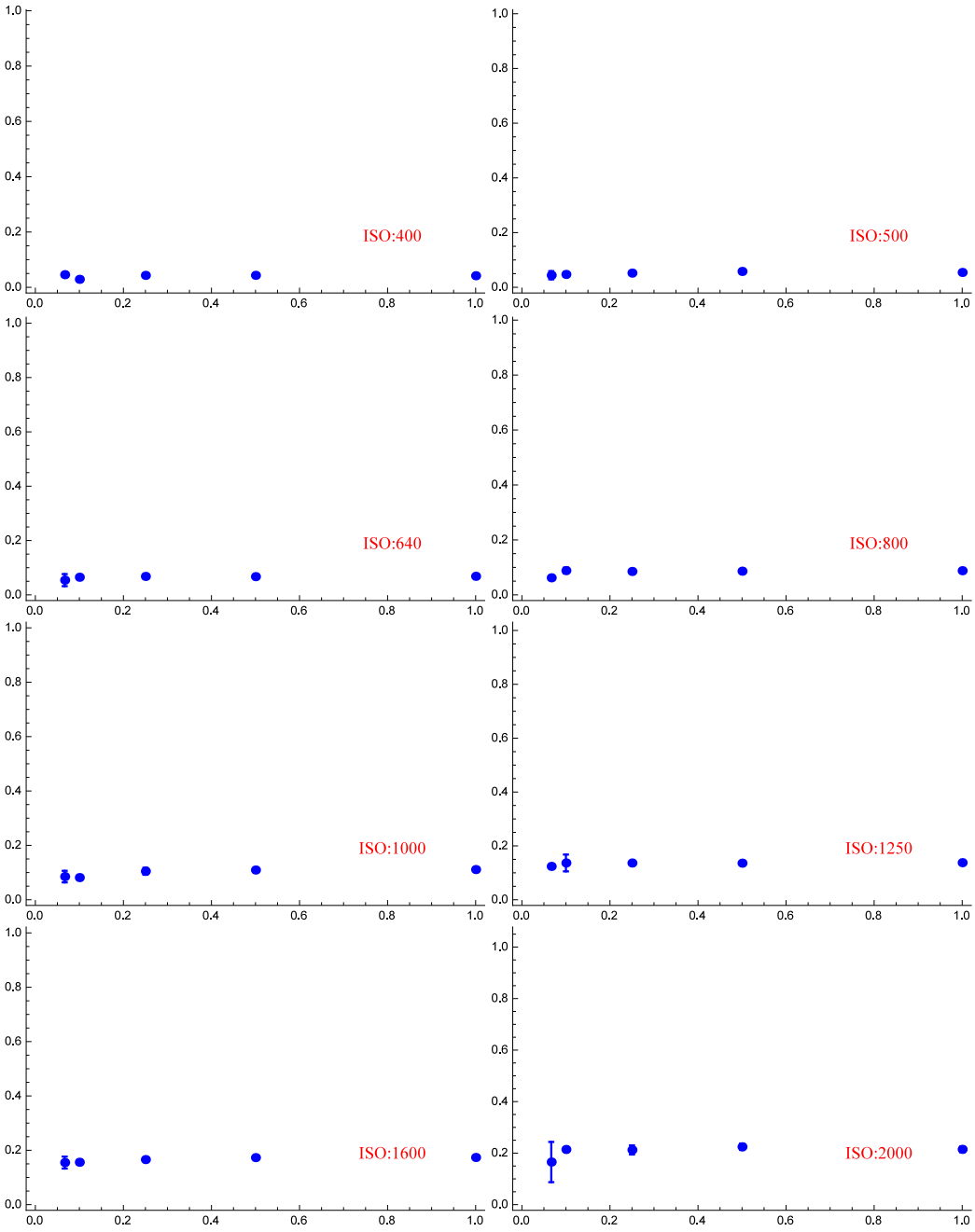

FIGURE A.12: Pixel value per photon vs exposure time (s) for green pixels exposed with IR laser : Part1

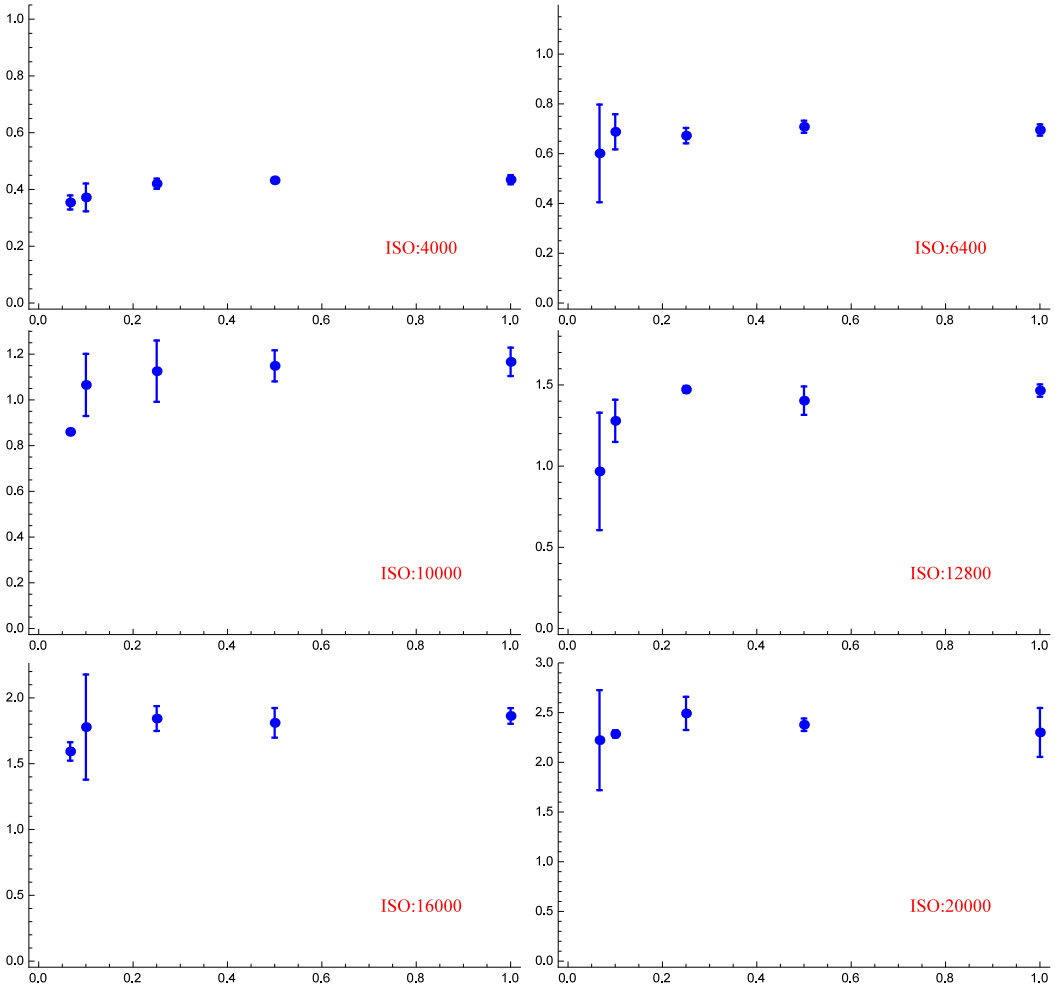

FIGURE A.13: Pixel value per photon vs exposure time (s) for green pixels exposed with IR laser : Part2

A.4 Comparing graph of the PVPP values for both wavelengths

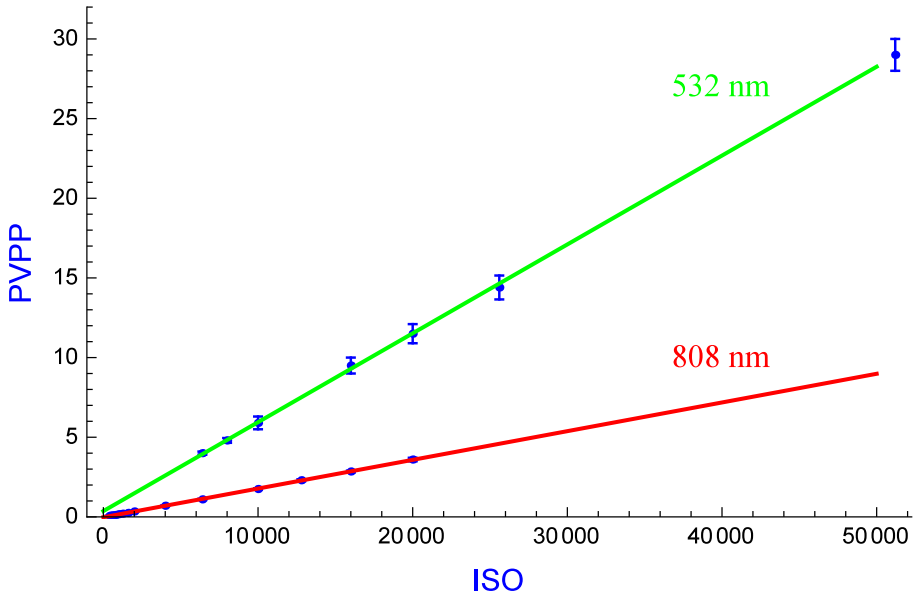

FIGURE A.14: Pixel value per photon vs ISO for red pixels exposed with 808 nm laser and green pixels exposed with 532 nm.

Appendix B

Orbits

B.1 Different geocentric satellite orbits

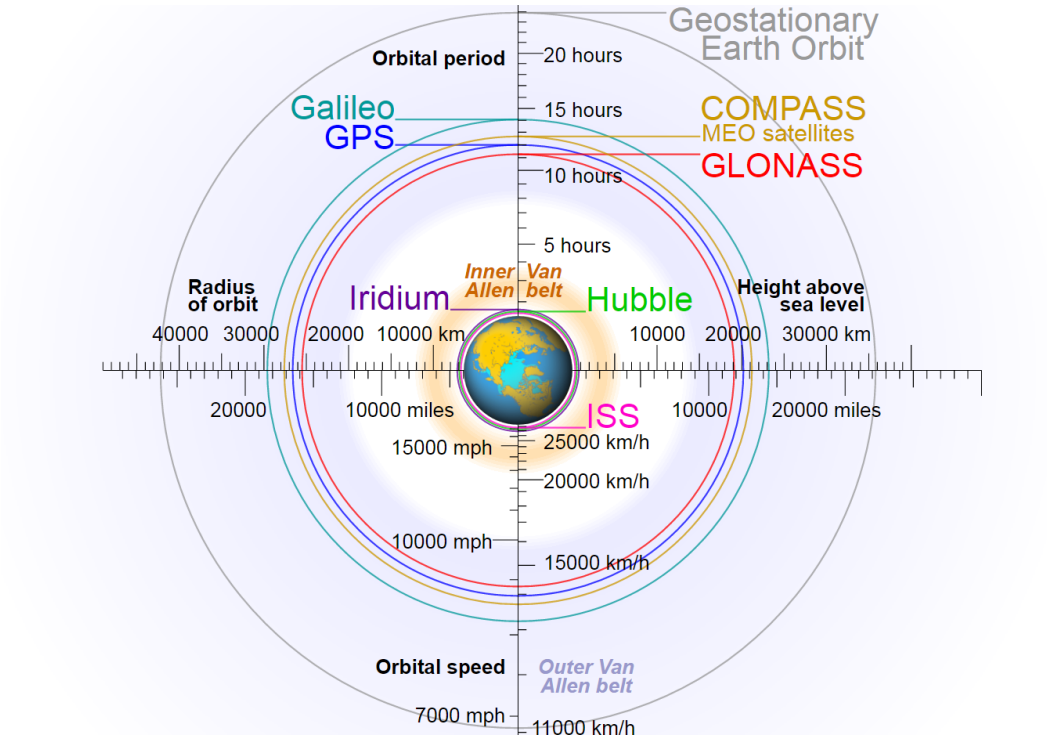

FIGURE B.1: Different orbits of the satellites including their orbital radius, velocity and period.

There are different orbits above the Earth that allow a great number of satellites orbit around the Earth. Figure B.1[1] shows a sketch of these orbits with the corresponding altitudes, velocities and orbital periods.

[1] https://upload.wikimedia.org/wikipedia/commons/b/b4/Comparison_satellite_navigation_orbits.svg

B.2 Low Earth Orbit

A low Earth orbit (LEO) is an orbit around the Earth with an altitude range of 160 to 2000 km and orbit period of respectively 88 minutes to 127 minutes. The velocity of the satellite in this orbit is ca. 7.8 km/s and decreases if the altitude increases. This range of orbit is located in two atmospheric layers. From 160 to 500 km is inside thermosphere and from 500 to 2000 in exosphere. This orbit is simplest and cheapest for satellite placement. Beside the International Space Station, many other satellites have LEO orbit such as spy satellites, Earth observation satellites, many communication satellites, etc.

B.3 Medium Earth Orbit

Medium Earth orbit (MEO) also known as intermediate circular orbit (ICO), is an orbit around the Earth with a range of altitude from 2000 km to 35000 km with orbital periods from 2 to approximately 24 hours. The most common use of this orbit is for navigation, communication, and geodetic or space environment science. The most common altitude of MEO orbital region is in altitude of 20000 km (with 12 hrs period) which is used for instance by the satellites of Global Positioning System (GPS).

B.4 Geostationary orbit

A geostationary orbit, geostationary Earth orbit or geosynchronous equatorial orbit (GEO) is a circular orbit at the altitude of 35,786 km. It's called stationary as the objects in this orbit have an orbital period equal to the Earth's rotational period (23:56':4"), therefore seem motionless to ground observers. The satellites have a velocity of 3.07 km/s in this orbit. Most of commercial communication satellites, broadcast satellites, and satellites of satellite-based augmentation system operate in this orbit.
Any orbit with altitude greater than geosynchronous orbit (35,786 km) is considered High Earth orbit.

Bibliography

[1] *Annex 1 : Additional technical Information on ISS capabilities and background information*. Tech. rep. European Space Staion, pp. 1–71. URL: http://wsn.spaceflight.esa.int/docs/201107/Annex1-ESA-ISS-CC-AO-Climate-Change.pdf.

[2] Markus Aspelmeyer et al. "(" QSpace ") Final Report". In: (2003).

[3] John S. Bell. "On the problem of hidden variables in quantum mechanics". In: *Reviews of Modern Physics* 38.3 (1966), pp. 447–452. ISSN: 00346861. DOI: 10.1103/RevModPhys.38.447. URL: http://journals.aps.org/rmp/abstract/10.1103/RevModPhys.38.447.

[4] Cristian Bonato et al. "Influence of satellite motion on polarization qubits in a Space-Earth quantum communication link." In: *Optics express* 14.21 (2006), pp. 10050–10059. ISSN: 1094-4087. DOI: 10.1364/OE.14.010050. URL: https://www.osapublishing.org/oe/abstract.cfm?URI=oe-14-21-10050.

[5] David Deutsch. "Quantum mechanics near closed timelike lines". In: *Physical Review D* 44.10 (Nov. 1991), pp. 3197–3217. ISSN: 0556-2821. DOI: 10.1103/PhysRevD.44.3197. URL: http://link.aps.org/doi/10.1103/PhysRevD.44.3197.

[6] T O T H E Editor et al. *8 Appendix*. Tech. rep. 1.0 d.d. 14 Apr 15. Cosine Research B.V., pp. 30–36.

[7] A Einstein, B Podolsky, and N Rosen. "Phys. Rev. 47, 777 (1935): Can Quantum-Mechanical Description of Physical Reality Be Considered Complete?" In: *Phys. Rev.* 47 (1935), pp. 777–780. ISSN: 0031-899X. DOI: 10.1103/PhysRev.47.777. URL: http://prola.aps.org/abstract/PR/v47/i10/p777{_}1{\textbackslash}npapers2://publication/doi/10.1103/PhysRev.47.777.

[8] Artur K. Ekert. "Quantum cryptography based on Bell's theorem". In: *Physical Review Letters* 67.6 (1991), pp. 661–663. ISSN: 00319007. DOI: 10.1103/PhysRevLett.67.661. URL: http://journals.aps.org/prl/abstract/10.1103/PhysRevLett.67.661.

[9] M Esposito and S Conticello. *QPOD project Trade-off between ISS and Cubesats platforms*. Tech. rep. 1.0 d.d. 14 Apr 15. 2015, pp. 1–36.

[10] A. Fedrizzi et al. "Practical quantum key distribution with polarization entangled photons". In: *2005 European Quantum Electronics Conference, EQEC '05* 2005 (2005), p. 303. ISSN: 1094-4087. DOI: 10.1109/EQEC.2005.1567469. URL: https://www.osapublishing.org/oe/abstract.cfm?uri=oe-12-16-3865.

[11] Nicolas Gisin et al. "Quantum cryptography". In: *Reviews of Modern Physics* 74.1 (2002), pp. 145–195. ISSN: 00346861. DOI: 10.1103/RevModPhys.74.145. URL: http://journals.aps.org/rmp/abstract/10.1103/RevModPhys.74.145.

[12] Daniel Gottesman et al. “Security of quantum key distribution with imperfect devices”. In: *Quantum Information and Computation* 4.5 (2004), pp. 325–360. ISSN: 1533-7146. DOI: 10.1109/ISIT.2004.1365172. URL: http://arxiv.org/abs/quant-ph/0212066.

[13] Breck Hitz, J.J. Ewing, and Jeff Hecht. *Introduction to Laser Technology*. 1. 2014, pp. 1–5. ISBN: 9780874216561. DOI: 10.1007/s13398-014-0173-7.2. URL: http://eu.wiley.com/WileyCDA/WileyTitle/productCd-0470916206.html.

[14] Paul G. Kwiat et al. “New high-intensity source of polarization-entangled photon pairs”. In: *Physical Review Letters* 75.24 (1995), pp. 4337–4341. ISSN: 00319007. DOI: 10.1103/PhysRevLett.75.4337. URL: https://journals.aps.org/prl/pdf/10.1103/PhysRevLett.75.4337.

[15] Xiao-Song Ma et al. “Quantum teleportation over 143 kilometres using active feed-forward.” In: *Nature* 489.7415 (2012), pp. 269–73. ISSN: 1476-4687. DOI: 10.1038/nature11472. URL: http://www.ncbi.nlm.nih.gov/pubmed/22951967.

[16] Michael a. Nielsen and Isaac L. Chuang. *Quantum Computation and Quantum Information: 10th Anniversary Edition*. 2011, p. 702. ISBN: 1107002176. DOI: 10.1017/CBO9780511976667. URL: http://www.cambridge.org/at/academic/subjects/physics/quantum-physics-quantum-information-and-quantum-computation/quantum-computation-and-quantum-information-10th-anniversary-edition.

[17] *QUANTUM INFORMATION AND QUANTUM PHYSICS IN SPACE: EXPERIMENTAL EVALUATION (“QIPS”)*. Tech. rep. 2007. arXiv: 9604166 [astro-ph].

[18] T. C. Ralph and J. Pienaar. “Entanglement decoherence in a gravitational well according to the event formalism”. In: *New Journal of Physics* 16 (2014). ISSN: 13672630. DOI: 10.1088/1367-2630/16/8/085008.

[19] T. Scheidl, E. Wille, and R. Ursin. “Quantum optics experiments using the International Space Station: A proposal”. In: *New Journal of Physics* 15 (2013). ISSN: 13672630. DOI: 10.1088/1367-2630/15/4/043008. URL: http://iopscience.iop.org/article/10.1088/1367-2630/15/4/043008/meta.

[20] Tobias Schmitt-Manderbach et al. “Experimental demonstration of free-space decoy-state quantum key distribution over 144 km”. In: *Physical Review Letters* 98.1 (2007), pp. 1–4. ISSN: 00319007. DOI: 10.1103/PhysRevLett.98.010504.

[21] D. Stucki et al. “High rate, long-distance quantum key distribution over 250 km of ultra low loss fibres”. In: *New Journal of Physics* 11 (2009). ISSN: 13672630. DOI: 10.1088/1367-2630/11/7/075003. URL: http://iopscience.iop.org/article/10.1088/1367-2630/11/7/075003/meta.

[22] Wolfgang Tittel, Nicolas Gisin, and Hugo Zbinden. *Die eigentümliche Natur der Quantenmechanik läßt sich für die Übertragung geheimer Nachrichten ausnutzen Wolfgang Tittel, Jürgen Brendel, Nicolas Gisin, Grégoire Ribordy, Hugo Zbinden*. 1999, pp. 25–30. URL: http://onlinelibrary.wiley.com/doi/10.1002/phbl.19990550608/abstract.

[23] R. Ursin et al. “Entanglement-based quantum communication over 144 km”. In: *Nature Physics* 3.7 (2007), pp. 481–486. ISSN: 1745-2473. DOI: 10.1038/nphys629. URL: http://www.nature.com/doifinder/10.1038/nphys629.

[24] Edo Waks, Assaf Zeevi, and Yoshihisa Yamamoto. “Security of quantum key distribution with entangled photons against individual attacks”. In: *Physical Review A* 65.5 (2002), pp. 1–16. ISSN: 1050-2947. DOI: 10.1103/PhysRevA.65.052310. URL: http://link.aps.org/doi/10.1103/PhysRevA.65.052310.

[25] Xiang Bin Wang. “Decoy-state protocol for quantum cryptography with four different intensities of coherent light”. In: *Physical Review A - Atomic, Molecular, and Optical Physics* 72.1 (2005), pp. 1–6. ISSN: 10502947. DOI: 10.1103/PhysRevA.72.012322. URL: http://journals.aps.org/pra/abstract/10.1103/PhysRevA.72.012322.